Computational Study of Liquid Film Flows along Flat and Undulated Substrates

by

Phuc-Khanh Nguyen

A dissertation submitted in partial fulfillment
of the requirements for the degree of
Doctor of Philosophy
(Mechanical Engineering)
in The University of Thessaly
September 2012

Doctoral Committee:

Professor Vasilis Bontozoglou, Chairman
Professor Dimitris Valourgeorgis
Professor Nikos Pelekasis
Associate Professor Nikos Andritsos
Professor John Tsamopoulos, University of Patras
Professor Stergios G. Yiantsios, Aristotle University of Thessaloniki
Professor Demetrios T. Papageorgiou, Imperial College in London

Institutional Repository - Library & Information Centre - University of Thessaly
09/06/2024 06:51:43 EEST - 18.219.33.223

© Phuc-Khanh Nguyen 2012

All Rights Reserved

Institutional Repository - Library & Information Centre - University of Thessaly
09/06/2024 06:51:43 EEST - 18.219.33.223

To Hanh and Phi

Institutional Repository - Library & Information Centre - University of Thessaly
09/06/2024 06:51:43 EEST - 18.219.33.223

ACKNOWLEDGEMENTS

Having a good working experience in the University of Thessaly, I am deeply indebted to my advisor, Professor Vasilis Bontozolgou for his encouragement and enthusiasm. I feel very lucky to have such an important and beautiful time of fruitful collaboration with him, making this three year period in Volos an unforgettably good memory in my life. My research progress is constantly paved with his guidance, and inspired by his simplicity and understanding. I really feel good thank to his refined treatment toward his students, that helps nurturing a free mind for new thought and illuminating my research work.

Essentially, I would like to acknowledge the research funding from the EU-FP7-Marie-Curie Initial Training Network "MULTIFLOW" via a grant number PITN-GA-214919-2. It facilitated me to make several participations to different scientific conferences, workshops and collaboration in several places, along with broader views of this world. In regard of some scientific interactions between nodes, I would like to thank to Prof. Kalliadasis, and his co-worker, Dr. Pradas for discussion during my work visit in the Imperial College London, that leads to a joint paper on *Bound-State Formation on Falling Liquid Films*. My thankful expressions also go to Prof. Ruyer-Quil for his initiative, and his PhD candidate Symphony from the FAST laboratory in Orsay-Paris for good collaboration in the study of *Extreme Solitary Wave* with quality outcomes. Special thanks go to Prof. Papageorgiou for embracing several discussions about linearisation. Eventually I would kindly like to express my deep gratitude to the doctoral committee for their helpful suggestions and for serving on my dissertation committee.

In a long course of my research work in the University of Thessaly, it is not enough to thank to graceful secretaries Nicoletta and Joe for their abundant help. Especially, my great thanks go to Nicoletta for her company in dealing with all kinds of public offices in Volos. I sincerely thank Prof. Andritsos for his kind concern to my living in Volos and his active help at the Department. Never enough, I would kindly like to say thanks to several other personnels in the department for providing me technical assistance and help, and to my several friends for a lot of wonderful moment with

Institutional Repository - Library & Information Centre - University of Thessaly
09/06/2024 06:51:43 EEST - 18.219.33.223

them in the seafront of Volos or around the mount Pelion.

Last but not least, my deep gratitude goes to my big brother, Alain, for showing me a good living example and for his invaluable encouragements along my graduate course. Finally, a lot of cherished thank goes to my little family, Hanh and Phi, who truly rewards me with so much lively and joyful moments together in the beautiful city Volos.

Institutional Repository - Library & Information Centre - University of Thessaly
09/06/2024 06:51:43 EEST - 18.219.33.223

TABLE OF CONTENTS

Institutional Repository - Library & Information Centre - University of Thessaly
09/06/2024 06:51:43 EEST - 18.219.33.223

Institutional Repository - Library & Information Centre - University of Thessaly
09/06/2024 06:51:43 EEST - 18.219.33.223

Institutional Repository - Library & Information Centre - University of Thessaly
09/06/2024 06:51:43 EEST - 18.219.33.223

LIST OF FIGURES

Figure

Institutional Repository - Library & Information Centre - University of Thessaly
09/06/2024 06:51:43 EEST - 18.219.33.223

Institutional Repository - Library & Information Centre - University of Thessaly
09/06/2024 06:51:43 EEST - 18.219.33.223

Institutional Repository - Library & Information Centre - University of Thessaly
09/06/2024 06:51:43 EEST - 18.219.33.223

Institutional Repository - Library & Information Centre - University of Thessaly
09/06/2024 06:51:43 EEST - 18.219.33.223

Institutional Repository - Library & Information Centre - University of Thessaly
09/06/2024 06:51:43 EEST - 18.219.33.223

Institutional Repository - Library & Information Centre - University of Thessaly
09/06/2024 06:51:43 EEST - 18.219.33.223

LIST OF TABLES

Table

Institutional Repository - Library & Information Centre - University of Thessaly
09/06/2024 06:51:43 EEST - 18.219.33.223

ABSTRACT

Computational Study of Liquid Film Flows
along Flat and Undulated Substrates
by
Phuc-Khanh Nguyen

Chairman: Prof. Vasilis Bontozoglou

This work presents a computational study of the gravity-driven liquid film flowing along either a flat wall, or a wall with periodic corrugations. The Galerkin Finite Element Method (FEM) briefly described in Chapter 2 is used to solve the two dimensional Navier-Stokes equations with appropriate boundary conditions. For the film flow on a flat wall, the properties of the extreme solitary wave, fully developed and stationary in the co-moving frame, are derived in terms of the flow rate and liquid properties in Chapter 3. Emphasis is placed on high Reynolds numbers, where inertia has a strong influence (drag-inertia regime), and where the predictions of simplified model diverge impressively. Moreover, these solitary waves are found to interact with each other and to form bound-states separated by intrinsically defined separation distances, documented in Chapter 4. Time-dependent computations show that, at short intrinsic separations, a continuous oscillation around the mean separation takes place.

Next, the steady solutions of inertial film flows along strongly corrugated substrates are systematically computed to describe the coupling of free surface deformation and recirculation eddy around the bottom trough, in three regimes of subcritical, resonance, and supercritical flow. Finally the numerical methodology for a time-dependent computation and its linearised version are developed in Chapter 6. Time-dependent direct numerical simulation (DNS) results predict a stabilising effect of corrugations on the liquid film flow. They further demonstrate that, above the critical threshold, energy-transfer takes place from long-wave to short-wave modes, and thus the classical long-wave instability is delayed and a short-wave appears first.

Institutional Repository - Library & Information Centre - University of Thessaly
09/06/2024 06:51:43 EEST - 18.219.33.223

ΠΕΡΙΛΗΨΗ

Υπολογιστική Μελέτη της Ροής Υγρού Υμένα
σε Επίπεδα ή Διαμορφωμένα Υποστρώματα

του

Phuc-Khanh Nguyen

Επιβλέπων: Καθηγητής Βασίλης Μποντόζογλου

Στην παρούσα εργασία, εξετάζεται υπολογιστικά η βαρυτική ροή υγρού υμένα πάνω σε επίπεδο ή σε περιοδικά διαμορφωμένο υπόστρωμα. Στο κεφάλαιο 2 παρουσιάζεται συνοπτικά η μέθοδος Galerkin πεπερασμένων στοιχείων, η οποία χρησιμοποιείται για την επίλυση των διδιάστατων εξισώσεων Navier-Stokes με τις κατάλληλες συνοριακές συνθήκες. Στο κεφάλαιο 3 μελετάται η ροή σε επίπεδο υπόστρωμα, και ειδικότερα υπολογίζονται οι ιδιότητες των πλήρως ανεπτυγμένων μοναχικών κυμάτων. Έμφαση δίνεται σε υψηλούς αριθμούς Reynolds, όπου η αδράνεια έχει ισχυρή επίδραση (drag-inertia regime), και όπου οι προβλέψεις των απλοποιημένων μοντέλων αποκλίνουν μεταξύ τους εντυπωσιακά. Στη συνέχεια, εξετάζεται στο κεφάλαιο 4 η αλληλεπίδραση των μοναχικών κυμάτων, και αποδεικνύεται ότι διαδοχικά κύματα σχηματίζουν συζευγμένες δυάδες και τριάδες (bound states), όπου οι κορυφές απέχουν μεταξύ τους καθορισμένες αποστάσεις. Χρονο-εξαρτώμενοι υπολογισμοί αποδεικνύουν ότι, για κοντινές αποστάσεις των κορυφών, λαμβάνει χώρα συνεχής ταλάντωση γύρω από τη μέση τιμή.

Στο κεφάλαιο 5 εξετάζεται συστηματικά η μόνιμη ροή υγρού υμένα πάνω σε περιοδικό υπόστρωμα με έντονη διαμόρφωση, και περιγράφεται η σύζευξη της ελεύθερης επιφάνειας και της δίνης ανακυκλοφορίας στον πυθμένα της διαμόρφωσης στην υποκρίσιμη περιοχή, την περιοχή συντονισμού και την υπερκρίσιμη. Τέλος, στο κεφάλαιο 6 αναπτύσσεται η υπολογιστική μέθοδος υπολογισμού χρονο-μεταβαλλόμενων ροών, καθώς και η ειδική εκδοχή της που αφορά γραμμική ροή (μικρές αποκλίσεις από την μόνιμη κατάσταση). Οι ακριβείς υπολογισμοί (DNS) προβλέπουν τη σταθεροποίηση της ροής υγρού υμένα λόγω των περιοδικών διαμορφώσεων. Επιπλέον, αποδεικνύουν ότι, πέρα από τις κρίσιμες συνθήκες, γίνεται μεταφορά ενέργειας από τα μεγάλα μήκη κύματος προς μήκη στην περιοχή της διαμόρφωσης. Με τον τρόπο αυτό, αναβάλλεται η εμφάνιση της κλασσικής αστάθειας μεγάλου μήκους, και οι πρώτες ασταθείς διαταραχές είναι πεπερασμένου μήκους κύματος.

Institutional Repository - Library & Information Centre - University of Thessaly
09/06/2024 06:51:43 EEST - 18.219.33.223

NOMENCLATURE

Roman Letters

$\mathbb{C}$	Continuity equation, page 17
$\mathbb{K}$	Kinematic equation, page 17
$\mathbb{M}$	Momentum conservation equation, page 17
$\underline{\underline{J}}$	Jacobian, page 107
$\underline{\underline{T}}$	Stress tensor of liquid, non-dimensionlised, page 17
$\underline{g}$	Unit vector in the direction of the gravity, non-dimensionlised, page 17
$\underline{n}$	Normal unit vector on the free surface, pointing outward from the fluid, page 19
$\underline{Q}$	Unknown variable vector, page 106
$\underline{U}$	Velocity vector, non-dimensionlised, page 17
$\underline{U}_i$	Velocity vector of liquid at node i, page 20
$\underline{X}_i$	Cartesian coordinate vector of node i in physical domain, page 20
A	Corrugation steepness, page 101
a	Dimensional wall amplitude, page 69
C	Phase speed, nondimensionalised, page 32
c	Phase speed, in dimensional value, page 7
D	Position of mesh refinement, page 35
E_I	Eddy intensity, page 71
E_S	Eddy size, page 71
g	Gravitational acceleration, page 5
g_x	Component of the gravitational acceleration projected in the x direction, page 5
g_y	Component of the gravitational acceleration projected in the y direction, page 5
H	Height of the free surface, non-dimensionlised, page 17
h	Height of the free surface, in dimensional value, page 5
H_i	Height of free surface at node i, page 20

Institutional Repository - Library & Information Centre - University of Thessaly
09/06/2024 06:51:43 EEST - 18.219.33.223

h_N Mean film thickness based on the steady flow Nusselt solution, in dimensional value, page 7

h_S Film thickness at the flat substrate far from the main hump, page 32

K Curvature of free surface, page 19

L Length of physical domain, page 35

l_c Capillary length of liquid, page 19

L_{12} Separation distance between the first and the second solitary pulse, page 61

L_{23} Separation distance between the second and the third solitary pulse, page 61

l_ν Viscous length of liquid, page 19

P Hydrostatic pressure of liquid, non-dimensionlised, page 17

p Hydrostatic pressure of liquid, in dimensional value, page 5

P_i Hydrostatic pressure of liquid at node i, page 20

P_{am} Ambient pressure of the supposedly uniform gas phase above the film flow, non-dimensionalised, page 19

q Flow rate per spanwise unit, page 32

r Ratio of flow rate along the actual corrugated wall to the hypothetical flat wall, page 82

R_C Residual by the Galerkin FEM of the continuity equation, page 22

R_K Residual by the Galerkin FEM of the kinematic equation, page 22

R_M Residual by the Galerkin FEM of the momentum equation, page 22

S Surface of liquid domain, page 22

T Time, non-dimensionlised, page 17

t_S Characteristic time scale, page 52

U Liquid velocity in X direction, non-dimensionlised, page 17

u Liquid velocity in the x direction, in dimensional value, page 5

u_N Mean film velocity based on the steady flow Nusselt solution, in dimensional value, page 7

u_S Mean film velocity at the flat substrate far from the main hump, page 32

V Liquid velocity in Y direction, non-dimensionlised, page 17

V Volume of liquid domain, page 22

v Liquid velocity in the y direction, in dimensional value, page 5

Greek Letters

α Inclination angle of the wall, page 5

β Clustering parameter, page 35

Institutional Repository - Library & Information Centre - University of Thessaly
09/06/2024 06:51:43 EEST - 18.219.33.223

β	Relative amplitude of the free surface deformation, page 71
$\boldsymbol{\eta}$	Global coordinate in the crosswise direction of computational domain, page 20
$\boldsymbol{\xi}$	Global coordinate in the streamwise direction of computational domain, page 20
δ	Dimensionless film thickness, page 70
η	Elementwise coordinate in crosswise direction of the computational domain, page 20
λ	Dimensional wavelength of the corrugated wall, page 69
λ_c	Ratio of the corrugation wavelength with respect to the capillary length, page 102
μ	Dynamic viscosity of liquid, page 5
ν	Kinematic viscosity of liquid, in dimensional value, page 7
Φ	Superficial phase shift, page 71
ϕ^i	Biquadratic basis function at node i, page 20
ψ^i	Bilinear basis function at node i, page 20
ρ	Density of liquid, page 5
σ	Surface tension of liquid, page 5
ξ	Dimensionless wall amplitude, page 70
ξ	Elementwise coordinate in streamwise direction of the computational domain, page 20
ζ	Steepness of wall corrugation, page 70

Subscripts

C	Continuity equation, page 22
i	i-th node, page 20
K	Kinematic equation, page 22
M	Momentum equation, page 22
N	Based on the Nusselt solution, page 7
S	Flat substrate far from the main hump, page 32
x, y	Directions of Cartesian coordinate, page 5

Superscripts

n	n-th time step, page 106

Mathematical Symbols

$\bar{}$	Steady quantities of the base flow, page 107

Institutional Repository - Library & Information Centre - University of Thessaly
09/06/2024 06:51:43 EEST - 18.219.33.223

∂	Partial derivative, page 17
$\tilde{}$	Perturbed quantities of the flow, page 107
$\underline{\nabla}$	$(\frac{\partial}{\partial x}, \frac{\partial}{\partial y})$, Gradient operator (Nabla operator), page 17

Nondimensional Numbers

δ	Reduced Reynolds number, page 33
η	Viscous dispersive number, page 33
κ	Shkadov scaling factor, page 55
ζ	Scaled inclination angle, page 33
Bo	Bond number, page 13
Bo^{-1}	Inverse Bond number, page 70
Ca	Capillary number, page 19
Fr	Froude number, page 41
k	Wave number, page 9
Ka	Kapitza number, page 8
Re_{cr}	Critical Reynolds number, page 8

Note: Only the most important symbols are listed above. The symbols are defined the first time they are used. Symbols are also subject to alteration on occasion.

Institutional Repository - Library & Information Centre - University of Thessaly
09/06/2024 06:51:43 EEST - 18.219.33.223

CHAPTER I

Introduction

1.1 Description of the Project in the Dissertation

1.1.1 Scope and Aims of the Dissertation

This dissertation presents a two-dimensional computational work by the integration of the Navier-Stokes equation system using the Galerkin Finite Element Method to study a gravity-driven liquid film flowing along either flat substrate, or sinusoidal topography. It deals with the Newtonian liquid characterized by its kinematic viscosity, surface tension, and density, on the condition of isothermal flow, no heat and mass transfer. The base substrate is a kind of no slip and no penetration.

The whole investigation in this dissertation can be divided into four particular studies. The first work is for falling film flows down a flat wall, provides an understanding of the extreme solitary wave and its properties in terms of flow inertia and liquid properties. Also dealing with the same flow, the second work is to investigate the bound-state formation of solitary waves down falling liquid films and documents the intrinsic bound-state separation distances between solitary pulses. Moving on to the inertial film flow along corrugated substrates, the third study systematically delineates the deformation of steady free surface under the imposition of wall corrugation. Parameters varied are the geometric characteristics of the wall (amplitude and length), the capillary lengthscale of the liquid, and the mean film thickness. Results focus on the effect of inertia on free surface deformation and on the creation of recirculation eddies. The last study deals with the development of computational methodology for the time dependent Navier-Stokes equation system, and its linearised version, as well as the numerical study of the stabilising effect of wall corrugation on film flows, and its physical mechanism.

Institutional Repository - Library & Information Centre - University of Thessaly
09/06/2024 06:51:43 EEST - 18.219.33.223

1.1.2 Novelties of the Dissertation

In the four above mentioned topics, the novelties of this dissertation are reported as new ideas, new numerical aspects applied in the topics studied, new numerical predictions of physics of flow presented, as well as thoughts and discussions. In particular, the first work deals with the solitary waves, being stationary in the co-moving frame and in its extreme limit where a large computational domain and a mesh refinement near solitary hump is used. The properties of solitary waves such as phase speed and wave height do not monotonically vary in terms of flow rate, and do depend on liquid properties. These numerical results resolve a controversy between different models of low dimensionality, which provide widely conflicting predictions.

The novelty in the second topic is the bound state formation of solitary waves on falling liquid films. Intrinsic bound-state separations are found and documented by the computation from an initial guess composed of two or three assembled solitary waves separated at desired distances. These initial guesses are fed into numerical code to converge to different bound-state structures of solitary pulses travelling at the same speed and being stationary in a co-moving frame. The separation distances in the three pulses system may deviate significantly from the two pulse system due to the contribution of the third pulse, especially in an asymmetric system of several waves. The study confirms the validity of the weak interaction theory and helps to explain the statistically wide distribution of separation distances in a train of solitary waves.

When wall topography interacts with inertial film flows, it imposes a non-trivial deformation on the free surface coupled with eddy separation around the wall trough. In the third work, we concentrate on the steady solutions of inertial film flows along periodic corrugations, and extensively describes the subcritical and supercritical flow behaviours represented by the free surface deformation and eddy separation. The resonance of free surface with wall corrugation is universally detected in some parametric diagrams. The appearance and suppression of coupled eddy separation is also documented for an applicable manipulation of eddy. A properly tailored surface of an object is conjectured to face less resistance while moving in liquid. Moreover, the computation reproduces successfully the hydraulic jump, bulge hump, standing wave of free surface for flow along corrugated wall at low inclination angle and large wavelength of corrugation.

The last work develops time-dependent computational methods for the full Navier-Stokes equation system and its linearised version. They are exploited to investigate the stabilizing effect by corrugation and the short-wave mode primary instability

Institutional Repository - Library & Information Centre - University of Thessaly
09/06/2024 06:51:43 EEST - 18.219.33.223

by direct numerical simulation (DNS). Flow on the tested wall corrugation is found stable at much larger Reynolds number at which the one on planar wall must be unstable. This confirms the stabilizing effect of this particular corrugation. Above the critical threshold, the evolution of long-wave mode into short-wave mode due to the modulation of periodic corrugations is numerically observed. Hence new mechanism of instability which is a short-wave mode is predicted due to the effect of corrugation to film flows. This preliminary numerical result supports the experimental observation of an enhanced stabilization by wall corrugation in the range of parameters studied.

1.1.3 Scientific Interest, Industrial Application, and Motivations of the Project

The dynamics and stability of thin liquid films have fascinated scientists over many decades. The observations of regular wave patterns in film flows down a windowpane or along guttering, the patterning of dewetting droplets, and the fingering of viscous flows down a slope are all examples that are familiar in daily life. Thin film flows occur over a wide range of length scales and are central to numerous areas of engineering, geophysics, and biophysics. These include nanofluidics and microfluidics, coating flows, flows in heat and mass transfer equipment, intensive processing, lava flows, dynamics of continental ice sheets, tear-film rupture, and surfactant replacement therapy.

These flows have attracted considerable attention in the literature, which have resulted in many significant developments in experimental, analytical, and numerical research in this area. These include advances in understanding dewetting, thermocapillary- and surfactant-driven films, falling films, films flowing over structured, compliant, and rapidly rotating substrates, evaporating films as well as those manipulated via use of electric fields to produce nanoscale patterns. A brief review of some experimental and theoretical results are referred to the monographs by *Alekseenko et al.* (1985), *Chang* (1994), *Oron et al.* (1997), *Craster and Matar* (2009), and *Kalliadasis et al.* (2012) for a more detailed information of the relevant literature and results.

Concentrating on gravity-driven free surface flow, wave evolution on an inclined or vertical falling film is especially an open-flow hydrodynamic instability, which has attracted an extensive study since the pioneering work of Kapitza and his son (*Kapitza and Kapitza*, 1965). Interfacial waves on film flows has been known on one side to enhance heat and mass transfer rates in process equipment such as condensers, falling film evaporators, absorption columns, and two-phase flow reactors, and on the other side, they degrade the quality of film in coating processes.

Institutional Repository - Library & Information Centre - University of Thessaly
09/06/2024 06:51:43 EEST - 18.219.33.223

Specifically, this dissertation deals with the gravity-driven film flows and is motivated by different topical studies. First, due to the largely different and even contradictory prediction reported by several low-dimensional models (*Ruyer-Quil and Manneville*, 2005) about the properties of the extreme solitary wave, the full Navier-Stokes equation computation is carried out on the extreme solitary wave down falling liquid films with twofold purpose: i) presenting a DNS prediction of extreme solitary waves and ii) offering the DNS data for validation of results given by different low-dimensional models.

Second, based on the experimental (*Vlachogiannis and Bontozoglou*, 2001) and numerical (*Malamataris et al.*, 2002a) evidence about possible solitary wave interactions, another work adhering also to falling liquid films is to prove the existence of solitary wave bound states. Here the stationary separation distance between solitary pulses in two-pulse system is rigorously computed. Moreover, the simulation of low-dimensional model (*Pradas et al.*, 2011a) has shown a wide distribution of separation distance in a train of waves. An extension with a three-pulse system is necessary to see the effect of additional pulses which indeed modify the intrinsic separation distances in two-pulse system. Dynamic simulations document various types of pulse interactions: monotonic attraction or repulsion, decaying oscillation, self-sustained oscillation. Especially, the explosive repulsion of pulses at very close separation reveals that there is a minimum separation in a train of many solitary pulses.

Taking into account undulated substrates, the third work aimed at providing a systematic description and insight of the flow behaviour in a broad range of parameters. It recovers the asymptotic results from the Stokes flow and several other information of the flow at finite inertia, which is fragmentarily reported in previous experimental, analytical and numerical literature. Essentially it unifies the physics into distinguished regimes of subcritical, resonance, and supercritical flow.

Noting that experiments and numerics merely report about a delay of instability by wall corrugation. Physical understanding of the new mechanism of stabilization imposed by the wall corrugation on film flow suggests a separate study focused on evolution of perturbation. Computational method is developed to solve the full Navier-Stokes equations for time dependent simulation. Evolution of full flow is subtracted from the base flow to extract the information of perturbation. This study confirms that the base flow along corrugation can be stable at higher Reynolds number than in planar case. Beyond the critical threshold, it is observed that perturbation evolves from long wave to short wave mode. Therefore, wall corrugation imposes a wave modulation and creates a short-wave mode primary instability of film flow.

Institutional Repository - Library & Information Centre - University of Thessaly
09/06/2024 06:51:43 EEST - 18.219.33.223

1.2 Background Information on Liquid Film Flow

1.2.1 Theoretical Formulation

The two-dimensional governing equations for a gravity-driven flow, as sketched in Fig. 1.1, of a Newtonian incompressible liquid with density ρ, dynamic viscosity μ, and surface tension σ are expressed in dimensional form from the universal laws of continuity in Eq. (1.1), momentum conservation in Eqs. (1.2),(1.3), and are coupled with the kinematic evolution in Eq. (1.4) of free surface as following,

$$\frac{\partial u}{\partial x} + \frac{\partial v}{\partial y} = 0, \tag{1.1}$$

$$\rho\left(\frac{\partial u}{\partial t} + u\frac{\partial u}{\partial x} + v\frac{\partial u}{\partial y}\right) = -\frac{\partial p}{\partial x} + \mu\left(\frac{\partial^2 u}{\partial x^2} + \frac{\partial^2 u}{\partial y^2}\right) + \rho\, g_x, \tag{1.2}$$

$$\rho\left(\frac{\partial v}{\partial t} + u\frac{\partial v}{\partial x} + v\frac{\partial v}{\partial y}\right) = -\frac{\partial p}{\partial y} + \mu\left(\frac{\partial^2 v}{\partial x^2} + \frac{\partial^2 v}{\partial y^2}\right) + \rho\, g_y, \tag{1.3}$$

$$\frac{\partial h}{\partial t} + u\frac{\partial h}{\partial x} - v = 0. \tag{1.4}$$

where g_x and g_y are two components of the gravitational acceleration g projected respectively on x and y directions, $g_x = g\sin\alpha$ and $g_y = -g\cos\alpha$.

The Navier-Stokes equation is a second-order differential equation for the velocity with respect to the spatial coordinates. To compute a solution, one scalar boundary condition is required for each component of the velocity or traction over each boundary. Over an impermeable solid surface, the no-slip and no-penetration boundary conditions are required. Over a free surface, the normal component of the traction is required to be equal to the ambient pressure increased or decreased by an amount that is equal to the product of the surface tension and the curvature of free surface, and the tangential component be equal to the Marangoni traction due to spatial variations in surface tension along the free surface. Finally, a periodic boundary condition is imposed for the inflow and outflow of the computational domain. These boundary conditions will be specified in more detail in the respective studies.

1.2.2 Nusselt Solution of the Steady Film Flow down an Inclined Planar Wall

Consider the flow of a film of thickness h down a plane wall that is inclined by the angle α with respect the horizontal, as illustrated in Fig. 1.1. The no-slip boundary

Institutional Repository - Library & Information Centre - University of Thessaly
09/06/2024 06:51:43 EEST - 18.219.33.223

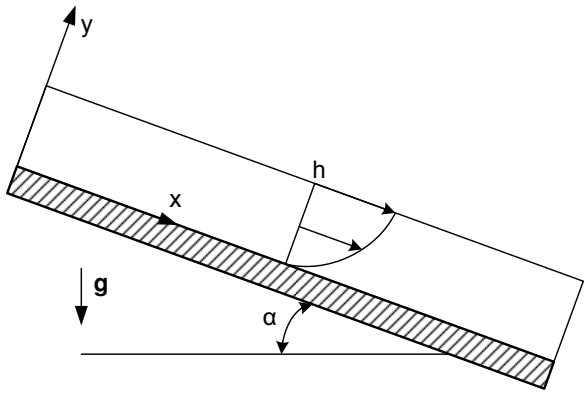

Figure 1.1: Sketch of a steady gravity-driven film flow down an inclined wall

condition requires that the velocity vanishes at the plane located at $y = 0$; the free surface condition requires that the shear stress vanishes at the free surface located at $y = h$. Under the assumption of unidirectional flow, the motion of the fluid is governed by the simplified equations of motion, Eqs. (1.5) and (1.6), by discarding terms that are identically equal to zero as follows,

$$0 = -\frac{\partial p}{\partial x} + \mu \frac{d^2 u}{dy^2} + \rho g_x, \tag{1.5}$$

$$0 = -\frac{\partial p}{\partial y} + \rho g_y, \tag{1.6}$$

subject to the aforementioned boundary and free-surface conditions expressed by

$$u = 0 \text{ at } y = 0, \tag{1.7}$$

$$\frac{du}{dy} = 0 \text{ at } y = h. \tag{1.8}$$

The pressure distribution is given by integrating the equation Eq. (1.6) with respect to y, with no pressure gradient in x direction, yielding

$$p(y) = P_0 + \rho\, g_y\, y,$$

where $g_y = -g \cos\alpha$. Setting the pressure at the free surface equal to the ambient atmospheric pressure, $P_{atm} = P_0 + \rho\, g_y\, h$ or $P_0 = P_{atm} - \rho\, g_y\, h$, leads to

$$p(y) = P_{atm} + \rho\, g\, \cos\alpha\, (h - y). \tag{1.9}$$

Institutional Repository - Library & Information Centre - University of Thessaly
09/06/2024 06:51:43 EEST - 18.219.33.223

Integrating twice the second-order linear ordinary differential equation (1.5) with respect to y, then applying the boundary conditions (1.7) and (1.8), it gives the so-called Nusselt velocity of semi-parabolic profile and its maximum value on the free surface as

$$u(y) = \frac{\rho\, g\, \sin\alpha}{2\mu} y(2h - y), \tag{1.10}$$

$$u_{max} = u(h) = \frac{\rho\, g\, \sin\alpha}{2\mu} h^2. \tag{1.11}$$

The flow rate per unit width is obtained by integrating the velocity across the film,

$$q = \int_0^h u(y)\, dy = \frac{g\, \sin\alpha\, \rho\, h^3}{3\mu}. \tag{1.12}$$

Given the flow rate q and the kinematic viscosity of the liquid $\nu = \mu/\rho$, the mean film thickness, h_N, of a wavy film flow is calculated based on the Nusselt solution as follows,

$$h_N = \left(\frac{3\, q\nu}{g\, \sin\alpha} \right)^{1/3}. \tag{1.13}$$

Also defining the mean film velocity of the Nusselt solution, u_N, by $q = h_N\, u_N$ gives

$$u_N = \frac{h_N^2\, g\, \sin\alpha}{3\nu} = \frac{2}{3} u_{max}. \tag{1.14}$$

The existence of an explicit relation (1.12) between flow rate and depth suggests that any gradual or long-wave disturbance from the uniform state would be propagated downstream with a (dimensional) velocity $c = dq/dh$,

$$c = \frac{h^2\, g\, \sin\alpha}{\nu} = 3u_N = 2u_{max}. \tag{1.15}$$

This simple result provides an interesting check on low-dimensional model analysis as well as a confirmation for the DNS result on solitary wave in Chapter III that very long waves developed near the critical threshold propagate with a phase velocity equal to three times of the mean velocity.

Institutional Repository - Library & Information Centre - University of Thessaly
09/06/2024 06:51:43 EEST - 18.219.33.223

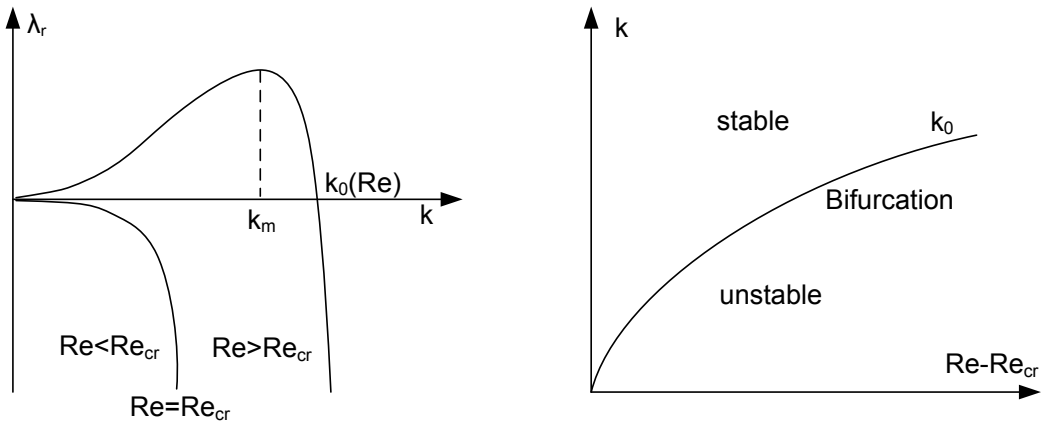

Figure 1.2: Schematic of the growth rate λ_r as a function of streamwise wave number k, and the neutral curve for the neutral wave number k_0 as a function of Reynolds number Re. The critical Reynolds number for the long wave is $Re_{cr} = \frac{5}{6}\cot\alpha$. The bifurcation of the stationary periodic wave family is also indicated, cf. the review by *Chang* (1994).

1.2.3 Linear Stability Analysis

Early literature on linear instability, beginning with the classical long-wave results by *Benjamin* (1957) and *Yih* (1963), address the convective instability by tackling the full Orr-Sommerfeld equation derived from the the linearised Navier-Stokes equation system. *Benjamin* (1957), by using the Orr-Sommerfeld equation which is accurate for infinitesimal amplitude disturbance on film flows down the vertical plane, gave the correct critical Reynolds number for long wave instability,

$$Re_{cr} = \frac{5}{6}\cot\alpha. \tag{1.16}$$

That means instability of very long waves on the vertical film flow occurs beyond $Re_{cr} = 0$, or in other words for all finite Reynolds number. In an analogue of Squire's theorem, the two-dimensional disturbances of the form $f(y) = exp(i\,k\,x+\lambda t)$ are found to be more unstable than three-dimensional disturbances. From the review by *Chang* (1994), the growth rate λ_r shown in Figure 1.2, is a parabolic one that encompasses the range $k \in (0, k_0)$ with k_0 the neutral wave number. The domain of linearly unstable modes in the case of a vertical plane is $0 < k < k_0$, with $k_0 = \sqrt{6Re/(5Ka)}$ where Ka is the Kapitza number defined later in Eq. (2.10). Using the IBL model by *Shkadov* (1967) with the scaled Reynolds number defined as $\delta = Re^{11/9}Ka^{-1/3}5^{-1}3^{-7/9}$ (Note that δ by Skadov has a coefficient 45 times smaller than the one, given in Chapter III,

Institutional Repository - Library & Information Centre - University of Thessaly
09/06/2024 06:51:43 EEST - 18.219.33.223

derived from the WRIBL method (*Ruyer-Quil and Manneville*, 1998, 2000)), Chang showed that in the limit of low flow rate ($\delta \to 0$), the neutral wave number k_0 approaches $\sqrt{18\delta}$. Destabilization of long waves is due to gravity-driven inertia and stabilization of short waves is due to capillary effects. In the same limit of low δ, the fastest growing mode is $k_m = k_0/\sqrt{2} = \sqrt{9\delta}$. Also at low δ, the normalized phase velocity $C = -\lambda_i/k$ is exactly 3 for all wave numbers k, e.g. all Fourier modes travel at three times the average velocity.

For linear disturbances of wave number $k = 2\pi/L$ where L is scaled with viscous length l_ν, another earlier work by *Gjevik* (1970) on the Orr-Sommerfeld equation gave the neutral curve and the curve of maximum rate of amplification. These results for short wave disturbance manifest a dependence on the liquid properties (involving the Kapitza number Ka) and can be written,

$$Re_{cr} = \frac{5}{6}(\cot\alpha + Ka\,k^2), \tag{1.17}$$

$$Re_{max} = \frac{5}{6}(\cot\alpha + 2Ka\,k^2). \tag{1.18}$$

By the need to study efficiently the flow evolution far beyond the critical threshold, several low-dimensional models were developed. One of the most popular models is Benney equation (*Benney*, 1966), which was found to display unphysical solutions that grow indefinitely in time (*Pumir et al.*, 1983; *Rosenau et al.*, 1992; *Oron and Gottlieb*, 2002; *Scheid et al.*, 2005; *Gottlieb and Oron*, 2004). An alternative model is a set of two evolution equations derived by *Shkadov* (1967) using the IBL approach which overestimates the critical threshold by a factor 1/6,

$$Re_{cr} = \cot\alpha. \tag{1.19}$$

To overcome many drawbacks, a new approach was introduced by Ruyer-Quil and Manneville (*Ruyer-Quil and Manneville*, 1998, 2000) extending the boundary-layer theory developed by Shkadov, for both first- and second-order approximations to the NS equations, classified as a weighted-residual integral boundary-layer (WRIBL) theory. In Chapter III, we will confirm the complete second-order four-equation model as the most accurate model for a broad range of Kapitza number ($Ka \sim 100 - 10000$) and large range of reduced Reynolds number ($\delta \sim 0 - 10$). The WRIBL technique corrected the inability of the Shkadov model equations to match the linear stability threshold of the system and was found to yield bounded solutions for a larger range

Institutional Repository - Library & Information Centre - University of Thessaly
09/06/2024 06:51:43 EEST - 18.219.33.223

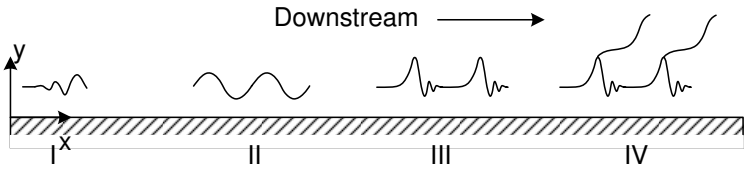

Figure 1.3: Sketch of the four region evolution of the naturally excited film flow.

of Reynolds number than in the case of the Benney equation. More recently, *Oron and Heining* (2008) recovered the same formulation (1.17) for any disturbance of wave number $k = 2\pi/L$, using the WRIBL technique that is credited to Ruyer-Quil and Manneville (*Ruyer-Quil and Manneville*, 1998, 2000), which offers the critical threshold for all long and short wave instability.

1.2.4 Nonlinear Evolution of Film Flows

Wave evolution by natural excitation for Reynolds number well beyond the critical threshold, where the instability consists of long interfacial waves dominated by gravity-capillary effects, is shown in the schematic Figure 1.3, see the review by *Chang* (1994). Four distinct wave regions have been observed.

- Region I: Infinitesimal disturbances at the inlet are amplified downstream, due to convective and not absolute instability, to form a monochromatic wave at the end of the region. If the initial disturbance is sufficiently monochromatic in frequency, the emerging wave inherits the forcing frequency. If the disturbance has a wide band of frequency, as is true with natural noise, a highly selective linear filtering process in region I yields a unique monochromatic wave field for all wideband disturbances.

- Region II: The exponential growth is arrested by weakly nonlinear effects as the amplitude of the monochromatic wave saturates to a finite value depending on the wave number, Re, and Ka. Neighbouring waves coalesce at intermittent locations due to a subharmonic instability (*Prokopiou et al.*, 1991) or a long-wave modulation which appears characteristic of sideband instability.

- Region III: Due to the coalescence, radiation and interaction of waves (*Malamataris et al.*, 2002a), the pulse waves grow in wavelength, amplitude, and speed and evolve into characteristic spatially localized teardrop humps. These humps have steep fronts which are relaxed by a series of front-running ripples. The whole structure

Institutional Repository - Library & Information Centre - University of Thessaly
09/06/2024 06:51:43 EEST - 18.219.33.223

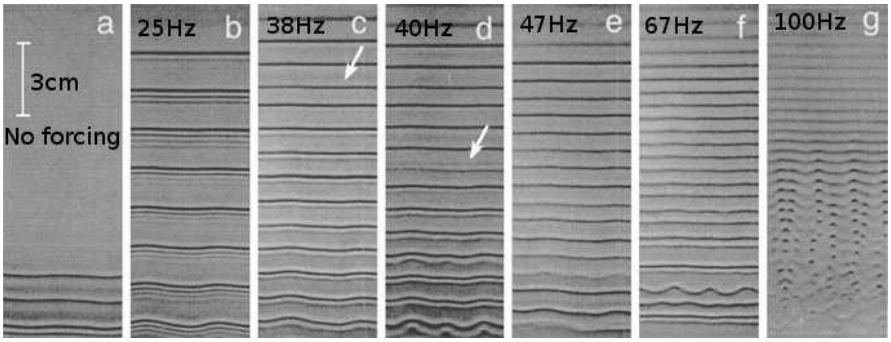

Figure 1.4: Shadow images of waves on a water film flowing down a vertical plate at Re = 52. With the exception of the first panel on the left, the inlet flow rate is periodically forced at the frequencies indicated in the upper right corner of each panel (in Hz). The white arrows indicate the appearance of double-peaked waves, from *Nosoko and Miyara* (2004).

in combination is called solitary wave or solitary pulse. In Chapter 3, the extreme solitary wave is shown to grow monotonically exponentially at downwind side, and to decay oscillatorily and exponentially at upwind side, and to leave a nearly flat liquid substrate far from the main hump between the solitary wave. Interaction of solitary waves leads eventually to the train of fully developed solitary waves, where their shape, phase speed, and wave height are nearly identical in the bound state formation (*Nguyen et al.*, 2012) at downstream.

- Region IV: At high enough Re, inertia effect causes a transverse variation, which begins to develop on the wave crests of the solitary humps. The dynamics of the transverse variation is nonstationary and these transverse variations grow to such amplitude (not in height but in the direction parallel to the wall) that adjacent crests merge at various points and pinch off.

For a forcing disturbance of frequency f to inlet flow rate, two cases can be distinguished dependent on the frequency f.

- A low-frequency finite-amplitude disturbance emerges into the region III of solitary waves right after bypassing the region I of infinitesimal one, as shown in panel b of Figure 1.4.

- However, a high forcing frequency is observed to produce train of monochromatic waves of the same frequency dominant in the extended region II. In region III, due to

Institutional Repository - Library & Information Centre - University of Thessaly
09/06/2024 06:51:43 EEST - 18.219.33.223

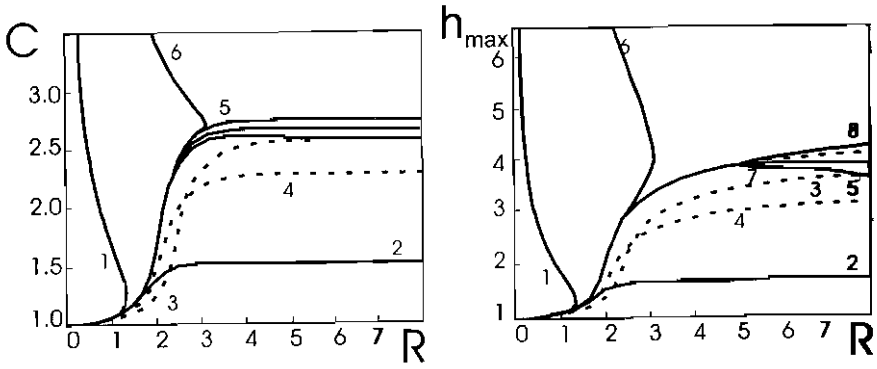

Figure 1.5: Phase speed C and maximum height H versus Reynolds number by different low-dimensional models, from *Chang et al.* (2002).

the close distance between solitary pulses, there are complex dynamical interactions of attractive, repulsive, and oscillatory separation distance, coupling with the mass exchange between solitary waves as described by *Nguyen et al.* (2012) as well as their coalescence and radiation by *Malamataris et al.* (2002a).

The above evolution of film flow on a planar wall attracted several studies to develop different low-dimensional models with different number of degree of freedom and order of accuracy. Although their descriptions on the film flow predict quite similar behaviour at the beginning of supercritical stage, the numerical results on the fully developed solitary wave deviate significantly from each other.

As Figure 1.5 depicts the numerical prediction of solitary wave properties (the phase speed and wave height) in terms of Reynolds number, results given by different low-dimensional models are very divergent. Moreover, the latter don't recognize the diffusive effect of viscosity and the characteristics of wave were incorrectly described to be independent on liquid properties. Based on the full statement of Navier-Stokes equation system, one of my topical study focuses on the fully developed solitary wave in the region III, to predict rigorously the stationary properties of extreme solitary wave in Chapter III, therein, making a conclusion on the complete four-equation model by *Ruyer-Quil and Manneville* (2000) as the most accurate. Next working still on the solitary waves, their bound state formation in a two pulse, then a three pulse system is investigated in Chapter IV, which explains the relative regularity of a train of solitary waves as well as the wide distribution of pulse separation distance in a multiple solitary pulse system.

Institutional Repository - Library & Information Centre - University of Thessaly
09/06/2024 06:51:43 EEST - 18.219.33.223

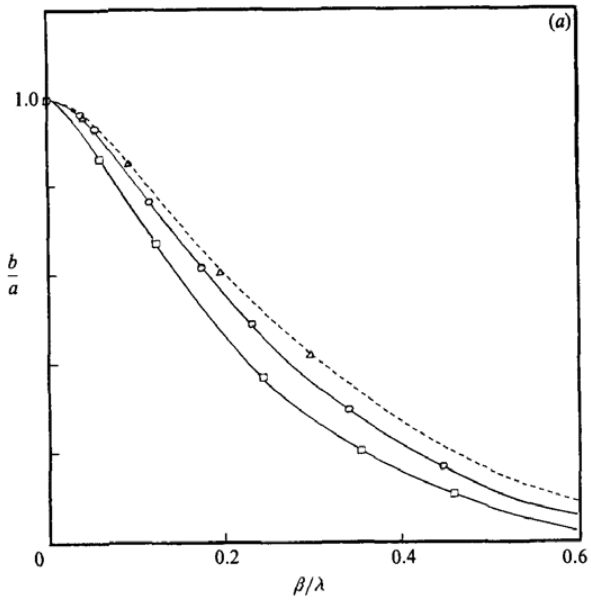

Figure 1.6: Amplitude b/a of the free surface as a function of the film thickness β/λ, for inclination angle $\alpha = 45°$, $Bo = \infty$, and different wave amplitudes: $\triangle$, $a/\lambda = 0.01$; $\bigcirc$, 0.10; $\square$, 0.20. Dashed line shows predictions of asymptotic theory for small a/λ and a/w by *Wang* (1981), from *Pozrikidis* (1988).

1.2.5 Corrugated Walls

There are several studies on the steady solutions of film flow along undulated substrate. The early numerical computation by *Pozrikidis* (1988) was carried out for Stokes flow (Reynolds number $Re \to 0$) (Physically it means a flow of very viscous liquid). Two cases of liquid film flowing along undulated wall were studied in comparison with asymptotic analysis by *Wang* (1981).

For a wall of amplitude a being very small compared both to its wavelength λ and the film thickness at the crest w, the flow tends to follow closely the wall profile. That assumption facilitates an asymptotic analysis (*Wang*, 1981). A good agreement between the results given by numerical method and asymptotic analysis was found as shown in Figure 1.6. Starting with a maximum deformation of nearly $b/a = 1$ (b is the amplitude of free surface deformation and a the wall amplitude) at very small flow rate, the free surface gain smoothness with the film thickness. In three cases of wall amplitude, due to assumption of large wavelength compared to capillary effect (or $Bo = \infty$), this flow is actually interpreted as being totally in the supercritical regime (defined in Chapter V). Therefore, the free surface deformation decreases with flow rate whose inertial effect tends to straighten free surface.

However, when the capillary force is dominant in accordance with a small Bond

Institutional Repository - Library & Information Centre - University of Thessaly
09/06/2024 06:51:43 EEST - 18.219.33.223

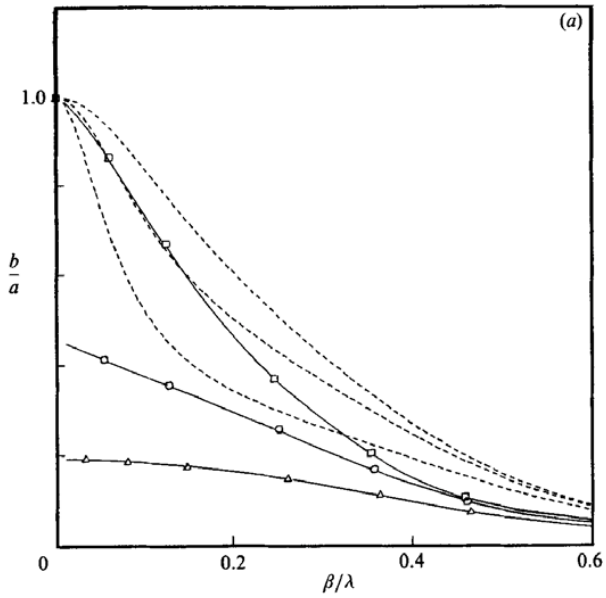

Figure 1.7: Effect of Bond number on the amplitude b/a of the free surface as a function of the film thickness β/λ, for inclination angle $\alpha = 45°$, $a/\lambda = 0.2$, and: $\square$, $Bo = \infty$; $\bigcirc$, 0.5; $\triangle$, 0.2. Dashed line shows predictions of asymptotic theory for small a/λ and large β/λ by *Wang* (1981), from *Pozrikidis* (1988).

number, the capillarity tends to be against the free surface deformation at low flow rate, where flow is in the subcritical regime as defined in Chapter V. The numerical results shown in Figure 1.7 for small Bond number are not in agreement with asymptotic analysis. In fact, the flow should exhibit a resonance of free surface deformation due to the interaction with the corrugated wall when both capillary and inertia effect interplays as high enough flow rate. We can find that the linear resonance was more appropriately predicted by *Bontozoglou and Papapolymerou* (1997) using the extended Orr-Sommerfeld equation and analytically analysed by *Wierschem et al.* (2008) under the assumption of infinitesimal corrugation amplitude.

Therefore at finite Reynolds number, the flow is quite different from Stokes flow. The free surface deformation is not monotonic and exhibits a maximum with respect to Reynolds number (hence flow rate). Looking at Figure 1.8, the free surface increasingly deforms with the flow rate, then reaches a maximum when both capillary and inertial effects have the same magnitude and hence allow a largest deformation. To higher Reynolds number, inertia takes over other forces and hence the flow seems to be able to bridge the gap between two consecutive crests without following closely the bottom wall. Other later studies working on periodic corrugation whose wavelength is comparable to the capillary length of liquid also describes a pronounced

Institutional Repository - Library & Information Centre - University of Thessaly
09/06/2024 06:51:43 EEST - 18.219.33.223

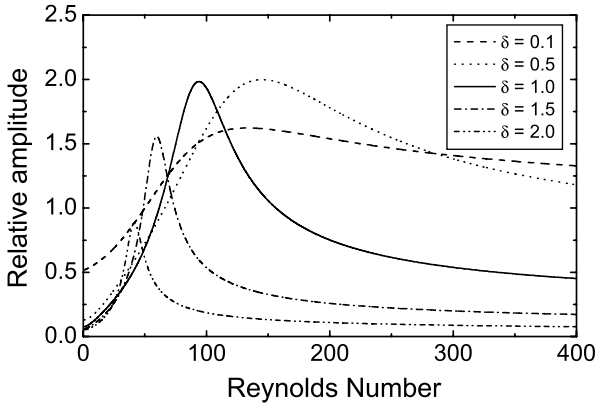

Figure 1.8: The resonance curve for different film thicknesses, from *Wierschem et al.* (2008).

resonance at intermediate flow rate. In particular, a nonlinear resonance was numerically studied for strongly undulated wall by *Heining et al.* (2009), and therein analytically approached provided that the film thickness is very thin compared to other characteristic lengths. It was also numerically found based on the full Navier-Stokes computation with the free outflow boundary condition by *Malamataris and Bontozoglou* (1999) for the S and C-shaped corrugation.

Moreover, the complex matrix of parameters makes the steady flow along undulated wall exhibit several physical phenomena. One is the coupling of free surface and the eddy separation in the bottom of wall. Eddy separation was experimentally investigated by *Wierschem and Aksel* (2004b) to delineate the influence of inertia on its size. For corrugation wall of large wavelength, the experiment by *Wierschem and Aksel* (2004a) well documented other interesting free surface deformation such as hydraulic jump, bulge, and fingering phenomena. For a thick-film flow, the competing geometric and inertial effects to the local flow structure was solved semianalytically for Stokes flow and numerically for inertial one. It suggests the possibility to manipulate the appearance and disappearance of the eddy separation in the bottom wall, which was recently studied thoroughly by computation and experiment of *Wierschem et al.* (2010). As these numerous works show fragmentary information on the topic, the study in Chapter V aims at providing a more comprehensive, broad range parametric description with physical explanation and insight. The work also attempts to relate the experimental data, the analytical approach with numerical predictions, and to unify several same physical observations at different parameters into some parametric maps (*Nguyen and Bontozoglou*, 2011).

Regarding the flow instability, corrugation wall is proved to impose a stabiliz-

Institutional Repository - Library & Information Centre - University of Thessaly
09/06/2024 06:51:43 EEST - 18.219.33.223

ing effect on the free surface under some specific conditions. Several works based on the low-dimensional models was carried out to describe the instability of flow by *D'Alessio et al.* (2009), flow evolution by *Oron and Heining* (2008), the long-wave disturbance on free surface of liquid film flowing along corrugation of the short wavelength by *Davalos-Orozco* (2007). The substantially important work based on the full Navier-Stokes equations was done by *Trifonov* (2007) who parametrically documented the instability of vertical liquid film along corrugation and also found the region of stabilizing effect of wall amplitude. However, the physical mechanism behind the stabilizing effect is still unknown and can be a topical discussion in Chapter VI.

Institutional Repository - Library & Information Centre - University of Thessaly
09/06/2024 06:51:43 EEST - 18.219.33.223

CHAPTER II

Computational Methodology: Finite Element Method

2.1 Theoretical Formulation

This study deals with two-dimensional, laminar, incompressible thin film flow of Newtonian liquids either along a flat wall (Chapter III and IV) or periodic corrugations (Chapter V and VI), driven down by the gravity. It works on isothermal case and there is no mass and heat exchange across the wall and free surface boundaries of physical domain. The problem is modelled as two-dimensional in a Cartesian coordinate system, with the x-axis pointing in the mean flow direction and the y-axis across the film. The respective dimensional velocity components are u and v. The liquid is characterized by the density ρ, the dynamic viscosity μ, and the surface tension σ. The primitive flow input is the mean-time volumetric flow rate q per unit spanwise and the location of the free surface is described as $y = h(x,t)$. The governing equations that express the principles of mass and momentum conservation augmented by the kinematic condition of no mass penetration are non-dimensionalised as follows,

$$\mathbb{C} := \underline{\nabla} \cdot \underline{U} = 0, \tag{2.1}$$

$$\mathbb{M} := \frac{\partial \underline{U}}{\partial T} + \underline{U} \cdot \underline{\nabla}\,\underline{U} - \underline{\nabla} \cdot \underline{\underline{T}} - \frac{3}{Re \sin\alpha}\underline{g} = \underline{0}, \tag{2.2}$$

$$\mathbb{K} := \frac{\partial H}{\partial T} + U\frac{\partial H}{\partial X} - V = 0. \tag{2.3}$$

Here, capital letters indicate dimensionless variables. $\underline{U} = [U, \quad V]^T$ is the velocity vector in the laboratory frame, P is the pressure, and $\underline{g}$ the unit vector in the direction of the gravity $\underline{g} = [\sin\alpha, \quad -\cos\alpha]^T$, with α the mean inclination angle of the mean

Institutional Repository - Library & Information Centre - University of Thessaly
09/06/2024 06:51:43 EEST - 18.219.33.223

wall to the horizontal plane, and T is the time.

In Eq. (2.2), $\underline{\underline{\mathrm{T}}}$ is the stress tensor that a constitutive equation relates the stress tensor to the deformation of the Newtonian liquids in the flow field as,

$$\tau_{ij} = -p\delta_{ij} + \mu(\frac{\partial u_i}{\partial x_j} + \frac{\partial u_j}{\partial x_i}), \tag{2.4}$$

where $u_{i,j} = (u, v)$ and $x_{i,j} = (x, y)$, or in an explicit and dimensionless form,

$$\underline{\underline{T}} = -P\underline{\underline{I}} + \frac{1}{Re}\begin{bmatrix} 2U_X & U_Y + V_X \\ U_Y + V_X & 2V_Y \end{bmatrix} \tag{2.5}$$

where the dimensionless parameter, Re, is the Reynolds number (the ratio of inertial to viscous forces) as follows

$$Re = \frac{\rho\, q}{\mu} = \frac{\rho \bar{u} \bar{h}}{\mu}, \tag{2.6}$$

where $\bar{u}$ and $\bar{h}$ are characteristic velocity and length of the problem, and ρ and ν are the density and viscosity of the liquid.

The governing equations are solved along with appropriate boundary conditions. The boundaries are divided into artificial and natural. Natural boundaries can be solid wall or free surfaces, as shown in Fig. 2.1.

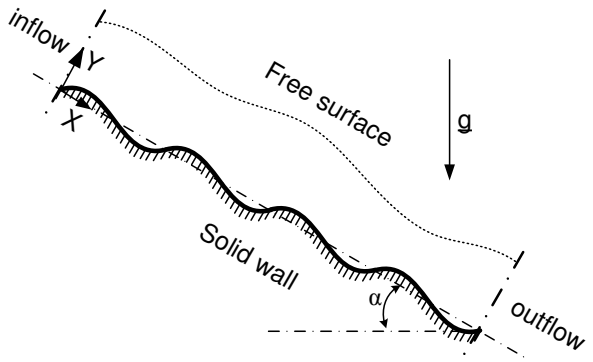

Figure 2.1: Illustration for a prototype of isothermal film flows down an inclined wavy wall.

Along these boundaries, the boundary conditions are imposed by known exchange rates or boundary variable values. At solid walls, there is no mass penetration, no

Institutional Repository - Library & Information Centre - University of Thessaly
09/06/2024 06:51:43 EEST - 18.219.33.223

slip, and no heat exchange.

$$U = V = 0. \tag{2.7}$$

Along the free surface, the shear stress is balanced by the capillary pressure due to the action of the surface tension and the supposedly uniform ambient gas pressure.

$$\underline{n} \cdot \underline{\underline{T}} = \underline{n}\, Ca\, K + \underline{n}\, P_{am} \tag{2.8}$$

In Eq. (2.8), $K = \underline{\nabla} \cdot \underline{n}$ is the curvature of the free surface and $Ca = \sigma\bar{u}/\mu$ the capillary number. If the pressure at one point in the liquid is set as the datum pressure, there is a pressure jump, ΔP between the datum pressure and the uniformed gas pressure. The relation can be rewritten as follows,

$$\underline{n} \cdot \underline{\underline{T}} = \Delta\, P\, \underline{n} + 3^{1/3}\, Ka\, Re^{-5/3}\, K\, \underline{n}. \tag{2.9}$$

$\underline{\mathrm{n}}$ is the outward unit normal vector of the free surface, and $K = \dfrac{H''}{(1+H'^2)^{3/2}}$ the curvature of the free surface.

The Kapitza number, Ka depends only on liquid properties for a fixed inclination and appears in Eq. (2.9),

$$Ka = (\frac{l_c}{l_v})^2. \tag{2.10}$$

The dimensional lengths entering into the above expression are: viscous length, $l_v = (\nu^2/(g\sin\alpha))^{1/3}$, capillary length, $l_c = (\sigma/(\rho g \sin\alpha))^{1/2}$.

The periodic boundary condition is applied for the inflow and outflow in most studied problems. It is physically valid for the steady flow case as well as the stationary-in-comoving frame problem. Thus, it offers an efficient computation without losing physical information. For the unsteady flow along corrugation, we focus only on perturbation evolving from the base flow near the critical threshold, so this condition remains applicable.

2.2 Numerical Method

The governing equations are partial non-linear differential equations that cannot be solved analytically. A numerical solution must be sought if physical predictions are desired. The Galerkin weighted residual Finite Element Method is used, following

Institutional Repository - Library & Information Centre - University of Thessaly
09/06/2024 06:51:43 EEST - 18.219.33.223

the work by *Malamataris* (1991). This technique requires a mapping of the physical domain (X, Y) into a square-shaped computational domain $(\boldsymbol{\xi}, \boldsymbol{\eta})$ by the following isoparametric transformation, where $Y = W(X)$ is the wall profile,

$$X = L\,\boldsymbol{\xi}; \quad Y = (H(X,T) - W(X))\,\boldsymbol{\eta} + W(X). \tag{2.11}$$

The global coordinates of a computational domain, $\boldsymbol{\xi}$ and $\boldsymbol{\eta}$ in a bold font, vary in the range $[0, 1]$. The FEM implementation requires an elementwise application of the governing laws as well as their weak formulations. The computational domain is then divided into rectangular finite elements with frozen or unchanged nodal coordinates $(\boldsymbol{\xi}_i, \boldsymbol{\eta}_i)$ in order to take the Gaussian quadrature on each element. As a result of the mapping, the physical space is correspondingly discretized into quadrilateral finite elements, as shown in Fig. 2.2 with often movable nodal coordinate (X_i, Y_i). The

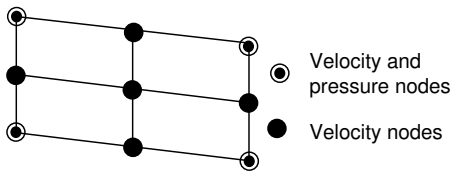

Figure 2.2: A finite element with the attached nodal unknowns.

flow field variables consisting of velocities $\underline{U} = (U, V)$, pressure P, free surface height H, and coordinates $\underline{X} = (X, Y)$ are interpolated from nodal unknowns and nodal coordinates using the Galerkin basis functions,

$$\begin{aligned} \underline{U} &= \sum_{i=1,9} \underline{U}_i\,\phi^i(\xi,\eta), & P &= \sum_{i=1,4} P_i\,\psi^i(\xi,\eta), \\ H &= \sum_{i=1,3} H_i\,\phi^i(\xi,\eta=1), & \underline{X} &= \sum_{i=1,9} \underline{X}_i\,\phi^i(\xi,\eta). \end{aligned} \tag{2.12}$$

Here, ξ and η in a normal font are the elementwise coordinates, varying in the range $[-1; 1]$, of a specified finite element in the computational domain. The Galerkin basis functions used in the above formulation are $\phi^i(\xi,\eta)$ (i = 1, 9) known bi-quadratic, $\psi^i(\xi,\eta)$ (i = 1, 4) known bi-linear, and $\phi^i(\xi,\eta = 1)$ (i = 1, 3) known quadratic bases over a prototype element shown in Fig. 2.3. All elements of the computational domain are transformed into the standard biquadratic element of Fig. 2.3 by means of the isoparametric transformation. The pressure appearing in the stress tensor of Eq. (2.2) is expanded with bi-linear basis functions to conform with the viscous components of total stress, since the velocity is expanded with bi-quadratic

Institutional Repository - Library & Information Centre - University of Thessaly
09/06/2024 06:51:43 EEST - 18.219.33.223

basis functions, otherwise spurious pressure may appear (*Olson*, 1977; *Sani et al.*, 1980).

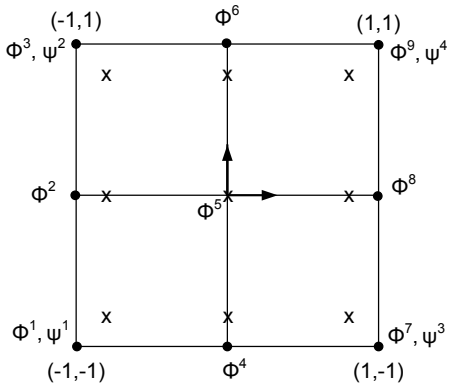

Figure 2.3: Standard finite element with biquadratic, ϕ^i, and bilinear, ψ^i basis functions and Gauss integration points $(0,0)$, $(0,\pm 0.77)$, $(\pm 0.77,0)$, $(\pm 0.77,\pm 0.77)$, $(\mp 0.77,\pm 0.77)$.

Biquadratic basis functions are:

$$\phi^1 = \frac{1}{4}\xi(\xi-1)\eta(\eta-1) \qquad \phi^2 = \frac{1}{2}\xi(\xi-1)(1-\eta^2)$$
$$\phi^3 = \frac{1}{4}\xi(\xi-1)\eta(\eta+1) \qquad \phi^4 = \frac{1}{2}(1-\xi^2)(1-\eta^2)$$
$$\phi^5 = (1-\xi^2)(1-\eta^2) \qquad \phi^6 = \frac{1}{2}(1-\xi^2)\eta(\eta+1)$$
$$\phi^7 = \frac{1}{4}\xi(\xi+1)\eta(\eta-1) \qquad \phi^8 = \frac{1}{2}\xi(\xi+1)(1-\eta^2)$$
$$\phi^9 = \frac{1}{4}\xi(\xi+1)\eta(\eta+1)$$

Bilinear basis functions are

$$\psi^4 = \frac{1}{4}(1-\xi)(1-\eta) \qquad \psi^3 = \frac{1}{4}(1-\xi)(1+\eta)$$
$$\psi^2 = \frac{1}{4}(1+\xi)(1-\eta) \qquad \psi^1 = \frac{1}{4}(1+\xi)(1+\eta)$$

The expansions by the Eqs. (2.12) are introduced into the governing equations and the resulting errors of interpolation is forced orthogonal to all basis functions (*Strang and Fix*, 1973), which is equivalent to minimizing that error to zero:

Institutional Repository - Library & Information Centre - University of Thessaly
09/06/2024 06:51:43 EEST - 18.219.33.223

$$R_C := \iiint_V \mathbb{C}\,\psi^i(\xi,\eta)\,dV = 0, \tag{2.13}$$

$$R_M := \iiint_V \mathbb{M}\,\phi^i(\xi,\eta)\,dV = \underline{0}, \tag{2.14}$$

$$R_K := \int_S \mathbb{K}\,\phi^i(\xi,\eta=1)\,dS = 0. \tag{2.15}$$

The resulting weighted residual, R_M, over the volume V of the computational domain are developed further by the divergence theorem, which decreases the order of differentiation and projects the natural boundary conditions along the boundaries of the domain according to:

$$\underline{\nabla}\cdot(\phi^i\underline{\underline{T}}) = \phi^i(\underline{\nabla}\cdot\underline{\underline{T}}) + \underline{\underline{T}}\cdot\underline{\nabla}\phi^i \tag{2.16}$$

$$\iiint_V \underline{\nabla}\cdot\underline{\underline{T}}\,\phi^i\,dV = \int_S \underline{n}\cdot\underline{\underline{T}}\phi^i\,dS - \iiint_V \underline{\underline{T}}\cdot\underline{\nabla}\phi^i\,dV. \tag{2.17}$$

Here S is the boundary of the domain of volume V and $\underline{n}$ the outward unit normal vector along S. The final form of the weighted residual, Eq. (2.14) becomes,

$$R_M = \iiint_V \left[\left(\frac{\partial\underline{\underline{U}}}{\partial T} + \underline{U}\cdot\underline{\nabla}\,\underline{U} - \frac{3}{Re\sin\alpha}\underline{g}\right)\phi^i + \underline{\underline{T}}\cdot\underline{\nabla}\phi^i\right]\,dV + \int_S \phi^i\underline{\underline{T}}\cdot\underline{n}\,dS. \tag{2.18}$$

The superscript i denotes the i-th node of the computational domain in Fig. 2.3 over which $\phi^i = 1$. Thus the i-th residual equation corresponds to the i-th node where the unknown variables have values U_i, V_i, P_i, H_i. The latter are determined by solving the algebraic system of equations resulting from the discretisation of Eqs. (2.13), (2.15) and (2.18). The discretising technique is employed by the Galerkin FEM in space and by the Crank-Nicolson scheme marching in time. The values of the unknown variables elsewhere are computed by means of Equations (2.12). Essential boundary conditions are applied by replacing the entire governing equations along the appropriate boundary nodes with the corresponding known values of the flow variables. Natural boundary conditions are applied by substituting the surface integral of Equation (2.18) with the appropriate known natural conditions. For confined flow, the equations (2.13) and (2.18) are integrated numerically by the nine-point Gaussian quadrature. A system of algebraic equations is obtained, which is solved

Institutional Repository - Library & Information Centre - University of Thessaly
09/06/2024 06:51:43 EEST - 18.219.33.223

with the Newton-Raphson iteration, and frontal technique (*Hood*, 1976), yielding simultaneously unknown flow variables at the nodal positions of the computation domain and elsewhere by mean of Equations (2.12). For free surface problems, the kinematic condition, Equation (2.3), is added to the governing equations in order to calculate the free surface, H, which is expanded in terms of the quadratic basis functions, $\phi(\xi, \eta = 1)$. Thus, the system of residual equations, Eqs. (2.13), (2.15), and (2.18), resulting respectively from the governing equations Eqs. (2.1), (2.3), and (2.2), is simultaneously solved for the set of unknown variables (velocity $\underline{U}$, pressure P, and free surface height H).

Institutional Repository - Library & Information Centre - University of Thessaly
09/06/2024 06:51:43 EEST - 18.219.33.223

CHAPTER III

Extreme Solitary Wave

The material presented in this chapter is a part of collaborative work with the *Fluides, Automatique et Systemes Thermiques* (FAST) lab, *Centre National de la Recherche Scientifique*, in the *University of Pierre and Marie Curie*, in Orsay, France. This chapter is an extended version of a manuscript in preparation entitled *Extreme Solitary Waves down Falling Film Flow* by P.-K. Nguyen, S. Chakraborty, C. Ruyer-Quil and V. Bontozoglou. My specific contribution to this work is to compute the true solitary waves on a sufficiently large domain length, based on DNS using the clustering grid and to confirm that the complete second-order model is the most accurate one as derived by Ruyer-Quil & Manneville (*Ruyer-Quil and Manneville*, 2000, 2002, 2005). To this aim, I specifically developed a numerical code for the Navier-Stokes equations to capture the solitary wave being stationary in the co-moving frame.

3.1 Introduction

Wave evolution on an inclined or vertical falling film is an open-flow hydrodynamic instability, which has attracted extensive study since the pioneering work of Kapitza and his son (*Kapitza and Kapitza*, 1965). Interfacial waves on film flows has been known on one side to enhance heat and mass transfer rates in process equipment such as condensers, falling film evaporators, absorption columns, and two-phase flow reactors, and on the other side, they degrade the quality of film in coating processes. A brief review of some experimental and theoretical results are referred to the monographs by *Alekseenko et al.* (1985), *Chang* (1994), *Craster and Matar* (2009), and *Kalliadasis et al.* (2012) for a more detailed information of the relevant literature and results.

Much of the information available for the problem is based on experiments. From experimental observations, waves emerge first as short periodic, near sinusoidal waves

Institutional Repository - Library & Information Centre - University of Thessaly
09/06/2024 06:51:43 EEST - 18.219.33.223

in the inception region (near the inlet) and evolve into long solitary type waves, which are often preceded by one or more small capillary waves (or ripples). These solitary waves might break up into spatially and temporally irregular three-dimensional waves further downstream. A technique introduced in the pioneering work of *Kapitza and Kapitza* (1965) and subsequently adopted by many investigators (*Alekseenko et al.*, 1985; *Liu and Gollub*, 1994; *Tihon et al.*, 2006; *Vlachogiannis et al.*, 2010; *Leontidis et al.*, 2010) is to facilitate observations of wave development by applying a constant-frequency disturbance at the inlet. In this way regular waves are produced, whose form depends to a large extent on the frequency of the forcing. These studies have demonstrated that high-frequency disturbances initially lead to saturated periodic waves, whereas low-frequency disturbances evolve directly into regularly-spaced solitary waves. The latter are characterized by large humps with steep wave fronts and gently sloping tails, preceded by front-running ripples (else called bow waves or precursor waves).

Other investigations have focused on film waves that occur naturally, triggered by random noise (*Tailby and Portalski*, 1962; *Jones and Whitaker*, 1966; *Takahama and Kato*, 1980; *Brauner and Maron*, 1982; *Tihon et al.*, 2006; *Vlachogiannis et al.*, 2010). In that case, the small-amplitude waves at the inception region generally correspond to the linearly most unstable mode, and initially evolve into a multi-frequency, complex pattern. It has been demonstrated (*Liu and Gollub*, 1994; *Tihon et al.*, 2006) that, farther downstream, the film flows produced by either regular high-frequency forcing or by natural noise are eventually dominated by a small number of irregularly spaced solitary humps, which emerge through phenomena of period-doubling and wave merging. The correlation of the celerity and the amplitude of solitary waves is documented in a recent experiment on vertical falling film covering a large range of fluid properties Ka and flow rates We by *Meza and Balakotaiah* (2008)

Extensive theoretical efforts at the problem of film flow have centred on perturbation expansions in a small parameter proportional to the thickness-over-wavelength ratio (accompanied by various order-of-magnitude assumptions for the pertinent dimensionless numbers Re and We). Although natural wave structures resemble the three-dimensional waves with pronounced transverse variations, the waves travel downstream at a relatively constant speed without changing their shapes, suggesting that a local two-dimensional model is sufficient for describing these naturally occurring wave profiles. The purpose of these models is to obtain a simplified low-dimensional description of the film in terms of the streamwise coordinate (x) and time (t). They can be a single evolution equation (*Benney*, 1966; *Chang*, 1994) for the local film

Institutional Repository - Library & Information Centre - University of Thessaly
09/06/2024 06:51:43 EEST - 18.219.33.223

thickness $h(x,t)$ or a pair of evolution equations for the local film thickness $h(x,t)$ and the local flow rate $q(x,t)$ (*Mei*, 1966; *Shkadov*, 1967; *Pumir et al.*, 1983; *Nakaya*, 1989; *Joo et al.*, 1991; *Chang et al.*, 1993; *Lee and Mei*, 1996; *Kliakhandler et al.*, 2001; *Ruyer-Quil and Manneville*, 1998, 2000, 2005; *Scheid et al.*, 2006; *Kalliadasis et al.*, 2012) or a three-equation set based on a cubic stream function for the local film thickness $h(x,t)$, the local flow rate $q(x,t)$ and the local pressure $p(x,t)$ (*Nguyen and Balakotaiah*, 2000) and even up to a set of four equations (*Ruyer-Quil and Manneville*, 2002).

Benney (1966) was credited for using the perturbation method to derive the first simplified model for describing the instantaneous amplitude of surface waves on liquid films. The model is commonly known as the long wave (LW) equation in the literature, written as follows,

$$\partial_t h + \frac{1}{3}\partial_x h \left(h^3 + \frac{2}{5}\delta h^6 \partial_x h - \zeta h^3 \partial_x h + \partial_{xxx} h \right) = 0, \tag{3.1}$$

which describes the evolution of film thickness. Here, δ is the reduced Reynolds number, ζ is the reduced slope. Unfortunately, it is valid only close to the instability threshold and fails to reproduce the behaviour of the film at a close distance from the critical threshold.

A weakly nonlinear truncation of the LW equation gives the Kuramoto-Sivashinsky (KS) equation. Numerical studies of the KS equation by *Sivashinsky and Michelson* (1980) showed that solitary waves generated in a bounded domain with periodic boundary conditions travel at the same speed as predicted from the linear theory. Long wave type equations were also derived and analysed by *Frenkel* (1992, 1993) for flows on cylindrical wires. *Shkadov* (1967, 1968) used the integral boundary layer (IBL) method with a self-similar velocity profile assumption to derive a two-equation model for describing the dynamics of large-amplitude waves.

$$\partial_t h + \partial_x q = 0, \tag{3.2}$$

$$\delta \partial_t q = h - 3\frac{q}{h^2} - \delta \left\{ \frac{12}{5}\frac{q}{h}\partial_x q - \frac{6}{5}\frac{q^2}{h^2}\partial_x h \right\} - \zeta h \partial_x h + h \partial_{xxx} h. \tag{3.3}$$

However, it was shown later that the Shkadov model does not predict the correct Hopf bifurcation (instability threshold), a necessary condition for predicting periodic waves in a moving frame of reference. *Alekseenko et al.* (1985) measured the local velocity components inside the waves and found that they are not self-similar but are close to parabolic. They also measured the wave growth rates, velocities, and amplitudes near

Institutional Repository - Library & Information Centre - University of Thessaly
09/06/2024 06:51:43 EEST - 18.219.33.223

inception. *Trifonov and Tsvelodub* (1991) analyzed the Shkadov model and resolved the problem associated with it by using periodic boundary conditions. Although their numerical simulations showed reasonable agreement with experimental data (near the inception region) at low to moderate Reynolds numbers, the assumption of periodic boundary conditions was questionable. Applying the dynamic singularity theory, Chang (*Chang*, 1994; *Chang et al.*, 1998) derived quantitative correlations between the solitary wave amplitude, velocity, and wavelength and showed that the single frequency waves first appearing on the smooth film evolve into doubly periodic waves, which may then become chaotic just before the solitary wave limit is reached. His work concentrated on the LW and the KS equation and was limited to small Reynolds numbers and high Kapitza (Weber) numbers for which the wave amplitude is very small. Further efforts to enrich the structure of the wave evolution process by retaining higher-order viscous terms and/or adding a third dimension did not result in significant improvement over simpler models (*Prokopiou et al.*, 1991; *Chang et al.*, 1993). Using the boundary collocation method, *Yu et al.* (1991) analysed two models, namely the boundary layer(BL) model and the second-order boundary layer (SBL) model, which were capable of describing the dynamics of large-amplitude waves at high Reynolds numbers. Both models compared well with the linear stability results of the OS equation. The SBL model also included a pressure variation across the film and higher-order viscous terms, which were essential in predicting accurate wall shear stress. In the travelling coordinate, numerical integration of the BL and SBL models predicted large-amplitude waves with peak to substrate ratios of 3 to 4 and agreed well with experimental data. Although the numerical computations using these models were much simpler than the full Navier-Stokes equations, they were still too complicated for general analytical studies. The resulting approximate evolution equations for the film thickness admit stationary travelling solutions. They have been analysed by modern bifurcation theory and have also been numerically scrutinized to yield a rich variety of solutions, including limit cycles, homoclinic orbits, and chaotic attractors (*Chen and Chang*, 1986; *Prokopiou et al.*, 1991; *Demekhin et al.*, 1991; *Trifonov and Tsvelodub*, 1991; *Tsvelodub and Trifonov*, 1989, 1992; *Yu et al.*, 1991).

Especially, along the line with the need for a low-dimensional but accurate model, Ruyer-Quil and Manneville (*Ruyer-Quil and Manneville*, 1998, 2000, 2002, 2005) have derived systematically several low-dimensional models based on the residual method of weighting on polynomial expansion. Their different models were gradually improved by including high-order viscous terms and by regularization. The simplified second-order model by *Ruyer-Quil and Manneville* (2000), coupling with Eq. (3.2),

Institutional Repository - Library & Information Centre - University of Thessaly
09/06/2024 06:51:43 EEST - 18.219.33.223

is as follows,

$$\delta\partial_t q = \frac{5}{6}h - \frac{5}{2}\frac{q}{h^2} - \delta\left\{\frac{17}{7}\frac{q}{h}\partial_x q - \frac{9}{7}\frac{q^2}{h^2}\partial_x h\right\} + \frac{5}{6}h\partial_{xxx}h - \frac{5}{6}\zeta h\partial_x h + \eta\left[4\frac{q}{h^2}(\partial_x h)^2 - \frac{9}{2h}\partial_x h\partial_x q - 6\frac{q}{h}\partial_{xx}h + \frac{9}{2}\partial_{xx}q\right]. \tag{3.4}$$

The terms within the square brackets are generated by the second-order contributions in the momentum equation and the tangential stress boundary condition. For a sake of easy tackling, this is a simplified version of a more important work. The latter has derived the four-equation model which can take into account all characteristics of the full N.-S equations by resorting to a high-order polynomial expansion and adding two independent local degrees of freedom to describe the evolution of finite amplitude waves for a realistic range of parameters. The model is written in vector form, coupling with Eq. (3.2) as follows,

$$\delta\left\{\partial_t\mathbf{A} + \left(\frac{q\partial_x h}{h^2}\mathbf{M_h} + \frac{\partial_x q}{h}\mathbf{M_q}\right)\mathbf{A} + \frac{q}{h}\mathbf{M_A}\partial_x\mathbf{A} + Fr^{-2}h\partial_x h\mathbf{V_b}\right\} = h\left(1+\partial_{xxx}h\right)\mathbf{V_b} - h^{-2}\mathbf{M_w}\mathbf{A}, \tag{3.5}$$

where $\mathbf{A} = (q, s_1, s_2)$ is the amplitude vector and $\mathbf{M_h}$, $\mathbf{M_q}$, $\mathbf{M_A}$, $\mathbf{M_w}$, and $\mathbf{V_b}$ are defined by,

$$\mathbf{M_h} = \begin{bmatrix} \frac{-6}{5} & \frac{12}{5} & \frac{126}{65} \\ \frac{3}{35} & \frac{-108}{55} & \frac{5022}{5005} \\ 0 & \frac{4}{11} & \frac{-18}{11} \end{bmatrix} \qquad \mathbf{M_q} = \begin{bmatrix} \frac{12}{5} & \frac{-12}{5} & \frac{171}{65} \\ \frac{-1}{35} & \frac{103}{55} & \frac{-9657}{5005} \\ 0 & \frac{2}{33} & \frac{19}{11} \end{bmatrix}$$

$$\mathbf{M_A} = \begin{bmatrix} 0 & \frac{-12}{5} & \frac{-1017}{455} \\ 0 & \frac{39}{55} & \frac{-10557}{10010} \\ 0 & \frac{6}{55} & \frac{288}{385} \end{bmatrix} \qquad \mathbf{M_w} = \begin{bmatrix} \frac{81}{28} & 33 & \frac{3069}{28} \\ \frac{3}{10} & \frac{126}{5} & \frac{126}{5} \\ \frac{13}{140} & \frac{39}{5} & \frac{11817}{140} \end{bmatrix} \mathbf{V_b} = \begin{bmatrix} \frac{27}{8} \\ \frac{1}{10} \\ \frac{13}{420} \end{bmatrix} \tag{3.6}$$

Dealing with the full-second order four-equation model is quite complicated. *Ruyer-Quil and Manneville* (2002) later used the Padé approximation technique to regularize the full model to obtain a regularized two-equation model, coupled with Eq. (3.2) as

Institutional Repository - Library & Information Centre - University of Thessaly
09/06/2024 06:51:43 EEST - 18.219.33.223

follows,

$$\begin{aligned}\delta\partial_t q =&\delta\left[\frac{9}{7}\frac{q^2}{h^2}\partial_x h-\frac{17}{7}\partial_x q\right]\\&+\left\{\frac{5}{6}h-\frac{5}{2}\frac{q}{h^2}+\eta\left[4\frac{q}{h^2}(\partial_x h)^2-\frac{9}{2h}\partial_x h\partial_x q-6\frac{q}{h}\partial_{xx}h+\frac{9}{2}\partial_{xx}q\right]\right.\\&\left.-\frac{5}{6}\zeta h\partial_x h+\frac{5}{6}h\partial_{xxx}h\right\}\left[1-\frac{\delta}{70}q\partial_x h\right]^{-1}.\end{aligned}\tag{3.7}$$

This set of equations is consistent at $O(\epsilon^2)$ and differs from the simplified model (3.4) through the addition of the Padé like factor $\left[1-\frac{\delta}{70}q\partial_x h\right]^{-1}$.

Computational attempts on the film flow problem through direct computation based on the full Navier-Stokes equations are not too many. One attractive approach is the numerical integration of the time-dependent equations as an initial-value problem, because it captures the nonlinear, spatial evolution of a convective instability and is thus more amenable to a direct comparison with experiments. The only numerical study that has adopted such an approach is the extensive simulation by *Ramaswamy et al.* (1996) These authors have presented temporal stability results that identify a transition regime characterized by quasiperiodic (instead of fully developed) waveforms, and have also computed the spatiotemporal evolution of inlet disturbances and compared their predicted free-surface profiles with the data of *Liu and Gollub* (1994) An extension of the above study is by *Malamataris et al.* (2002b) for the study of solitary wave interaction using free outflow boundary condition (*Malamataris and Papanastasiou*, 1991; *Malamataris and Bontozoglou*, 1999; *Malamataris*, 1991) in order to ensure smooth exiting of nonlinear waves from the computational domain.

Due to a time consuming computation of unsteady computation, an alternative DNS can be used with the application of the periodic boundary conditions at the inlet and outlet of the flow field to capture the fully developed stationary wave. The pioneering work by *Bach and Villadsen* (1984) was followed by few contributions, (*Kheshgi and Scriven*, 1987; *Ho and Patera*, 1990; *Northey et al.*, 1990; *Salamon et al.*, 1994), which obtained good agreement with data of fully developed nonlinear waveforms. This formulation overcomes the problem of the outflow boundary condition but excludes by definition nonstationary dynamics and aperiodic phenomena such as chaotic waves. On the contrary, periodic and fully developed solitary waves are recovered. Thus, the above studies permit comparisons with stationary solutions, derived from the aforementioned simplified forms of the Navier-Stokes equation based on long-wave expansion. However, characteristics of travelling wave was studied in

Institutional Repository - Library & Information Centre - University of Thessaly
09/06/2024 06:51:43 EEST - 18.219.33.223

part for short waves and at small Reynolds number, and information about solitary wave in the true solitary limit is not yet documented by DNS.

Regarding to the true solitary wave, although most low-dimensional models predict similar behaviours close to the threshold (onset of drag-gravity regime), they exhibit differences from each other at intermediate and higher value of Reynolds number (which is scaled with Kapitza number to give the reduced Reynolds number δ), i.e. when the inertia becomes significant in the transition region and the drag-inertia regime, see Figure 3.1. Hence, a crucial test of such models consists in the

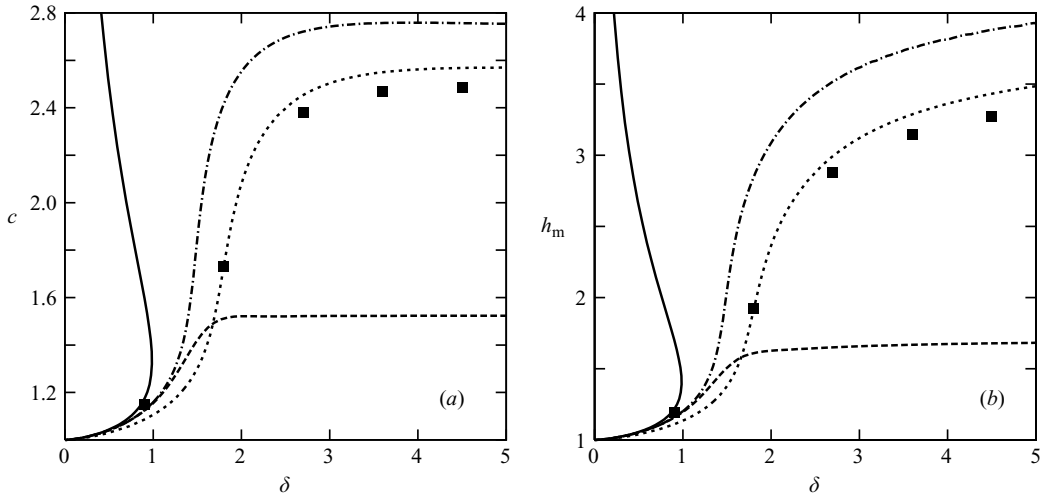

Figure 3.1: Phase speed c and wave height h_m as functions of the reduced Reynolds number δ of the solitary wave, given by different low-dimensional models, from *Ruyer-Quil and Manneville* (2005).

correct predictions of the properties (shape, wave speed and wave height) of solitary wave as a function of the distance from the instability threshold. For that, our direct numerical simulation (DNS) work is done based on the integration of the full two-dimensional Navier-Stokes equation by the Finite Element Method with the application of the periodic boundary condition at the inlet and the outlet. The bottom line is the use of a large enough length of computational domain in order that all the solitary waves approach asymptotically to the true solitary limit. It serves two-fold, first, offering numerical predictions of the extreme solitary wave properties, then using these data to validate the different low-dimensional models. Among them, the four-equation model (*Ruyer-Quil and Manneville*, 2002) is proved to have an excellent agreement to the DNS results and to be considered the most accurate model for further theoretical and applied study perspectives.

The chapter is organized as follows: Problem formulation and finite-element im-

Institutional Repository - Library & Information Centre - University of Thessaly
09/06/2024 06:51:43 EEST - 18.219.33.223

plementation are outlined in Sec. 3.2. In Sec. 3.3, the fully-developed solitary wave is studied and its properties are characterized in terms of different parameters. Comparisons with the different low-dimensional models are made, which prove as the best model to the complete second-order four-equation by Ruyer-Quil and Manneville. Finally, the key properties of extreme solitary wave are summarized in the concluding section 3.4.

3.2 Problem Formulation and Computational Methodology

3.2.1 Governing Equations and the Finite Element Method

This study deals with liquid films flowing along an infinite planar wall, inclined at an angle α with the horizontal plane, which is, in most part of this study, set to 90 degree (Fig. 4.1), except otherwise mentioned. The flow is free of shear force at the gas-liquid interface. The solitary wave is further assumed to be fully developed and hence move at constant speed and have a fixed shape. In this stationary state, the solitary wave can be considered, in the the co-moving reference frame, to move on a base substrate which is undisturbed far away from main hump. If the solitary wave hump is fixed at the middle point of a sufficiently large domain of length L, the liquid substrates near inflow, and outflow regions are practically undisturbed or resemble a flat Nusselt flow so that the periodic boundary can be applied for these two ends.

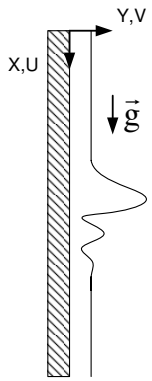

Figure 3.2: The configuration of vertically falling liquid films

The problem is modelled as two-dimensional in a Cartesian coordinate system, with the x-axis pointing in the mean flow direction and the y-axis across the film. The respective dimensional velocity components are u and v. The liquid is incompressible and Newtonian, with density ρ, dynamic viscosity μ, and surface tension σ. The

Institutional Repository - Library & Information Centre - University of Thessaly
09/06/2024 06:51:43 EEST - 18.219.33.223

primitive flow input is the volumetric flow rate q and the location of the free surface is described at stationary state as $y = h(x)$.

The full Navier-Stokes equations governing the two-dimensional flow are non-dimensionalised using as characteristic scales the film thickness and the mean velocity

$$h_S = \left(\frac{3\mu q}{\rho g \sin\alpha}\right)^{1/3} \text{ and } u_S = \frac{g h_S^2 \rho \sin\alpha}{3\mu} \tag{3.8}$$

of the undisturbed substrate far away from the main hump transporting the flow rate q along a planar wall. The resulting equations are formulated at stationary state by the transformation $X \to X - C\,T$ as follows, with capital letters indicating the respective dimensionless variables:

$$\mathbb{C} := \nabla \cdot \underline{U} = 0, \tag{3.9}$$

$$\mathbb{M} := -C\frac{\partial \underline{U}}{\partial X} + \underline{U} \cdot \nabla \underline{U} + \nabla P - \frac{1}{Re}\nabla^2 \underline{U} - \frac{3}{Re \sin\alpha}\underline{g} = \underline{0}, \tag{3.10}$$

coupled with the kinematic equation for free surface evolution

$$\mathbb{K} := -C\frac{\partial H}{\partial X} + U\frac{\partial H}{\partial X} - V = 0, \tag{3.11}$$

where the velocity vector is $\underline{U} = [U, \quad V]^T$, and time derivative term is replaced by spatial derivative one due to the coordinate transformation, $\frac{\partial}{\partial T} = -C\frac{\partial}{\partial X}$. Moreover, we impose the no-slip and no-penetration boundary conditions at the wall,

$$U = V = 0, \tag{3.12}$$

and the dynamics boundary conditions at the free surface,

$$\underline{n} \cdot \underline{\underline{T}} = \Delta P\, \underline{n} + 3^{1/3}\, Ka\, Re^{-5/3}\, K\, \underline{n}. \tag{3.13}$$

In Eq. (3.13), $\underline{\underline{T}}$ is the stress tensor, $\underline{n}$ is the normal vector on the free surface and $K = \frac{H''}{(1+H'^2)^{3/2}}$ the surface curvature. We have 6 variables: two velocity components U and V, pressure P, free surface height H, pressure jump at a reference point in the liquid to the supposedly uniform gas pressure ΔP, and phase speed C. But so far there are only four equations: one from Eq. (3.9), two from Eqs. (3.10), and one from Eq. (3.11). Two additional equations need to be established from imposing the phase

Institutional Repository - Library & Information Centre - University of Thessaly
09/06/2024 06:51:43 EEST - 18.219.33.223

of a steadily travelling wave by
a) pinning the maximum height of solitary wave in the middle of domain (this is to avoid a degeneracy) without loss of generality,

$$H'(x = L/2) = 0, \tag{3.14}$$

b) and setting the thickness of undisturbed substrate far away from the main hump

$$H(x = 0) = 1 \tag{3.15}$$

The dimensionless parameters arising in the governing equations (3.10) are the Reynolds number

$$Re = \frac{\rho\, q}{\mu} = \frac{\rho u_S h_S}{\mu}, \tag{3.16}$$

and the inclination angle, α of the planar wall to the horizontal plane, shown in the unit vector in the gravity direction $\underline{g} = [\sin\alpha, \quad -\cos\alpha]^T$. The Kapitza number depending only on liquid properties, appears in Eq. (3.13),

$$Ka = (\frac{l_c}{l_v})^2. \tag{3.17}$$

The dimensional lengths entering into the above expressions are: viscous length, $l_v = (\nu^2/(g\sin\alpha))^{1/3}$, capillary length, $l_c = (\sigma/(\rho g \sin\alpha))^{1/2}$, and thickness of the undisturbed substrate, h_S, which is far away from main hump, and used as a characteristic scale length.

Alternatively, three other dimensionless parameters, a reduced Reynolds number δ, a viscous dispersion number η, and a scaled inclination ζ) are often used in the low-dimensional model analysis (*Ruyer-Quil and Manneville*, 1998, 2000, 2002) or the falling film studies (*Kalliadasis et al.*, 2012; *Ruyer-Quil and Manneville*, 2005; *Scheid et al.*, 2006) and related to the three conventional parameters as follows.

$$\delta = (3Re)^{11/9} Ka^{-1/3} = \frac{h_s^{11/3}}{l_\nu^3 \quad l_c^{2/3}}, \tag{3.18}$$

$$\eta = (3Re)^{4/9} Ka^{-2/3}, \tag{3.19}$$

$$\zeta = \cot\alpha (3Re)^{2/9} Ka^{-1/3}. \tag{3.20}$$

In order to make a comparison of solitary wave properties given by the low-

Institutional Repository - Library & Information Centre - University of Thessaly
09/06/2024 06:51:43 EEST - 18.219.33.223

dimensional models and DNS computation, only two parameters δ and Ka are needed as control data to represent respectively the significance of the inertial effect and the liquid properties.

Using the Galerkin finite element method on a structured mesh, the system of governing equations is integrally weighted, particularly with bi-linear $\Psi^i(\xi,\eta)$ (i = 1, 4), bi-quadratic $\Phi^i(\xi,\eta)$ (i = 1, 9), and quadratic basic functions $\Phi^i(\xi,\eta=1)$ (i = 1, 3) to produce respectively the residuals of the continuity equation, of the momentum equations, and of the kinematic equation,

$$\iint_V \mathbb{C}\,\Psi^i(\xi,\eta)\,dV = 0,$$
$$\iint_V \mathbb{M}\,\Phi^i(\xi,\eta)\,dV = \underline{0},$$
$$\int_S \mathbb{K}\,\Phi^i(\xi,\eta=1)\,dS = 0.$$

where ξ and η are elementwise coordinates in each element of the computational domain. The flow field variables consiting of velocities U and V, pressure P, and free surface height H are also interpolated from nodal unknowns using these basic functions.

$$\underline{U} = \sum_{i=1,9} \underline{U}_i\,\Phi^i(\xi,\eta),$$
$$P = \sum_{i=1,4} P_i\,\Psi^i(\xi,\eta),$$
$$H = \sum_{i=1,3} H_i\,\Phi^i(\xi,\eta=1).$$

The elementwise integration results in a discretised system of algebraic equations, which is solved by the Newton-Raphson iterative scheme, using a frontal technique.

The solitary wave resulting from the solution of the above system is typically characterized by:
(a) Wave height, H, which is measured at the peak of solitary wave, and scaled with the thickness of the undisturbed substrate (with X dependence, the same letter denotes the free surface height.)

$$H = \frac{h}{h_S},$$

Institutional Repository - Library & Information Centre - University of Thessaly
09/06/2024 06:51:43 EEST - 18.219.33.223

(b) Phase speed, C, which is a constant value of the stationary solitary wave in the co-moving frame, and scaled with the three times of the mean velocity of the undisturbed substrate.

$$C = \frac{c}{3\,u_S}.$$

3.2.2 Mesh Clustering

Following the exponential mesh clustering technique given in the book of *Hoffman and Chiang* (2000), the meshing of the 2D film flow domain is refined in the vicinity of the main hump of solitary wave in the streamwise direction, see Figure 3.3. The

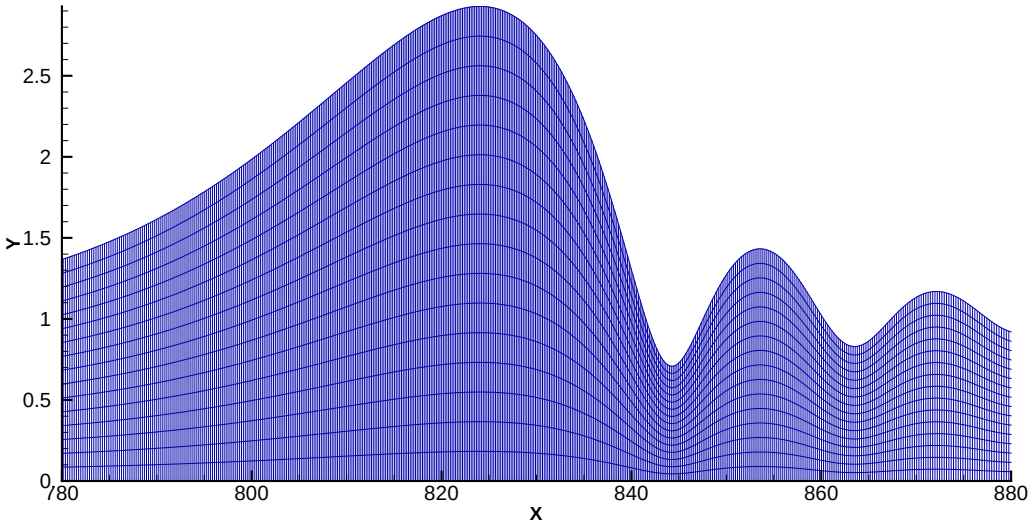

Figure 3.3: Refinement of mesh around the main hump and relaxing in the flat substrates (which is beyond the viewing window).

clustering technique in the interior of the domain is required. In particular, the mesh is clustered around the main hump and capillary ripples, and relaxed in the nearly flat substrate far away from the main hump. The following transformations are used

$$X = L\left\{1 + \frac{\sinh[\beta(\xi - A)]}{\sinh(\beta A)}\right\}, \tag{3.21}$$

$$Y = H(X)\,\eta, \tag{3.22}$$

where

$$A = \frac{1}{2\beta}\ln\left[\frac{1 + (e^{\beta} - 1)(D/L)}{1 + (e^{-\beta} - 1)(D/L)}\right]. \tag{3.23}$$

Institutional Repository - Library & Information Centre - University of Thessaly
09/06/2024 06:51:43 EEST - 18.219.33.223

In the equation (3.21), β is the clustering parameter in the range of $0 < \beta < \infty$, and L the length of physical domain. Physical coordinate Y is scaled with the free surface height $H(X)$ in Eq. (3.22). In Eq. (3.23), D is the X coordinate where clustering is desired, in this case, it is the streamwise location of the maximum height which is pinned in the middle of domain, $D = L/2$. The isoparametric mapping from the physical domain to the rectangular computational domain is done by the transformations (3.21) and (3.22) where ξ and η (the same notation used also for the elemenwise coordinates in each element of computational domain) are the two coordinates of the computational domain in the range $0 < \xi < 1$, $0 < \eta < 1$ and with constant stepsizes $\Delta\xi$ and $\Delta\eta$. In order to capture the solitary wave's properties in asymptotic limit, the domain length should be larger than thousand times of Nusselt flat substrate thickness. In this study, the domain length $L = 3000$ is sufficient to cover a wide parametric range up to either a large flow rate $\delta = 20$ or to a very low viscous liquid of $Ka = 10^4$. Accordingly, the parameter β is defined such that the minimum space step ΔX_{min} should be much smaller than the scaled capillary length, i.e. $N_c \Delta X_{min} \leq l_c/h_s$, where a large factor $N_c = 512$ is empirically chosen. Very small N_c may cause an overshoot or undershoot of solitary wave or a failure of numerical convergence due to low meshing resolution. On the contrary, very large N_c may cause too many elements clustering around the main hump and too few in other parts. To begin, the solitary wave is first computed at a small δ with highly clustering mesh intended for following computations at higher δ. By parametric continuation, this mesh is fixed to compute waves at different parameters. It is not necessary to regenerate the mesh in each computing process, otherwise, the interpolation of nodal unknowns is needed and may cause significant deviation from the previous result and interrupt the continuation process.

3.3 Numerical Results

3.3.1 Extreme Solitary Wave Profile and Characteristics

In Fig. 3.4, the free surface profile shows an exponential growth upstream and oscillatory decay downstream of the main hump in the form of preceding ripples. Hence at a large distance, substrate of the film flow is nearly flat on both sides upstream and downstream. The main hump amplitude is determined in terms of parameters δ, Ka, α, and saturated on a large-length domain, L, of one single wave, see Fig. 3.5. From numerical experience, the dimensional domain length l should be hundreds to thousands times larger than (respectively proportional to the order

Institutional Repository - Library & Information Centre - University of Thessaly
09/06/2024 06:51:43 EEST - 18.219.33.223

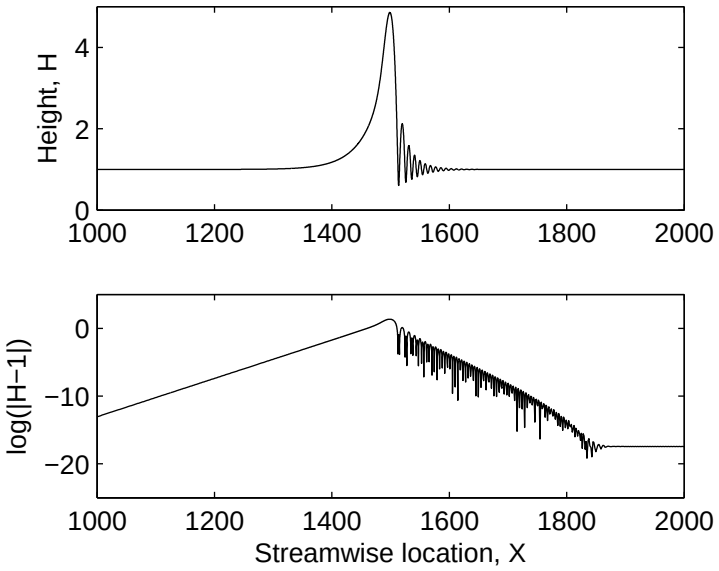

Figure 3.4: Free surface profile of extreme solitary wave and its exponential representation at $\delta = 4$, $Ka = 3400$, $\alpha = 90^{\circ}$, and computational domain length $L = 3000$, in which the nearly flat substrate far from the main hump is out of window.

magnitude of Kapitza number, $Ka \sim 10^0 \div 10^4$) the substrate thickness h_s, in order that solitary wave properties converge asymptotically to true solitary limit. However, the number of elements in the computational domain can be necessarily small by the use of a clustering mesh around the main hump and the ripples, and a relaxed mesh in the nearly flat substrate part of the solitary wave. The clustering mesh is very useful to capture either a steep front of a solitary wave's hump at small Kapitza number or an increasing number of tightly paced ripples in the drag-inertia regime (at medium to large reduced Reynolds number). Especially, clustering grid effectively helps to resolve a zone of a very tall hump preceded by dense ripples at large Ka in order to avoid a numerical overshoot or undershoot of solitary wave's peak. It is also noted that no solution can be provided when approaching to the limiting condition where a parameter set of both small Kapitza and large reduced Reynolds number leads to extremely steep front of solitary wave.

3.3.2 Drag-Gravity, Transition, and Drag-Inertia Regimes

3.3.2.1 Effect of Flow Inertia

In Fig .3.6, it is observed that both the phase velocity and the wave height exhibit inflection points in the transition region, then maxima at intermediate values of δ,

Institutional Repository - Library & Information Centre - University of Thessaly
09/06/2024 06:51:43 EEST - 18.219.33.223

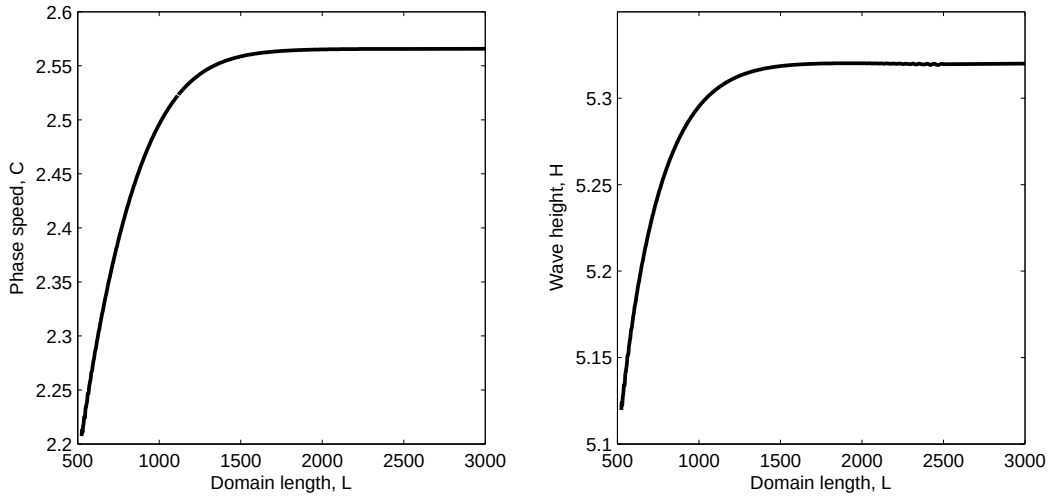

Figure 3.5: The convergence of extreme solitary wave properties in terms of domain length at $\delta = 10$, $Ka = 10^4$, and $\alpha = 90°$.

and finally a drop to a plateau at high enough δ. These are unique characteristics of the full second-order model by *Ruyer-Quil and Manneville* (2002), whereas all other models predict either a monotonic increase or a monotonic, asymptotic limit. In particular, simulations and the above second-order model agree quantitatively in the drag-gravity regime and the transition region to the drag-inertia regime, but only qualitatively in the drag-inertia regime. The behaviour deep in the drag-inertia regime is found to depend on Ka, which in the present simulations is varied in the range 200-10000. With increasing Ka, the maxima that occur at intermediate δ become steeper. However, whereas the high-δ limit of the phase velocity appears almost unaffected, that of the wave height increases roughly linearly with Ka, which underlines the stabilizing effect of viscous diffusion at low Kapitza numbers. It is observed that the maximum height does not necessarily occur at the same condition for the maximum phase speed. The latter is also found to drop to asymptotic value $C = 2.56$ in high δ limit. The phase plot shows the linear dependence of phase speed to the low-to-intermediate range of wave height. Then, the phase H-C curves make similar-tie profile in the drag-inertia regime where phase speed is independent of Ka and the dimensionless wave height continuously drops down a gentle slope.

Institutional Repository - Library & Information Centre - University of Thessaly
09/06/2024 06:51:43 EEST - 18.219.33.223

3.3.2.2 Effect of Viscosity in the Drag-Gravity, and the Drag-Inertia Regime

From Fig. 3.7, at high δ value in the drag-inertia regime, phase speed is almost unaffected by Kapitza number, but the wave height increases roughly linearly with Ka which underlines the stabilising effect of viscous diffusion at low Ka.
On the contrary, in the drag-gravity regime, when the inertia is less important and surface tension assumes a prominent role, it is observed that the wave height (and also the phase speed) decreases with Kapitza number dictating a stabilizing effect of surface tension.

3.3.2.3 Flow Reversal

Flow reversal is studied for vertically falling film flow, as typically shown in Fig. 3.8 in the laboratory frame, where dashed lines (in the upper panel) demarcate the boundaries (zero velocity) of the downward and upward flow zones. It should be clearly specified that the upward flow is not a recirculating one because there is no close streamline. The mechanism for this phenomenon can be explained by observing a velocity field of a typical flow reversal zone between the hump and the first ripple (on the lower panel). On the downwind side of the main hump or ripples, the velocity vectors point downward and to the wall ($U > 0$, $V < 0$), but on the upwind side, they gradually turn away from the wall ($U > 0$, $V > 0$), with a wall-parallel direction at the peak of hump or ripples. In a high inertia flow, the U component on the upper part of the hump or ripples can exceed the phase speed C, which results in adverse gradient of pressure at capillary dimples. From Fig. 3.8, for example, the velocity ($U = 8.634650$) at the peak of the hump is larger than the phase speed ($3C = 7.694349$, the factor 3 is needed by rescaling with u_s). However, the velocity U is only a local value and varies along the free surface. In particular, the liquid flow increases speed in downwind side and decreases speed in upwind side of the hump or ripples. It slows down to zero speed until a flow reversal occurs. In the flow reversal zone which takes place around capillary dimples, the local U component varies either increasingly or decreasingly by magnitude but take a reverse direction. The physical mechanism inside the flow is similar to the one on the free surface but with lower magnitude in approaching to the solid wall. It is observed that in high inertia flow there is no recirculation in the main hump or in the crest of ripples but rather several flow reversal zones immediately in front of the high and fast hump and ripples.

At very low inertia with the wave height being very small, there is no flow reversal.

Institutional Repository - Library & Information Centre - University of Thessaly
09/06/2024 06:51:43 EEST - 18.219.33.223

However, its occurrence is not trivial because it is afterwards suppressed further in the higher inertia regime. A parametric map of flow reversal occurrence is shown in Fig. 3.9, where the flow reversal takes place in the zone between the two curves: one for the onset and the other for the suppression of flow reversal. An example for the aqueous glycerol solution with $Ka = 193$ shows the flow reversal emerges at $\delta = 1.5$, then survives in the higher range of inertia, and finally is suppressed beyond $\delta = 9.55$. It is observed that the appearance of flow reversal does not depend on liquids and emerges always at the same $\delta = 1.5$ but its survival and suppression delays to higher inertia for lower viscosity liquid (with larger Ka^*). For water $Ka^* = 3400$, the suppression of flow reversal does not happen in the window of inertia up to $\delta = 20$. The last important remark is that the onset of flow reversal at $\delta = 1.5$ is a demarcation between the drag-gravity regime with low wave height and small phase speed to the drag-inertia regime with much larger pertinent characteristics.

3.3.3 Comparison with Results of Low-Dimensional Models

In Fig. 3.10 the numerical predictions of the simplified model are compared with the DNS results. The comparison is not satisfactory. In particular, it is noted that the simplified model predicts the same dependence of phase speed, C, and wave height, H, on δ, irrespective of the change of liquid properties as expressed by Ka. Fig. 3.11 compares DNS to the predictions of the regularized model. Though the latter exhibits some variation in C and H with Ka, the agreement is still unsatisfactory. Finally, the predictions given by the complete second-order model of the four-equation set are presented in Fig. 3.12, and show a very satisfactory agreement with the DNS results for a large range of liquids, even though some differences may arise as expected for extremely high $Ka = 10000$.

3.3.4 Effect of Froude Number to Solitary Wave Properties

Now, extreme solitary wave is studied for film flow not only along vertical wall but also along inclined wall. According to Ruyer-Quil's definition (*Kalliadasis et al.*, 2012), the exchanging effect of inertia and gravity is expressed in a dimensionless number, Froude number Fr, which compares the speed of "kinematic wave" due to the advection, $3u_s$, and the speed of "gravity waves", $\sqrt{gh_s \cos\alpha}$ as follows,

$$\frac{1}{Fr^2} = \frac{\cot\alpha}{3\,Re} = \frac{\sqrt{gh_s\cos\alpha}}{(3\,u_s)^2} = \frac{\zeta}{\delta} \tag{3.24}$$

Institutional Repository - Library & Information Centre - University of Thessaly
09/06/2024 06:51:43 EEST - 18.219.33.223

It is reminded that this definition is different from the conventional one ($Fr^{-2} = 3/(Re\sin\alpha)$) for seeking a relationship to the critical threshold of long wave instability, $Re_c = \frac{5}{6}\cot\alpha$. That means a critical Froude number is $Fr_c^{-2} = 0.4$. If the value of Fr^{-2} varies in the unstable range from zero for vertical wall to the critical threshold, $Fr^{-2} = 0 \div 0.4$, the solitary wave properties can be shown for the aqueous glycerol solution with $Ka^* = Ka\,(\sin\alpha)^{1/3} = 193$ in Fig. 3.13 where $Ka^* = \frac{\sigma}{\rho\, g^{1/3}\nu^{4/3}}$ depending only on liquid properties. It is observed that for the same δ, the phase speed and wave height gets smaller when approaching the instability threshold or the critical Froude number. The DNS result also confirms the linear stability theory that there is no more wave for the $Fr_c^{-2} \geq 0.4$. At the other end of the range, these properties attain the largest values for flow along vertical wall, $Fr^{-2} = 0$. Again, it is observed that the results given by the complete second order model are in excellent agreement with the DNS results, see Fig. 3.13. In particular, it is observed that the maximum value of C and H, which is attained at large δ between 3 and 5, is the strongest for the vertical flow, but does not appear at small inclinations or low Fr^{-2}. Moreover the wave height of solitary wave is observed to be independent of liquid properties up to a distance from the critical threshold $Fr^{-2} = 0.4$, but to vary with Ka in the range of small Fr^{-2}, as shown in Fig. 3.14 for two liquids: aqueous glycerol, and pure water $Ka^* = 3400$ when all other physical parameters δ and Fr are kept the same. On the other hand, the C curves appear to be insensitive to liquid properties, and linearly proportional to the departure of Fr^{-2} from the criticality.

Noting the high δ limit of the same Fr curve, the phase speed appears to approach asymptotic value irrespective of flow rate whereas the wave height shows a slight dependence on the δ. The wave height gets maximum in the transition regime and drops slightly at higher δ due to scaling with the increasing substrate thickness.

3.4 Conclusions

Derivation of simplified models, based on long-wave expansions, for the description of liquid film flow has a long history marked by classical results such as the one-equation model of Benney and the two-equation model of Shkadov. A crucial test of such models is the correct prediction of the properties (shape, maximum height, phase velocity) of solitary waves as a function of the distance from the instability threshold. The latter is usually quantified in terms of the reduced Reynolds number, $\delta = (3\,Re)^{11/9} Ka^{-1/3}$, where the Reynolds number is defined in terms of the undisturbed film thickness and mean velocity, $Re = u_s h_s/\nu$, and the Kapitza number,

Institutional Repository - Library & Information Centre - University of Thessaly
09/06/2024 06:51:43 EEST - 18.219.33.223

$Ka = \sigma/(\rho\nu^{4/3}(g\,\sin\alpha)^{1/3}$, contains only physical properties and compares capillary and viscous diffusive effects. Considering a vertical wall and assuming negligible streamwise viscous diffusion effects, i.e. large Kapitza numbers, δ is the only independent parameter of the rescaled equations. It is recalled that, though most models predict similar behaviour close to the threshold (onset of drag-gravity regime), they exhibit large differences from each other at intermediate and large values of δ, i.e. when inertia becomes significant (transition region and drag-inertia regime). Thus, rigorous simulations emerge as the only means to resolve this issue. The present work computes accurately the properties of stationary, traveling wave by solving the Navier-Stokes equation by a finite-element technique, implemented with periodic boundary conditions and strong mesh refinement in the vicinity of the solitary wave. Solitary-like waves are derived by considering a long enough computational domain. However, it is shown that lengths of the order of 10^3 times the film thickness are necessary for the properties of the wave to converge asymptotically to the true solitary limit with accuracy less than 10^{-3}. Both the phase velocity and the wave height exhibit inflection points in the transition region, then maxima at intermediate values of δ, and finally a drop to a plateau at high enough δ. These are unique characteristics of the complete second-order model by Ruyer-Quil and Manneville, whereas all other models predict either a monotonic increase or a monotonic, asymptotic limit. In particular, simulations and the above second-order model agree quantitatively in the drag-gravity regime and the transition region to the drag-inertia regime, but only qualitatively in the drag-inertia regime. The behaviour deep in the drag-inertia regime is found to depend on Ka, which in the present simulations is varied in the range 200-10000. With increasing Ka, the maxima that occur at intermediate δ become steeper. However, whereas the high-δ limit of the phase velocity appears almost unaffected, that of the wave height increases roughly linearly with Ka, which underlines the stabilizing effect of viscous diffusion at low Kapitza numbers.

Institutional Repository - Library & Information Centre - University of Thessaly
09/06/2024 06:51:43 EEST - 18.219.33.223

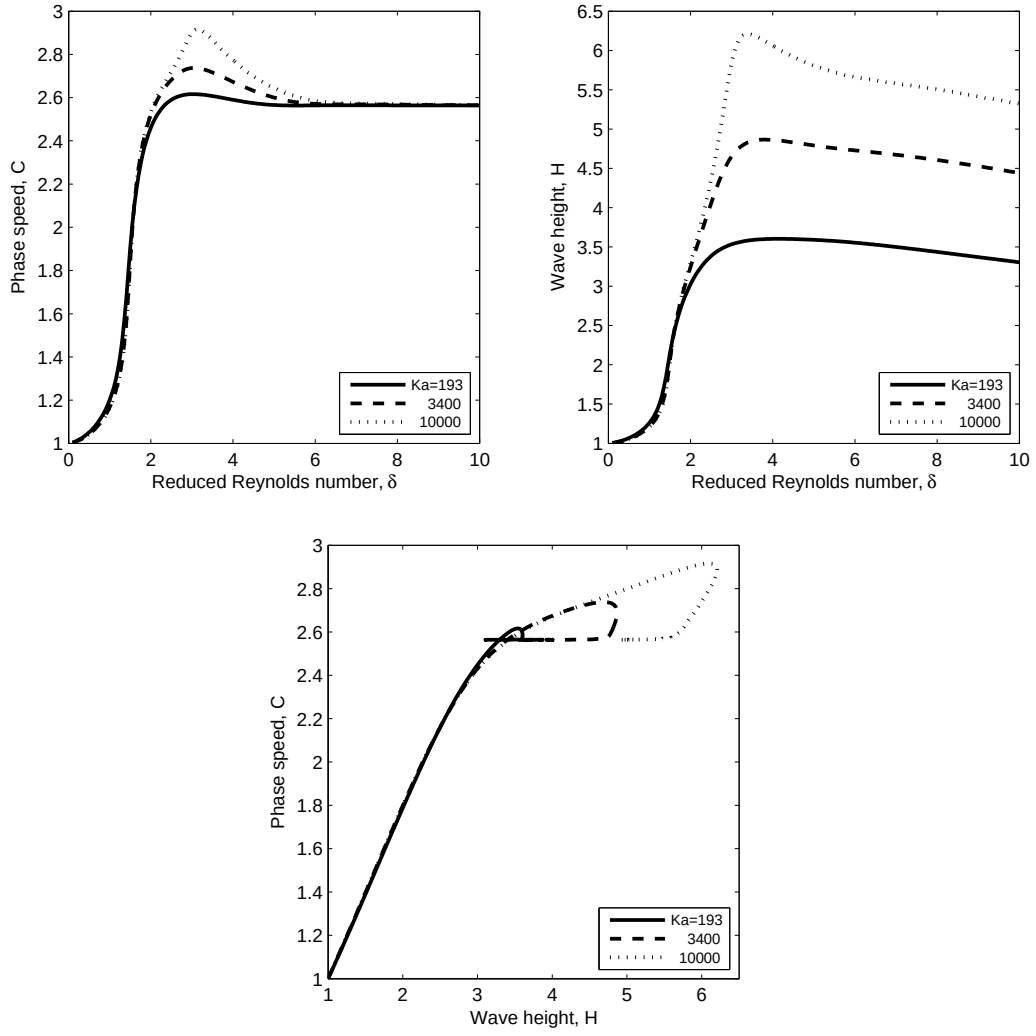

Figure 3.6: The extreme solitary wave's properties in terms of the δ for different liquid properties $Ka = 193$ (aqueous glycerol solution), $Ka = 3400$ (pure water), and $Ka = 10000$ (liquid nitrogen) flowing along a vertical wall $\alpha = 90°$. The third plot shows the phase space of C and H.

Institutional Repository - Library & Information Centre - University of Thessaly
09/06/2024 06:51:43 EEST - 18.219.33.223

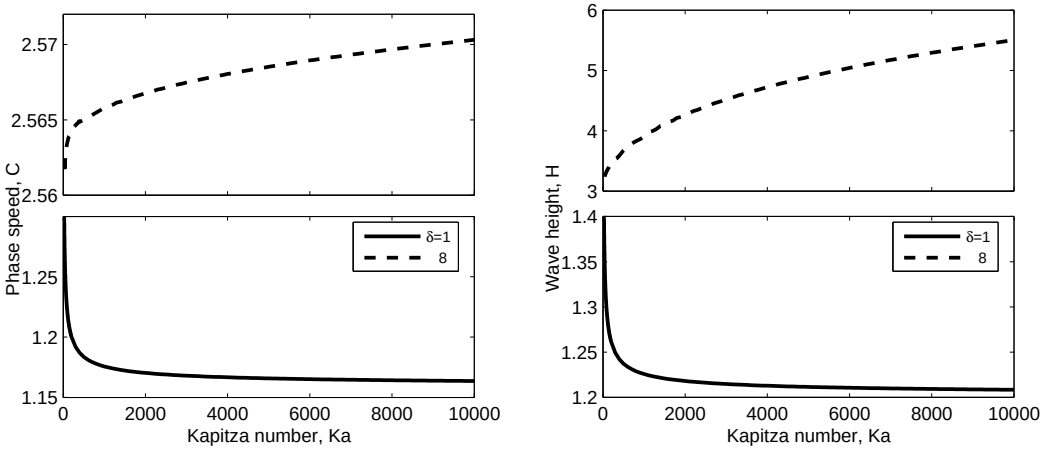

Figure 3.7: The extreme solitary wave's properties in terms of the Ka for flows in the drag-gravity regime, $\delta = 1$, and the drag-inertia regime, $\delta = 8$ along a vertical wall $\alpha = 90°$.

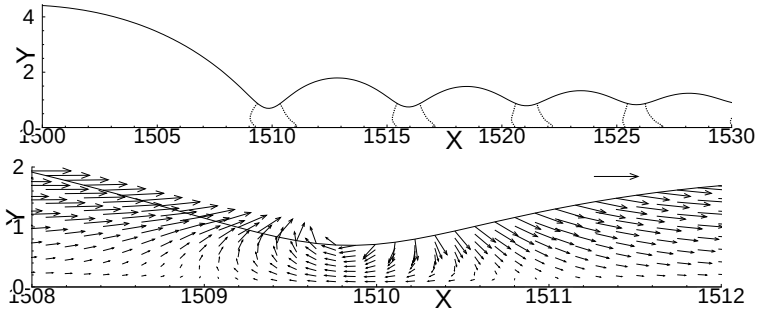

Figure 3.8: A close view of the reversal flow at high inertial regime, $\delta = 10$, for water with $Ka = 3400$ down a vertical wall. The upper panel plots the boundaries of flow reversal zone (in dashed lines), and the lower one depicts the velocity field (in vector) of one reversal zone in reference with the vector of the phase speed.

Institutional Repository - Library & Information Centre - University of Thessaly
09/06/2024 06:51:43 EEST - 18.219.33.223

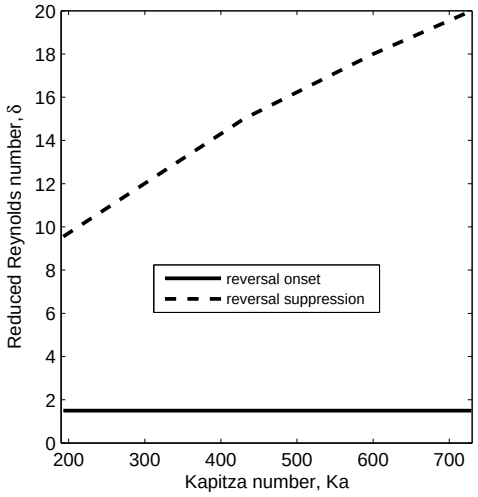

Figure 3.9: A parametric map of the flow reversal down a vertical wall.

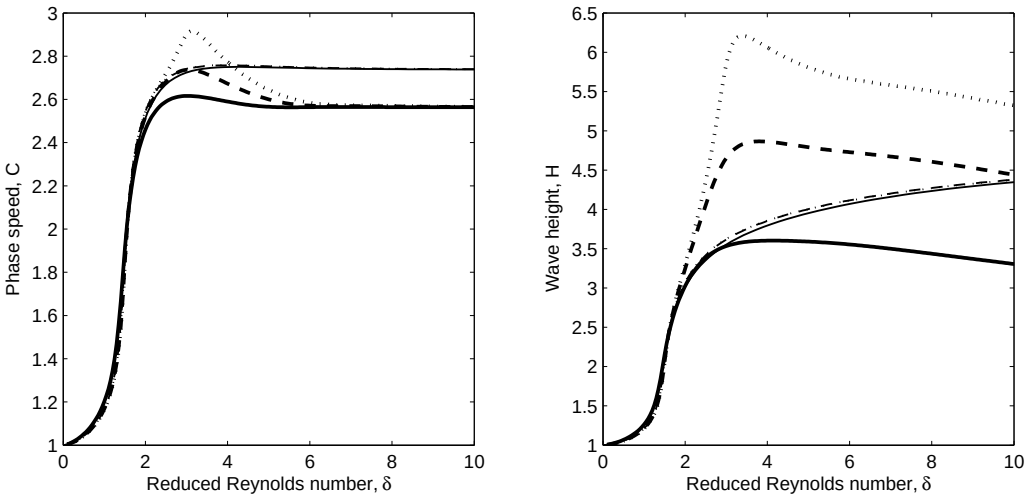

Figure 3.10: Comparison of numerical predictions by DNS with simplified model. The phase speed C and the amplitude H of the single hump solitary waves are shown as functions of the reduced Reynolds number δ where thick-solid, thick-dashed, thick-dotted lines correspond to the result from DNS and solid, dashed, dotted lines correspond to the result of the model for different Kapitza numbers, $Ka = 193$ (aqueous glycerol solution), $Ka = 3400$ (water), $Ka = 10000$ (liquid nitrogen) respectively.

Institutional Repository - Library & Information Centre - University of Thessaly
09/06/2024 06:51:43 EEST - 18.219.33.223

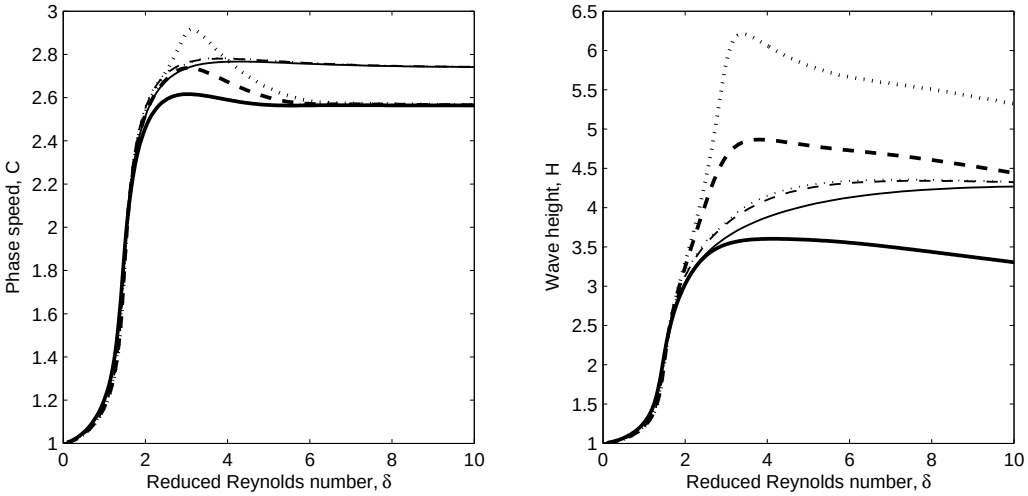

Figure 3.11: Comparison of numerical predictions by DNS with regularized model. The phase speed C and the amplitude H of the single hump solitary waves are shown as functions of the reduced Reynolds number δ where thick-solid, thick-dashed, thick-dotted lines correspond to the result from DNS and solid, dashed, dotted lines correspond to the result of the model for different Kapitza numbers, $Ka = 193$ (aqueous glycerol solution), $Ka = 3400$ (water), $Ka = 10000$ (liquid nitrogen) respectively.

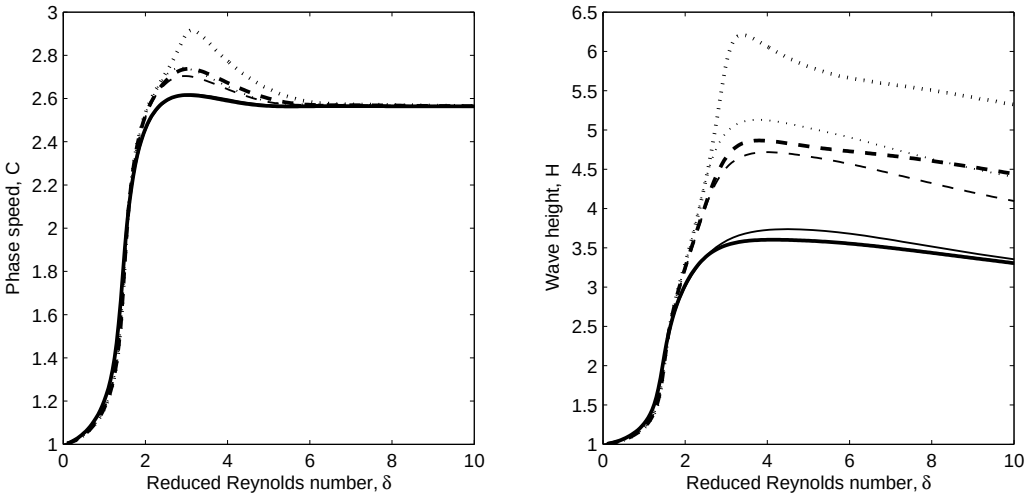

Figure 3.12: Comparison of numerical predictions by DNS with full second order model, where thick solid, thick dashed, thick dotted lines corresponds to the result from DNS and solid, dashed, dotted lines corresponds to the result of the four-equation model (Full second order model) for different Kapitza numbers $Ka = 193$ (aqueous glycerol solution), $Ka = 3400$ (water), $Ka = 10000$ (liquid nitrogen) respectively.

Institutional Repository - Library & Information Centre - University of Thessaly
09/06/2024 06:51:43 EEST - 18.219.33.223

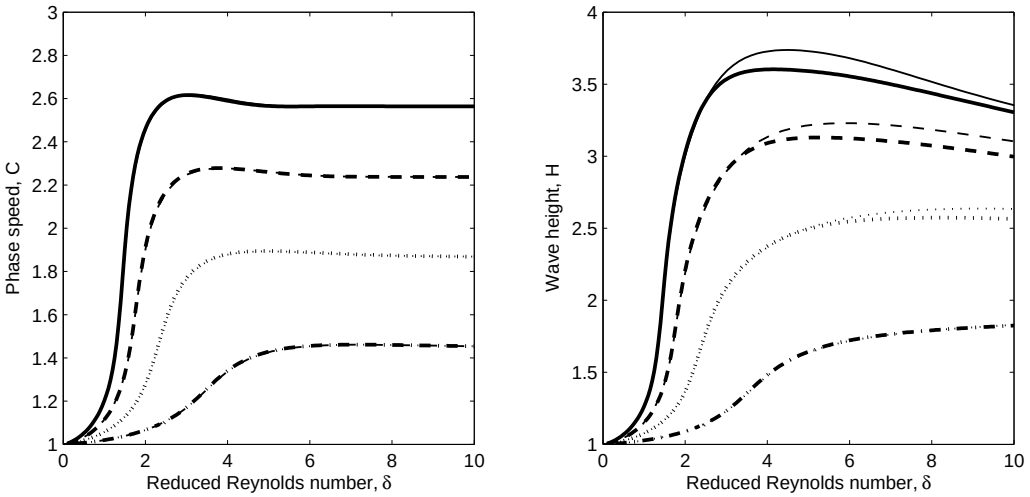

Figure 3.13: Comparison of numerical predictions by DNS with full second order model, where thick solid, thick dashed, thick dotted, thick dash-dotted lines corresponds to the result from DNS, and solid, dashed, dotted, dash-dotted lines corresponds to the result of the four-equation model (Full second order model) for different inverse square Froude numbers $Fr^{-2} = 0; 0.1; 0.2;$ and 0.3 respectively, and for the same liquid with $Ka^* = 193$.

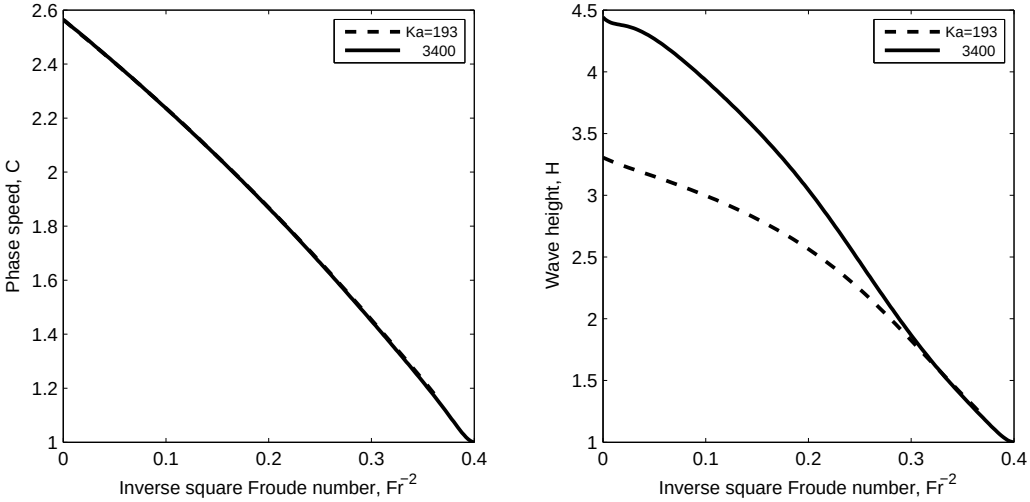

Figure 3.14: The extreme solitary wave's properties in terms of Fr^{-2} in the drag-inertia regime, $\delta = 10$ for different liquids.

Institutional Repository - Library & Information Centre - University of Thessaly
09/06/2024 06:51:43 EEST - 18.219.33.223

CHAPTER IV

Solitary Wave Interaction - Bound State Formation

The material presented in this chapter is a part of the collaborative work with the *Department of Chemical Engineering* in the *Imperial College in London*, UK. This chapter is an extended version of a manuscript in preparation entitled *Bound State Formation in Falling Liquid Film* by Phuc-Khanh Nguyen, Marc Pradas, Serafim Kalliadasis and Vasilis Bontozoglou. My specific contribution to this work is to compute the bound state system of two and three solitary waves on a sufficiently large domain length, based on DNS and offer a confirmation by the DNS results to the theoretical and numerical solutions given by the low-dimensional model (*Pradas et al.*, 2011a). To this aim, I specifically use a joining technique rather than the naive superposition of waves to construct a more appropriate initial guess, which is fed into the numerical code based on the stationary-in-co-moving frame Navier-Stokes equations to compute the separation distance of solitary waves in a two and three wave systems.

4.1 Introduction

Falling liquid films can be encountered in many multiphase industrial applications, specially because wave formation on free surfaces has a strong affect on e.g. heat and mass transfer or the quality of coating processes. Falling liquid films have also been extensively studied theoretically. A falling film is an open-flow, long-wave hydrodynamic instability, exhibiting a rich spatio-temporal dynamics and a wide spectrum of wave forms and interactions, starting from nearly harmonic waves upstream to complex spatio-temporal highly nonlinear wave patterns downstream. Reviews of the dynamics of a falling film are given, amongst others, in *Chang* (1994); *Chang and*

Institutional Repository - Library & Information Centre - University of Thessaly
09/06/2024 06:51:43 EEST - 18.219.33.223

Demekhin (2002); *Kalliadasis and Thiele* (2007); *Kalliadasis et al.* (2012).

For low-to-moderate Reynolds numbers (the Reynolds number is typically defined as the ratio of flow rate per unit span to kinematic viscosity), the flow evolves primarily in the streamwise direction as it is stable to spanwise modulations (*Demekhin et al.*, 2007). That has been observed in many experimental studies (*Argyriadi et al.*, 2004; *Liu and Gollub*, 1993; *Liu et al.*, 1993; *Vlachogiannis and Bontozoglou*, 2001) and theoretical works (*Chang et al.*, 1995, 2002). The film free surface appears to be randomly covered by localized coherent structures, each of which resembling infinite-domain solitary pulses. These pulses are a consequence of a secondary modulation instability of the primary wave field. They consist of a nonlinear hump preceded by damping ripples and can even appear at sufficiently small Reynolds numbers.

The organization of the free surface of falling liquid films into trains of coherent structures, has been numerically investigated by time-dependent finite-element simulations of the Navier-Stokes equations with free-surface boundary conditions (*Malamataris et al.*, 2002b), and analytically scrutinized in a recent coherent-structure theory based on weak interaction (*Pradas et al.*, 2011a), by appropriately extending previous works on coherent-structure interaction of model equation such as the generalized Kuramoto-Sivashinsky (gKS) equation (*Duprat et al.*, 2009; *Tseluiko et al.*, 2010a,b). As far as the falling film problem is concerned, the study by *Pradas et al.* (2011a) was based on a low-dimensional model for the flow containing terms up to second order in the long-wave expansion parameter (*Ruyer-Quil and Manneville*, 2000), and including the second-order viscous effects originating from the streamwise viscous diffusion and the tangential stress balance. These terms have been ignored in previous pulse interaction theories for film flows (*Chang and Demekhin*, 2002; *Chang et al.*, 1995). They prove to have a dispersive effect on the phase speed, the wave height, and the shape of the capillary ripples in front of a solitary hump.

The coherent-structure theory in *Pradas et al.* (2011a) showed that the interaction between solitary pulses may give rise to the formation of bound states consisting of two or more pulses separated by well-defined distances and travelling at the same velocity. The dynamics around such bound states is actually very rich since different behaviours, such as repulsion, attraction or self-sustained oscillations may emerge depending on the separation length between pulses (*Pradas et al.*, 2011b).

The present work aims to validate the results by *Pradas et al.* (2011a) study obtained from a low-dimensional model, through direct numerical simulation (DNS) of the full two-dimensional (2D) Navier-Stokes equations and associated boundary conditions. It confirms the results obtained in *Pradas et al.* (2011a) on bound-state

Institutional Repository - Library & Information Centre - University of Thessaly
09/06/2024 06:51:43 EEST - 18.219.33.223

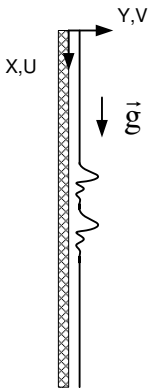

Figure 4.1: Bound-state formation in vertically falling liquid films.

formation on a two-pulse system, and provides further insight concerning the oscillatory interaction. Moreover, a detailed numerical study of bound states on a system composed of three pulses is presented, thus offering insight into the interpretation of the wideband spectrum of separation distances predicted by dynamic simulations of the low-dimensional model used in *Pradas et al.* (2011a) and involving many pulses.

Section 4.2 presents the Galerkin Finite Element Method and the technique to numerically construct initial guesses. The numerical results on stationary and non-stationary doublets, as well as stationary triplet interactions, are outlined in Sec. 4.3. Finally, it closes with conclusions in Sec. 4.4.

4.2 Computational Method

4.2.1 Governing Equations and Numerical Methods

This study consider 2D solitary pulses in liquid films flowing down along an infinite, vertical and planar wall (see Fig. 4.1). The liquid is incompressible and Newtonian, with density ρ, dynamic viscosity μ, and surface tension σ. The free surface is taken as shear-free, i.e. the dynamic effect of a superposed gas phase is negligible.

The problem is formulated as two-dimensional in a Cartesian coordinate system, with the x-axis pointing towards the mean flow direction and the y-axis across the film. A moving frame (t, x, y) with the velocity c of a solitary pulse is introduced to transform the laboratory frame (τ, ξ, η) coordinates as $t = \tau$, $x = \xi - c\,\tau$, and $y = \eta$,

Institutional Repository - Library & Information Centre - University of Thessaly
09/06/2024 06:51:43 EEST - 18.219.33.223

so that:

$$\frac{\partial}{\partial \tau} = \frac{\partial}{\partial t}\frac{\partial t}{\partial \tau} + \frac{\partial}{\partial x}\frac{\partial x}{\partial \tau} = \frac{\partial}{\partial t} - c\,\frac{\partial}{\partial x},$$
$$\frac{\partial}{\partial \xi} = \frac{\partial}{\partial x}\frac{\partial x}{\partial \xi} = \frac{\partial}{\partial x},$$
$$\frac{\partial}{\partial \eta} = \frac{\partial}{\partial y}\frac{\partial y}{\partial \eta} = \frac{\partial}{\partial y}.$$

Although velocity vector and pressure are determined each at moving coordinates (t, x, y), these flow field variables are still referred to the laboratory frame. The primitive flow input is the volumetric flow rate per unit span, q, and the location of the free surface in the moving frame is denoted as $y = h(x, t)$.

The Navier-Stokes equations governing the 2D flow are non-dimensionalized using as characteristic scales the film thickness and the mean velocity of the undisturbed substrate far away from the main hump transporting the flow rate q along a planar wall,

$$h_S = \left(\frac{3\mu q}{\rho g \sin\alpha}\right)^{1/3}, \qquad u_S = \frac{g h_S^2 \rho \sin\alpha}{3\mu}, \tag{4.1}$$

respectively. g is gravity and α is the wall inclination angle which for simplicity is set to $\alpha = 90°$. The resulting stationary differential equations are formulated in the moving frame as follows:

$$\mathbb{C} := \underline{\nabla} \cdot \underline{U} = 0, \tag{4.2}$$
$$\mathbb{M} := -C\frac{\partial \underline{U}}{\partial X} + \underline{U} \cdot \underline{\nabla}\,\underline{U} + \underline{\nabla} P - \frac{1}{Re}\underline{\nabla}^2 \underline{U} - \frac{3}{Re \sin\alpha}\underline{g} = \underline{0}, \tag{4.3}$$

where capital letters indicate dimensionless variables; $\underline{U} = [U, \quad V]^T$ is the velocity vector in the laboratory frame, P is the pressure, C is the dimensionless speed, and the scaled gravity vector is given as $\underline{g} = [\sin\alpha, \quad -\cos\alpha]^T = [1, \quad 0]^T$. The above equations are coupled to the kinematic equation for free surface evolution:

$$\mathbb{K} := -C\frac{\partial H}{\partial X} + U\frac{\partial H}{\partial X} - V = 0. \tag{4.4}$$

Non-stationary states are also studied in the moving frame by using the unsteady

Institutional Repository - Library & Information Centre - University of Thessaly
09/06/2024 06:51:43 EEST - 18.219.33.223

form of Eqs. (4.3) and (4.4):

$$\mathbb{M} := \frac{\partial \underline{U}}{\partial T} - C\frac{\partial \underline{U}}{\partial X} + \underline{U}\cdot\underline{\nabla}\,\underline{U} + \underline{\nabla}P - \frac{1}{Re}\underline{\nabla}^2\underline{U} - \frac{3}{Re\sin\alpha}\underline{g} = \underline{0}, \tag{4.5}$$

$$\mathbb{K} := \frac{\partial H}{\partial T} - C\frac{\partial H}{\partial X} + U\frac{\partial H}{\partial X} - V = 0, \tag{4.6}$$

where we have used $t_s = h_s/u_s$ as the characteristic time scale. Furthermore, we impose the no-slip and no-penetration boundary conditions on the wall,

$$U = V = 0, \tag{4.7}$$

and the dynamic boundary condition at the free surface,

$$\underline{n}\cdot\underline{\underline{T}} = \Delta P\,\underline{n} + 3^{1/3}\,Ka\,Re^{-5/3}\,K\,\underline{n}, \tag{4.8}$$

where $\underline{\underline{T}}$ is the stress tensor, $\underline{n}$ is the outward unit vector normal to the free surface and $K = \dfrac{H''}{(1+H'^2)^{3/2}}$ is the surface curvature. The dimensionless parameters Re and Ka appearing in Eqs. (4.5) and (4.8) correspond to the Reynolds and Kapitsa numbers, respectively, and will be defined and discussed in Sec. 4.2.3.

The case of a single travelling pulse serves as a basis for all subsequent investigations. Its computation involves six field variables: the two velocity components U and V, pressure P, free surface height H, pressure jump ΔP of a reference point in the liquid to the (uniform) gas pressure, and phase speed C. So far, we have four equations: one from (4.2), two from (4.3), and one from (4.4). The two additional equations needed to close the system are provided by (a) pinning the maximum of the hump at the middle of the flow domain (this eliminates a degeneracy without loss of generality),

$$H'(x = L/2) = 0, \tag{4.9}$$

and, (b) fixing the thickness of the undisturbed substrate far away from the main hump

$$H(x = 0) = 1. \tag{4.10}$$

By using the Galerkin finite element method on a structured mesh, the system of governing equations is integrally weighted with bi-linear $\Psi^i(\xi,\eta)$ (i = 1, 3), bi-quadratic $\Phi^i(\xi,\eta)$ (i = 1, 9), and quadratic basis functions $\Phi^i(\xi,\eta=1)$ (i = 1, 3), to produce,

Institutional Repository - Library & Information Centre - University of Thessaly
09/06/2024 06:51:43 EEST - 18.219.33.223

respectively, the residuals of the continuity, momentum, and kinematic equation:

$$\iint_V \mathbb{M}\,\Phi^i(\xi,\eta)\,dV = 0, \tag{4.11}$$

$$\iint_V \mathbb{C}\,\Psi^i(\xi,\eta)\,dV = 0, \tag{4.12}$$

$$\int_S \mathbb{K}\,\Phi^i(\xi,\eta=1)\,dS = 0. \tag{4.13}$$

The flow field variables consisting of velocities U and V, pressure P, and free surface height H are also interpolated from nodal unknowns using the above bases:

$$\underline{U} = \sum_{i=1,9} \underline{U}_i\,\Phi^i(\xi,\eta),$$
$$P = \sum_{i=1,4} P_i\,\Psi^i(\xi,\eta),$$
$$H = \sum_{i=1,3} H_i\,\Phi^i(\xi,\eta=1).$$

The elementwise integration of Eqs. (4.11), (4.12), and (4.13) is made by the nine, four, and three-point Gaussian quadratures, respectively. The time integration in unsteady computations is based on a Crank-Nicolson scheme. The resulting system of algebraic equations is solved by a Newton-Raphson iterative algorithm, coupled with a frontal technique.

4.2.2 Constructing Initial Guesses for Two-Pulse and Three-Pulse Structures

To obtain converged solutions to the different bound-state doublets, an appropriate initial condition needs to be devised. This is illustrated for the case of doublets. First, a single-pulse solution is obtained on a periodic domain of length L_D, which is sufficiently long to approach the infinite domain solitary-wave solution properties. Two such pulses are then assembled one next to the other along the streamwise direction, to set up a two-pulse structure. This initial structure, which in general is not a solution to the equations, is parametrized by the separation distance between the two humps. The structure is subsequently modified by removing a certain number of columns of elements in the film region joining the two pulses. Although the joining zone is no more continuous, this initial condition works very well: by fixing the lo-

Institutional Repository - Library & Information Centre - University of Thessaly
09/06/2024 06:51:43 EEST - 18.219.33.223

cation of one pulse [using Eq. (4.9)], and letting the other pulse relax to adjust to a new position, all the stable and unstable bound states predicted by weak interaction theory *Pradas et al.* (2011a) are recovered.

This technique is particularly efficient to successfully construct initial guesses of bound states with very closely-spaced pulses where use of a naive superposition of the two single-pulse solutions would lead to unacceptably high film thickness between the pulses. It is also important to remark that the success on using such a technique is based on the exponentially fast decay of both the front and back tails of the solitary pulses, as it is confirmed in Figs. 4.2 and 4.3, which is in turn also responsible for the very accurate computation of single-pulse properties based on a long but finite flow domain with periodic boundary conditions. Likewise, the construction of an initial guess for a bound-state triplet is a straightforward extension of the above technique by joining a numerically converged doublet with a single pulse or vice versa. The location of the single pulse is then fixed while the other two are left to relax to equilibrium positions. It should be noted however, that convergence to bound-states is numerically more tedious for triplets than for doublets.

4.2.3 Parameters and Characteristic Properties

The dimensionless parameters arising in the governing equation (4.3) are the Reynolds number, defined as the ratio of the mean flow rate per unit span to the kinematic viscosity,

$$Re = \frac{\rho\, q}{\mu} = \frac{\rho u_S h_S}{\mu}, \tag{4.14}$$

and the Kapitsa number appearing in Eq. (4.8) which depends only on the liquid properties as:

$$Ka = \left(\frac{l_c}{l_v}\right)^2, \tag{4.15}$$

involving the viscous length, $l_v = (\nu^2/(g\sin\alpha))^{1/3}$, and the capillary length, $l_c = (\sigma/(\rho g\sin\alpha))^{1/2}$.

Alternatively, three other dimensionless parameters, a reduced Reynolds number δ, a viscous dispersion number η, and a scaled inclination ζ are used often in falling film studies (*Kalliadasis et al.*, 2012; *Ruyer-Quil and Manneville*, 2000), and are

Institutional Repository - Library & Information Centre - University of Thessaly
09/06/2024 06:51:43 EEST - 18.219.33.223

related to the above conventional parameters as follows:

$$\delta = (3Re)^{11/9} Ka^{-1/3} = \frac{h_s^{11/3}}{l_\nu^3 \quad l_c^{2/3}}, \tag{4.16}$$

$$\eta = (3Re)^{4/9} Ka^{-2/3}, \tag{4.17}$$

$$\zeta = \cot\alpha (3Re)^{2/9} Ka^{-1/3}. \tag{4.18}$$

To make a comparison between the results given by the low-dimensional models and the Navier-Stokes computations for $\alpha = 90°$, only two parameters are varied independently, namely δ and Ka. Moreover, for solitary pulses in particular, the Shkadov scaling is appropriate, and it involves the compression factor $\kappa = \eta^{-1/2}$ followed by the transformation $X \to X\kappa^{-1}, T \to T\kappa^{-1}$. The principal characteristics of a solitary pulse are: (a) wave height, H, which is measured at the peak of solitary wave and scaled with the thickness of the undisturbed substrate as:

$$H = \frac{h}{h_S};$$

(b) phase speed, C, of the steady travelling pulses, scaled as:

$$C = \frac{c}{3\,u_S};$$

and (c) separation between pulses, L_S, nondimensionalized with flat substrate thickness $L_S = l/h_S$, and followed by a stretching via the Shkadov factor κ as:

$$L = \frac{l}{h_S \kappa}.$$

4.3 Numerical Results

4.3.1 Steady Doublets

Water is used as working liquid throughout the whole study with kinematic viscosity $\nu = 10^{-6}$ m^2/s, density $\rho = 1000$ kg/m^3, and surface tension $\sigma = 72.01$ mN/m, giving a Kapitza number of $Ka = 3364$. At first, the bound-state formation of two-pulses structure is studied by considering two cases of flow rates that correspond to the values $\delta = 0.98$ and $\delta = 1.82$. Other parameters such as Re, η, and κ are also calculated for reference. The computation of a single pulse yields the phase speed, C, and the wave height, H, shown in Table 4.1. These pulses are used to construct

Institutional Repository - Library & Information Centre - University of Thessaly
09/06/2024 06:51:43 EEST - 18.219.33.223

initial guesses.

δ	Re	η	κ	C	H
0.98	3	0.0118	9.1932	1.1595	1.2040
1.82	5	0.0148	8.2146	2.3999	2.9280

Table 4.1: Parameters and characteristics of the single solitary pulse in two study cases with water as working liquid.

The equilibrium separations between both pulses in bound-state doublets are shown in Table 4.2, and an example of a doublet profile for the low flow rate case, $\delta = 0.98$, is provided in Fig. 4.2. Note that there is a tolerance of L less than 0.05 due to mesh resolution with $\Delta X = 0.0296$ and $\Delta X = 0.0420$ respectively for two cases $\delta = 0.98$ and $\delta = 1.82$.

L_S	l [mm]	L	L [1]	Stability [1]
135.29	13.12	14.72	13.9	stable
156.79	15.21	17.06	17.3	unstable
190.54	18.48	20.73	20.7	stable
220.76	21.41	24.01	24.1	unstable
252.33	24.48	27.45	27.5	stable
283.37	27.49	30.82	30.9	unstable
314.67	30.52	34.23	34.3	stable
345.97	33.56	37.63	37.7	unstable
377.28	36.60	41.04	41.1	stable
408.31	39.61	44.41	44.5	unstable

Table 4.2: Bound-state separation lengths for $\delta = 0.98$. The dimensional separation distances l are obtained by rescaling with the substrate thickness $h_S = 0.097$ mm, and $L = L_S/\kappa$ is obtained after Shkadov scaling. [1] The results presented in the fourth and fifth columns correspond to the analytical findings in *Pradas et al.* (2011a).

As the flow rate is increased, the amplitude of the solitary wave becomes larger and the wave steeper, and both the frequency and amplitude of the front-running capillary ripples increase (see Fig. 4.3). As a result, the number of bound states observed at moderate distances also increases. Indeed, Table 4.3 shows a range of consecutive stationary separations with shorter increment as compared to the low flow rate case.

Remarkably, for both low and high flow rate cases (Table 4.2 and 4.3, respectively) there is an excellent agreement between the computed bound states at intermediate and large separation distances and the analytical predictions based on a

Institutional Repository - Library & Information Centre - University of Thessaly
09/06/2024 06:51:43 EEST - 18.219.33.223

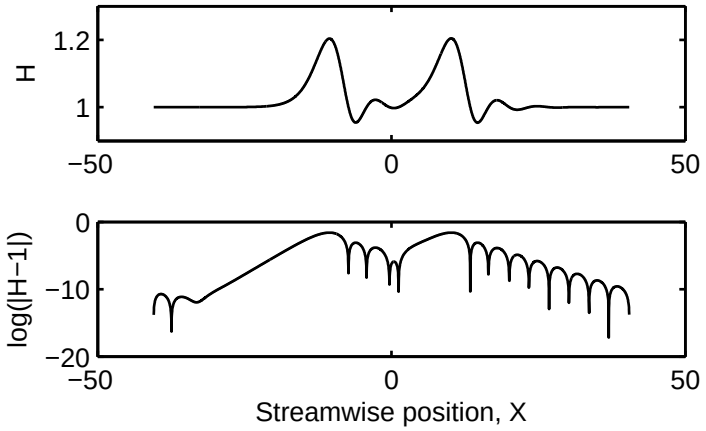

Figure 4.2: Free-surface profile and exponential representation of doublets for $\delta = 0.98$ for the bound-state separation $L = 20.73$.

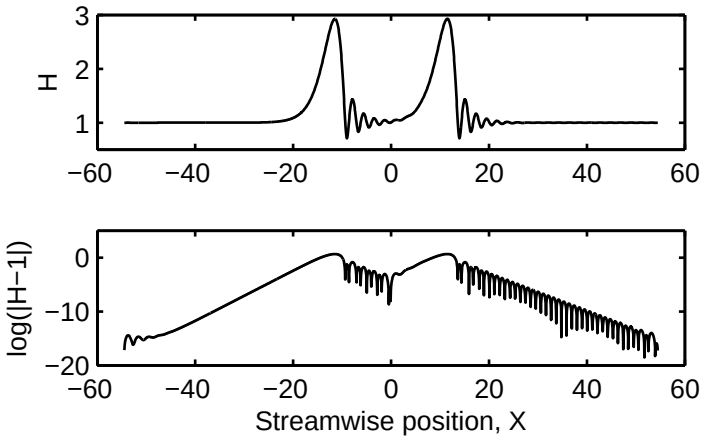

Figure 4.3: Free-surface profile and exponential representation of doublets for $\delta = 1.82$ for the bound-state separation $L = 22.97$.

low-dimensional model under the assumption of well-separated pulses (weak interaction) (*Pradas et al.*, 2011a). As expected, however, a deviation between theory and DNS appears for the shortest separation distances, where strong interactions between pulses start to play a prominent role.

4.3.2 Unsteady Doublets

Unsteady doublets are studied by setting $\delta = 1.82$ and $Ka = 3364$, and by choosing three different initial separation lengths (see Table 4.4).

Following *Pradas et al.* (2011a), the bound states given in Tables 4.2 and 4.3 have been classified alternatively as nominally stable and nominally unstable, according to

Institutional Repository - Library & Information Centre - University of Thessaly
09/06/2024 06:51:43 EEST - 18.219.33.223

L_s	l [mm]	L	L [1]	Stability [1]
156.23	17.97	19.02	18.81	stable
161.06	18.52	19.61	19.84	unstable
172.09	19.79	20.95	20.89	stable
178.99	20.58	21.79	21.93	unstable
188.65	21.69	22.97	22.98	stable
196.58	22.61	23.93	24.01	unstable
205.89	23.68	25.06	25.06	stable
213.83	24.59	26.03	26.09	unstable
222.79	25.62	27.12	27.14	stable
231.41	26.61	28.17	28.17	unstable
240.04	27.60	29.22	29.21	stable
248.66	28.60	30.27	30.25	unstable
257.28	29.59	31.32	31.29	stable
265.90	30.58	32.37	32.33	unstable
274.52	31.57	33.42	33.37	stable
283.15	32.56	34.47	34.41	unstable
291.77	33.55	35.52	35.45	stable
300.39	34.54	36.57	36.49	unstable
309.01	35.54	37.62	37.53	stable
317.63	36.53	38.67	38.56	unstable

Table 4.3: Bound-state separation lengths for $\delta = 1.82$. The dimensional separation distances l are obtained by rescaling with the substrate thickness $h_S = 0.115$ mm, and $L = L_S/\kappa$ is obtained after Shkadov scaling. [1] The results presented in the fourth and fifth columns correspond to the analytical findings in *Pradas et al.* (2011a).

the competition between weak attractive and repulsive forces when slightly displaced from equilibrium. Although it is expected that unstable states would not survive in time-dependent computations (pulses would shift towards stable positions), our computational results show that the actual behaviour is more complex and in fact intriguing. It is observed that stationary bound states emerge from time-dependent computations only when the initial pulse separation length is sufficiently large. An example is shown in Fig. 4.4, where initial distances of $L = 37.95$ and $L = 37.28$ approach monotonically the stable bound state $L = 37.62$. This weakly coupled pulse system may be viewed as an overdamped oscillator, where any deviation from equilibrium will be damped in time.

On the other hand, when both pulses are initially placed closely enough, the structure may exhibit an oscillatory behaviour around its steady separation with a pronounced and non-decaying amplitude. An example is provided in Fig. 4.5, where

Institutional Repository - Library & Information Centre - University of Thessaly
09/06/2024 06:51:43 EEST - 18.219.33.223

Case study	Attraction	Repulsion	Oscillation
Initial separation	37.95	37.28	25.06
Mean separation	37.62	37.62	27.12
Main frequency	0	0	0.082
Separation amplitude	0	0	0.75
Vertical amplitude of leading pulse	0	0	0.015
Vertical amplitude of trailing pulse	0	0	0.013

Table 4.4: Table of initial guesses and the dynamic properties of the doublet.

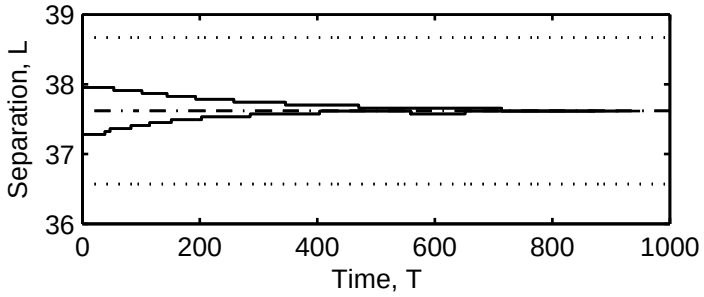

Figure 4.4: Monotonic attraction between two pulses when they are initially separated with $L = 37.95$, and monotonic repulsion when $L = 37.28$. The dashed dotted line shows the stable steady doublet separations, and the dotted lines unstable doublet positions.

the simulation is initially fed with a nominally stable separation solution, $L = 25.06$. The long-time behaviour consists of an oscillatory variation with the mean pulse separation around the value $L = 27.12$, which is similar to the steady separation $L = 27.12$ of a nominally stable bound state and it is in excellent agreement with the analytical prediction of $L = 27.14$ (*Pradas et al.*, 2011a).

It is important to note that such an oscillatory behaviour is clearly harmonic with a well-defined frequency F, in this case of $F = 0.0082$, demonstrating a periodic attracting-repelling alternation under the gravity forcing. This behaviour is coupled to the mass exchange between pulses: the growing pulse accelerates and the shrinking pulse decelerates, and their overshoot leads to an oscillation. The maximum and the minimum of the pulse-to-pulse separation is apparently confined between two neighbouring unstable separations.

The complex nature of pulse-to-pulse interactions is reflected in Table 4.5. First, it is noted that different initial separation lengths ranging between $L = 22$ and $L = 28$ lead to the same oscillatory behaviour with mean separation around $L = 27.20$ (see also Fig. 4.6 for the separation time evolution when initially is $L = 22.97$). This means that the stable bound states, which were found at distances below $L \sim 28$

Institutional Repository - Library & Information Centre - University of Thessaly
09/06/2024 06:51:43 EEST - 18.219.33.223

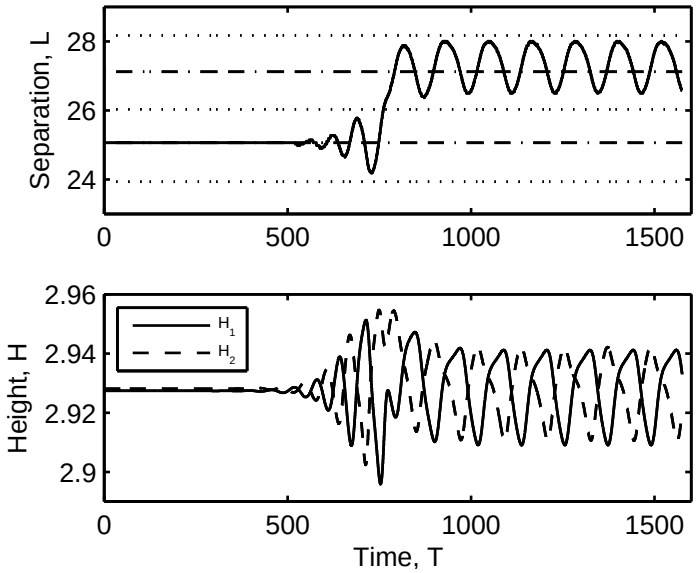

Figure 4.5: The dynamic oscillation of the separation length (top) and the pulse heights, H_1 and H_2, (bottom) of the unsteady doublet with mean separation $L = 27.12$. The initial solution is a nominally stable separation length with $L = 25.06$.

when computing steady solutions, turn out to be unstable when we consider time-dependent computations. Therefore, any initial separation length chosen in the range of $L \sim [22, 28]$ is attracted towards the oscillatory state.

On the other hand, it is also observed that both the amplitude and frequency of the final oscillatory state are independent of the initial condition, in particular, starting with either an initial separation of $L = 27.63$, which is slightly perturbed from the nominally stable state located around 27.12, or a strongly perturbed initial separation of $L = 22.97$, leads to a similar frequency and amplitude (cf. Table 4.5).

Initial L	Mean L	Main frequency	Amplitude
22.97	27.33	0.0085	0.75
25.06	27.12	0.0082	0.75
26.79	27.32	0.0085	0.74
27.63	27.33	0.0081	0.67

Table 4.5: Different initial conditions and dynamic properties of the doublet separation for $\delta = 1.82$.

Now, it can be expected that an evolutionary combination of a self-sustained oscillatory behaviour and a monotonically varying one may manifest for an initial separation distance in between. As an evidence, in Fig. 4.6, the initial separation length

Institutional Repository - Library & Information Centre - University of Thessaly
09/06/2024 06:51:43 EEST - 18.219.33.223

$L = 28.17$ exhibits a decaying oscillation behaviour with an exponentially decreasing amplitude. Therefore it makes a smooth transition from a range of self-sustained oscillatory behaviour into a monotonically varying one. This figure also shows once again the two large initial separations exhibit either monotonic attraction (36.44) or monotonic repulsion ($L = 36.69$) away from the unstable state toward stable states. This DNS information confirms the weak interaction theory about the bound-state instability in the range of large separation. Finally, it is also observed that for even smaller initial separation lengths ($L < 22$, see Fig. 4.6), there is an initial strong repulsive interaction that brings both pulses to rapidly repel each other. After a short attraction, the interactive process exhibits a quick monotonic growth, then a slight correction of separation until the pulses get locked into a stable bound state located at much larger distances. From a physical point of view, this behaviour may be qualitatively explained by considering that, at short separations, pulse interactions do not only occur via the tails (weak theory), but also between the main humps and capillary ripples, giving rise to a more complex interaction. So far, the oscillatory solutions found around the stable bound state $L = 27.12$ demarcate the transition from, on one hand a monotonic approach to stable equilibrium at much larger separations, and on the other hand, strong repulsive growth at much shorter separations. In this sense, such oscillatory states may be viewed as metastable states, that could tentatively be attributed to a narrow strange attractor of film flow dynamics.

4.3.3 Steady Triplets

The final question intended to address is the effect caused by the presence of a third pulse in the binary system studied in the previous sections. As starting point, and for the sake of simplicity, it is focused on the formation of stationary triplets. The numerical results for $\delta = 0.98$ and $Ka = 3364$ are given in Table 4.6 in terms of the separation length between the first and second pulses, L_{12}, and between the second and third, L_{23}. The equilibrium doublet separations are also provided for reference along the left column and the bottom row of the table.

The question of whether the existence of a third pulse modifies the previously computed equilibrium distance of doublet bound states is addressed more conveniently in Fig. 4.7. Grid lines mark pulse separation of nominally stable (dot-dashed) and nominally unstable (dotted) doublets bound states, and solid circles correspond to the separations L_{12} and L_{23} of the triplets. Points along the diagonal indicate that, if the leading and trailing pulses are placed symmetrically with respect to the middle one, the equilibrium separation distances are similar to those obtained in a binary system.

Institutional Repository - Library & Information Centre - University of Thessaly
09/06/2024 06:51:43 EEST - 18.219.33.223

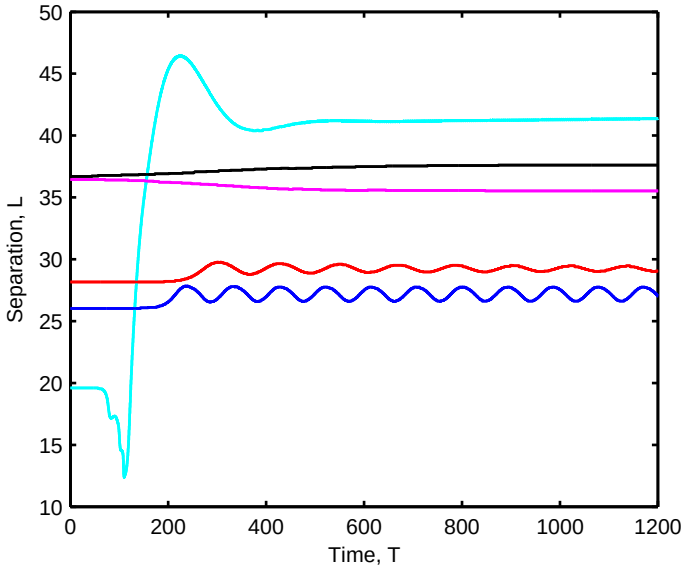

Figure 4.6: Time evolution of separation lengths for five different initial conditions: $L = 19.61$ (explosive repulsion), 26.03 (self-sustained oscillation), 28.17 (decaying oscillation), 36.44 (monotonic attraction) and $L = 36.69$ (monotonic repulsion).

However, when the leading and trailing pulses are placed asymmetrically (points off the diagonal), the pair of pulses with the shortest separation length equilibrates with the remaining pulse at separation lengths that may deviate considerably from the binary system, especially at short distances (see points located around $L_{23} = 15$ and $L_{12} > 20$). It is also important to note that these results depend on whether the pair with shortest distance is located in front or behind the remaining pulse. This is consistent with the numerical observations by *Pradas et al.* (2011a) using random initial conditions, the statistical analysis of which indicates that pulse separation may exhibit a broad distribution around specific mean distances.

4.4 Conclusion

It has been shown via DNS that the interaction between solitary pulses may give rise to the formation of bound states consisting of two or more pulses separated by well-defined distances and travelling at the same velocity. Two-pulse systems are studied first: stationary solutions of the governing equations are sought and the resulting equilibrium pulse separation lengths compare favourably to theoretical predictions at large-to-intermediate separations. The approach to these solutions from

Institutional Repository - Library & Information Centre - University of Thessaly
09/06/2024 06:51:43 EEST - 18.219.33.223

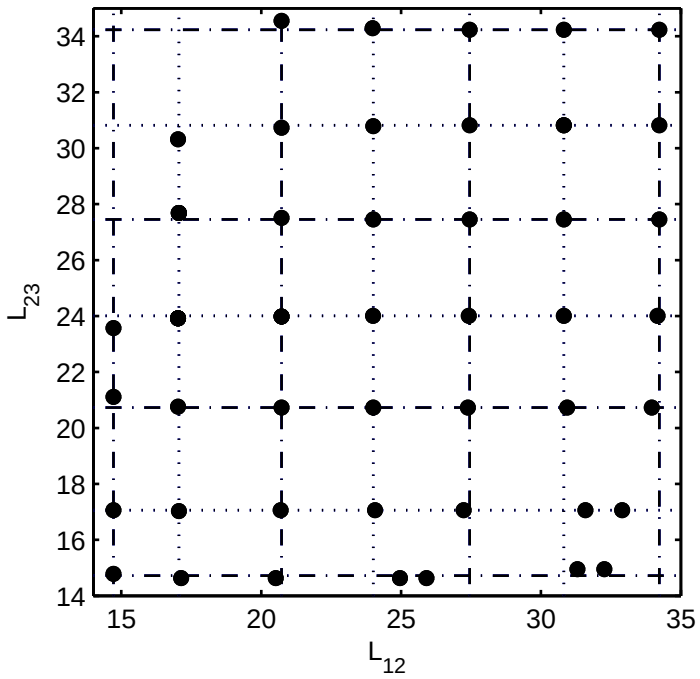

Figure 4.7: Map of the separation distances in a triplet for the same set of parameters in Table 4.6. The pairs (L_{12}, L_{23}) are depicted by the solid circle markers, whereas the dotted and dot-dashed lines show respectively the unstable and stable separations in a doublets, indicating deviation from the triplet's separations.

Institutional Repository - Library & Information Centre - University of Thessaly
09/06/2024 06:51:43 EEST - 18.219.33.223

34.23	-	-	20.73; 34.55	23.98; 34.29	27.45; 34.23	30.82; 34.23	34.23; 34.23
30.82	-	17.03; 30.32	20.73; 30.73	24.01; 30.79	27.45; 30.82	30.82; 30.82	34.23; 30.82
27.45	-	17.06; 27.68	20.73; 27.51	24.01; 27.45	27.45; 27.45	30.82; 27.45	34.23; 27.45
24.01	14.72; 23.57	17.03; 23.92	20.73; 23.98	23.98; 24.01	27.42; 24.01	30.82; 24.01	34.17; 24.01
20.73	14.72; 21.11	17.03; 20.76	20.73; 20.73	24.01; 20.73	27.39; 20.73	30.94; 20.73	33.96; 20.73
17.06	14.72; 17.06	17.06; 17.03	20.70; 17.06	24.07; 17.06	27.04; 17.06	31.59; 17.06	32.90; 17.06
14.72	14.72; 14.78	17.14; 14.63	20.52; 14.63	24.96; 14.63	25.91; 14.63	31.30; 14.95	32.27; 14.95
L_{12}; L_{23}	14.72	17.06	20.73	24.01	27.45	30.82	34.23

Table 4.6: Pairs of $(L_{12}; L_{23})$ of the triplet bound-state formation for $\delta = 0.98$, $Ka = 3364$. The left column and the bottom row depict doublet separations for reference.

appropriately perturbed initial conditions is shown by time-dependent computations to be monotonic and straightforward.

When two pulses are closely spaced, strong interactions between the two start to be relevant and the theoretical predictions based on weak interaction become less accurate. In addition, time-dependent simulations indicate that different initial conditions lead to an oscillatory dynamics with well-defined frequency and non-decaying amplitude. When the pulses are placed at very short separation lengths, strong repulsive interactions induce a rapid and monotonic growth of the pulse separation until a stable bound state is reached.

Stationary bound states consisting of three pulses were computed next, and pulse distances were compared to those obtained in the binary system. Deviations grow with the asymmetry in pulse location, indicating that multi-pulse systems are expected to exhibit broad distributions around the mean pulse separation distances.

Institutional Repository - Library & Information Centre - University of Thessaly
09/06/2024 06:51:43 EEST - 18.219.33.223

CHAPTER V

Steady Flows along Periodic Corrugations

The material presented in this chapter is a part of collaborative work under the guidance of my advisor, Prof. Bontozoglou. This chapter is an extended version of a paper entitled *Steady Solutions of Inertial Film Flows along Strongly Undulated Substrates* by P.-K. Nguyen and V. Bontozoglou, published in Physics of Fluids in 2011 (*Nguyen and Bontozoglou*, 2011). My specific contribution to this work is to compute extensively the properties of the film flows covering a large range of geometric and physical parameters. To this aim, I specifically create a parametric map to describe uniformly the physics behaviour of film flows under seemingly different conditions of flow rate, liquid properties or corrugated geometry.

5.1 Introduction

The effect of a wall with topography on gravity-driven, liquid film flow was first examined in the late '70s early '80s (*Tougou*, 1978; *Wang*, 1981), and has attracted since then a continuously growing interest. Applied motivation is related to the use of corrugated surfaces in industrial process equipment with the aim to increase heat and mass transfer rates (*deSantos et al.*, 1991; *Webb*, 1994; *Valluri et al.*, 2005), and also to the need of coating surfaces with topographical features (*Kalliadasis et al.*, 2000; *Tseluiko et al.*, 2008; *Luo et al.*, 2008). With respect to the latter, we note recent indications that a corrugated wall may extend the stable film flow to higher Re (*Wierschem et al.*, 2005; *Argyriadi et al.*, 2006; *Trifonov*, 2007), which have led to the suggestion (*Davalos-Orozco*, 2007) that a properly tailored wall could potentially increase the efficiency and through-put of coating processes.

More specifically, the modifications imposed on film flow by a periodic wall appear to be nontrivial in many respects, and thus their study attracts significant fundamental interest as well. The problem was first considered in the asymptotic limit of

Institutional Repository - Library & Information Centre - University of Thessaly
09/06/2024 06:51:43 EEST - 18.219.33.223

infinitesimal wall amplitude and creeping flow. The steady flow was shown (*Wang*, 1981) to replicate the period of the wall, with the deformation of the free surface varying in phase from that of the wall and decreasing monotonically in amplitude with the liquid film thickness.

Keeping the assumptions of infinitesimal wall amplitude and steady flow, but extending the analysis to finite Re, it was found (*Bontozoglou and Papapolymerou*, 1997) that the ratio of the free-surface to wall deformation (amplification) depends non-monotonically on Re, and under certain conditions exhibits the characteristics of a weak resonant interaction (linear resonance). More specifically, for wall wavelengths in the capillary to capillary-gravity range, a critical Re corresponding to maximum amplification was predicted, and the flow structure differed qualitatively between Re in the subcritical and the supercritical regime. Experimental evidence in favor of this prediction was provided later (*Vlachogiannis and Bontozoglou*, 2002; *Wierschem and Aksel*, 2004a), and the resonant interaction was explained recently (*Wierschem et al.*, 2008; *Demekhin et al.*, 2008) as a result of phase-locking between the undulated wall and capillary waves travelling against the flow.

A complementary aspect addressed in the literature is the effect of corrugations of finite amplitude, again in the limit of creeping flow (*Pozrikidis*, 1988; *Zhao and Cerro*, 1992; *Shetty and Cerro*, 1993; *Malamataris and Bontozoglou*, 1999). The formation of separation eddies at the wall troughs was predicted, and their role in the structure of the flow was investigated. More recently, a systematic delineation of the effect of liquid film thickness, inclination angle and wall waviness on the occurrence of these kinematic eddies over sinusoidal walls was accomplished (*Wierschem et al.*, 2003). In particular, the existence of a minimum dimensionless film thickness for the appearance of the eddy was observed, with the value of the minimum approaching zero as the waviness of the wall increases or the inclination angle decreases.

Unlike the above well-studied cases of infinitesimal wall amplitudes at arbitrary Re and of strongly corrugated walls at small Re, the information on the interaction of a steep wavy wall with a film at finite Re appears fragmentary, and a complete understanding of the flow is still lacking. The main new difficulty lies in the coupling between the deformation of the free surface and the separated flow structures close to the wall. Asymptotic analyses have predicted the first non-linear interactions (*Davalos-Orozco*, 2007; *Oron and Heining*, 2008; *Heining et al.*, 2009; *D'Alessio et al.*, 2009), but in most cases (with a notable exception (*Hacker and Uecker*, 2009)) the results are not valid beyond flow separation. Computational and experimental evidence (*Negny et al.*, 2001a,b) indicates that flow separation can occur not only at the

Institutional Repository - Library & Information Centre - University of Thessaly
09/06/2024 06:51:43 EEST - 18.219.33.223

trough, but also at the flattest part of a corrugated substrate. An interesting limit has been identified for very thick films (*Wierschem and Aksel*, 2004b; *Scholle et al.*, 2008), where surface deformation has a diminishing influence on the characteristics of the eddy.

Computational studies (*Trifonov*, 1998; *Bontozoglou*, 2000) have predicted that the separation eddy contracts, or even disappears, when the parametric conditions of linear resonance are approached. Very recently (*Wierschem et al.*, 2010), this prediction was systematically confirmed by a combination of experiments and simulations. Thus, the change in the nature of the flow when crossing linear resonance justifies differentiation between a subcritical and a supercritical regime.

The goal of this chapter is to provide systematic computational predictions in a wide parametric range of inertia and capillary forces, with particular emphasis to the case of steeply corrugated walls and relatively thin liquid films, i.e. when the free surface and the internal flow structures are strongly coupled. Only two-dimensional, steady solutions are considered, though it is noted that some results for three-dimensional, steady flows (two-dimensional topography) are already available in the literature (*Luo and Pozrikidis*, 2006; *Veremieiev et al.*, 2010).

Though the present study is limited to steady flows, we want to comment briefly on the related stability problem. It is known that, beyond a, small, critical value of the Reynolds number, film flow becomes convectively unstable to travelling disturbances. We argue, however, that the results of the present steady calculation, which extend to Re much higher than the critical, are important for a number of reasons, beyond their evident utility as a starting point for a stability analysis. In particular, film flows are convectively unstable and thus the steady solution always re-establishes between successive disturbances. In this sense, the computed profiles are the equivalent of steady, Nusselt flow that governs the substrate between waves in film flow along a flat wall. Further than that, there is experimental evidence (*Argyriadi et al.*, 2006) that the steady flow characteristics (spatially periodic deformation of the free surface with the wavelength of the wall and specific amplitude and phase) are always superposed on the travelling waves. An example similar to the data discussed in the above work is depicted in Fig. 5.1. More specifically, the profile of a travelling wave is shown for five time instants, separated from each other by 0.1s.

The outline of the chapter is the following: Sect. 5.2 describes the computational methodology, Sect. 5.3 describes the characteristics of the subcritical and supercritical separation, provides complete flow regime maps and documents the branch disconnection at high corrugation steepness. Finally, some concluding remarks are offered.

Institutional Repository - Library & Information Centre - University of Thessaly
09/06/2024 06:51:43 EEST - 18.219.33.223

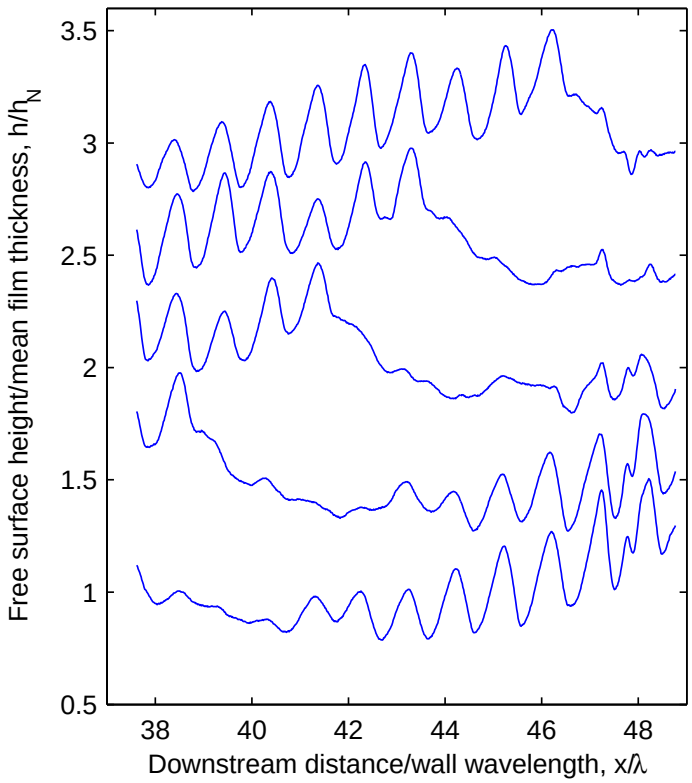

Figure 5.1: Streamwise free-surface profile at five consecutive instants for $\alpha = 5.4^o$ and $Re = 113$. The time interval between profile is $\Delta t = 0.1s$. Four upper profiles are consecutively shifted upward 0.5 for the sake of clarity.

Institutional Repository - Library & Information Centre - University of Thessaly
09/06/2024 06:51:43 EEST - 18.219.33.223

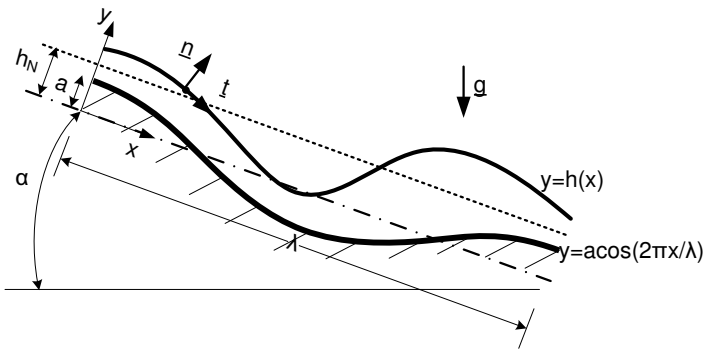

Figure 5.2: The configuration of film flow along sinusoidal corrugated wall

5.2 Governing Equations and Computational Methods

The film flow considered, occurs along a sinusoidally corrugated wall of wavelength λ and amplitude a, inclined at an angle α with the horizontal plane (Fig. 5.2). The problem is modelled as two-dimensional in a Cartesian coordinate system, with the x-axis pointing in the mean flow direction and the y-axis across the film. The respective dimensional velocity components are u and v. The liquid is incompressible and Newtonian, with density ρ, dynamic viscosity μ and surface tension σ. The primitive flow input is the volumetric flow rate q and the location of the free surface is described at steady state as $y = h(x)$.

The full Navier-Stokes equations governing the two-dimensional flow are non-dimensionalized using as characteristic scales the mean film thickness and the mean velocity

$$h_N = \Big(\frac{3\mu q}{\rho g \sin\alpha}\Big)^{1/3} \text{ and } u_N = \frac{g h_N^2 \rho \sin\alpha}{3\mu} \tag{5.1}$$

of the known steady Nusselt solution transporting the same flow rate along a flat wall. The resulting equations are formulated at steady state as follows, with capital letters indicating the respective dimensionless variables:

$$\begin{cases} \nabla \cdot \underline{U} = 0 \\ \underline{U} \cdot \nabla \underline{U} = -\nabla P + \frac{1}{Re}\nabla^2 \underline{U} + \frac{3}{Re}\underline{g} \end{cases} \tag{5.2}$$

where the velocity vector is $\underline{U} = [U, \quad V]^T$.

Moreover, we impose the no-slip and no-penetration boundary conditions at the wall,

$$U = V = 0, \tag{5.3a}$$

Institutional Repository - Library & Information Centre - University of Thessaly
09/06/2024 06:51:43 EEST - 18.219.33.223

with wall bottom profile

$$Y = \xi \cos(\delta X) \tag{5.3b}$$

and the kinematic and the dynamics boundary conditions at the free surface,

$$UH_X = V, \tag{5.4a}$$

$$\underline{n} \cdot \underline{\underline{T}} = \Big(\frac{3Bo^{-1}}{\delta^2 Re}\Big) K \underline{n}. \tag{5.4b}$$

In Eq. (5.4), $\underline{\underline{\mathrm{T}}}$ is the stress tensor, $\underline{\mathrm{n}}$ is the normal vector on the free surface and $K = \dfrac{H''}{(1+H'^2)^{3/2}}$ the surface curvature.

The dimensionless parameters in the governing equations (5.2) are the Reynolds number

$$Re = \frac{\rho u_N h_N}{\mu} \tag{5.5}$$

and the scaled gravity vector $\underline{g} = [1, \quad -\cot\alpha]^T$. Three other dimensionless parameters, appear in Eqs. (5.3) and (5.4), namely the dimensionless wall amplitude,

$$\xi = \frac{a}{h_N}, \tag{5.6}$$

the dimensionless film thickness (or, equivalently, the dimensionless wall wavelength),

$$\delta = \frac{2\pi h_N}{\lambda}, \tag{5.7}$$

and the inverse Bond number,

$$Bo^{-1} = \frac{4\pi^2 \sigma}{\rho g \lambda^2 \sin\alpha}. \tag{5.8}$$

The latter may also be considered as the squared ratio of the capillary length $l_c = \sqrt{\sigma/(\rho g \sin\alpha)}$ over the wall wavelength. An additional important parameter is the steepness of the wall corrugations,

$$\zeta = \frac{2\pi a}{\lambda} = \xi\delta. \tag{5.9}$$

The system of governing equations and boundary conditions is discretised using the Galerkin finite element method on a structured meshing. The velocities U and V are interpolated by bi-quadratic basis functions, the pressure P by bi-linear basis functions and the surface height H by quadratic basis functions. The discretised

Institutional Repository - Library & Information Centre - University of Thessaly
09/06/2024 06:51:43 EEST - 18.219.33.223

system of algebraic equations is solved by the Newton-Raphson iterative scheme, using a frontal technique.

The steady flows sketched in Fig. 5.3 resulting from the solution of the above system are typically characterized by: (a) The relative amplitude of the free surface

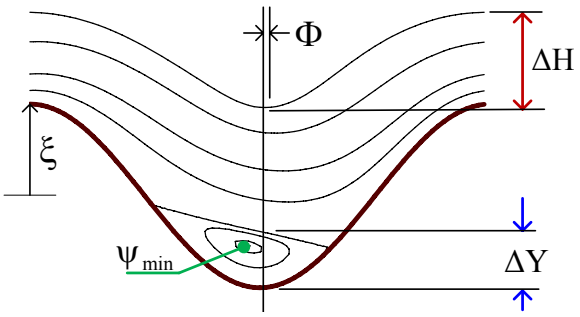

Figure 5.3: Characterization of steady solution of liquid film flow along a periodic wall.

deformation (amplification), β, which is a ratio of the peak-to-peak amplitude of the free surface to the wall amplitude,

$$\beta = \frac{H_{max} - H_{min}}{2\xi} = \frac{\Delta H}{2\xi} \tag{5.10}$$

(b) the superficial phase shift, Φ, which is measured in terms of the distance in the x-direction between the locations of minimum height on free surface and on the wall (the latter at $x = \lambda/2$)

$$\Phi = 360^o \left(\frac{x_{H_{min}}}{\lambda} - \frac{1}{2} \right) \tag{5.11}$$

and (c) the intensity, E_I, and size, E_S, of the separation eddy, in case such an eddy exists. The eddy intensity

$$E_I = \frac{|\Psi_{min}|}{q} \tag{5.12}$$

is defined in terms of the absolute value of the stream function minimum, Ψ_{min}, which occurs at the core of the eddy. The eddy size

$$E_S = \frac{(Y_{Separatrix} - Y_{Wall})_{x=\lambda/2}}{\xi} = \frac{\Delta Y}{\xi} \tag{5.13}$$

is defined as the distance in the y-direction from the bottom of the trough to the intersection with the separatrix. For the sake of clarity, flow structure plots (depicting equally spaced streamline contours) are sometimes drawn in x-y coordinates scaled with the wall wavelength.

Institutional Repository - Library & Information Centre - University of Thessaly
09/06/2024 06:51:43 EEST - 18.219.33.223

5.3 Results

5.3.1 Background Information from the Linear Limit

We use representative results from the well-studied (*Wierschem et al.*, 2008) linear limit ($\zeta \equiv 2\pi a/\lambda \ll 1$ and $\xi \equiv a/h_N \ll 1$), in order to introduce the role of the dimensionless numbers of the problem. More specifically, Fig. 5.4a shows the ratio of

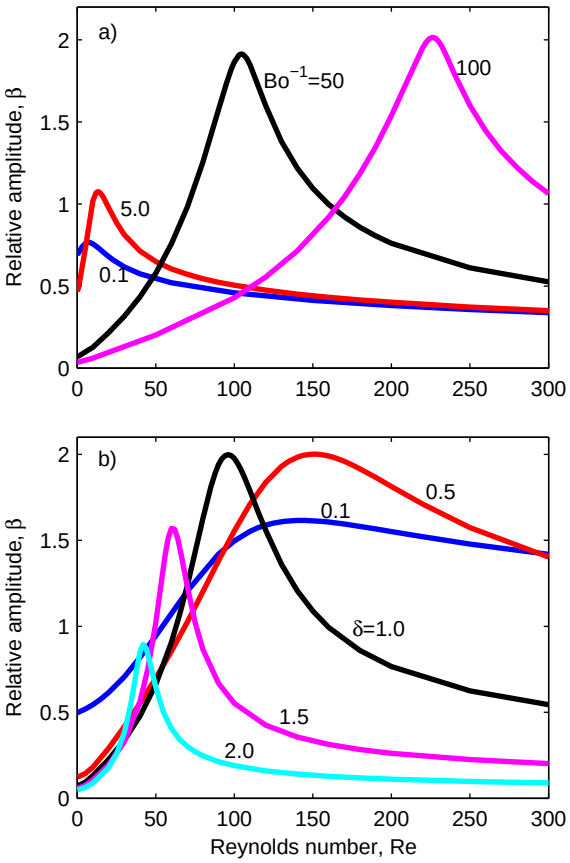

Figure 5.4: The ratio of the free surface amplitude to the wall amplitude as a function of Re for (a) various Bo^{-1}=0.1; 5; 50; and 100 at α=45°, ζ=0.1, δ=1, and (b) for various δ=0.1; 0.5; 1.0; 1.5; and 2.0 at α=45°, ζ =0.015, Bo^{-1}=50.

free surface to wall amplitude (amplification) as a function of Re for various values of the inverse Bond number, Bo^{-1}, and in Fig. 5.4b for various values of the dimensionless film thickness, δ. From Fig. 5.4a we observe that capillary forces have a dual, and superficially contradictory, effect. At zero Re, increasing Bo^{-1} results in smaller amplification, i.e. a less deformed free surface. This is intuitively expected, given that surface tension resists surface deformation. However, strong capillary forces also intensify the wall-free surface resonance. As a result, the peak in amplification grows

Institutional Repository - Library & Information Centre - University of Thessaly
09/06/2024 06:51:43 EEST - 18.219.33.223

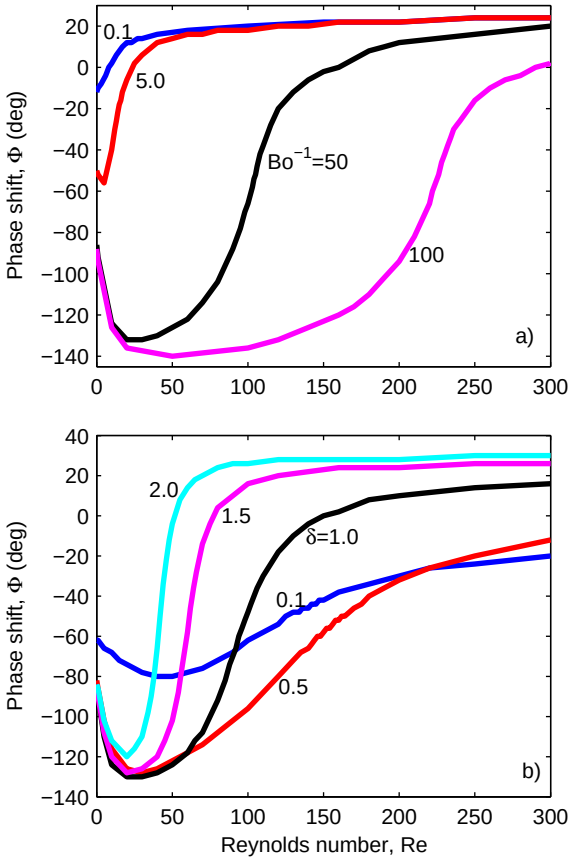

Figure 5.5: The phase shift of the free surface to the wall corrugation as a function of Re for (a) various Bo^{-1} at α=45°, ζ=0.1, δ=1, and (b) for various δ at α=45°, ζ=0.015, Bo^{-1}=50.

Institutional Repository - Library & Information Centre - University of Thessaly
09/06/2024 06:51:43 EEST - 18.219.33.223

with increasing Bo^{-1}, and simultaneously moves to higher Re_{res}. Therefore, strong capillary forces resist free surface deformation at small Re, but trigger extensive deformation at high enough Re.

From Fig. 5.4b it is observed that free surface amplification is maximum at $\delta \sim O(1)$. For lower δ values, the surface deformation remains significant (approaching the value one as $\delta \to 0$) but loses in sharpness, whereas for higher δ values the resonance remains sharp but decreases in size. This is the typical behaviour when capillary forces are strong ($Bo^{-1} \sim O(10^1 - 10^2)$). In the regime of weak or negligible capillary forces ($Bo^{-1} \leq O(10^0)$), the free surface deformation only decreases monotonically with increasing film thickness.

The phase difference between the undulations of the free surface and the wall is depicted in Fig. 5.5a and b for parametric conditions corresponding respectively to Fig. 5.4a and b. At high Bo^{-1} (50 and 100), two limits are identified: at low Re the phase of the free surface precedes that of the wall, whereas at high Re it lags behind. The rapid variation in phase lag occurs around Re_{res}, and we may thus identify a subcritical and a supercritical flow regime. For low Bo^{-1} (0.1 and 5), capillary effects are small and the supercritical flow regime extends in the whole range of Re.

Based on the insight gained from the linear limit, we summarize the physical significance of the dimensionless variables of the problem as follows: The Reynolds number, Re, defines the subcritical and the supercritical regimes, separated by the value, Re_{res}, where the free surface exhibits maximum amplification in the linear limit. The classification into subcritical and supercritical flow is very convenient in the analysis of the non-linear problem as well, and will be adhered to in the rest of the paper. In particular, it unifies the observed behaviour under apparently different values of the pertinent parameters.

The inverse Bond number, Bo^{-1}, is mainly affected by the wavelength of the corrugations, and defines the capillary and the gravity regimes. The wall-free surface resonance is strong in the former but becomes gradually negligible in the latter. The dimensionless film thickness, δ, has a damping effect, and thus governs the extent to which the flow disturbance due to the wall is conveyed to the free surface. The mean inclination angle, α, determines the component of gravity normal to the wall, and thus the stabilizing effect of the gravity force. With the exception of the last subsection, where predictions are compared to independent data, all the present simulations are performed at an intermediate inclination $\alpha = 45^o$.

Finally, the wall steepness, ζ, whose effect constitutes the main theme of the present work, determines the extent of deviation from linear behaviour. We will see

Institutional Repository - Library & Information Centre - University of Thessaly
09/06/2024 06:51:43 EEST - 18.219.33.223

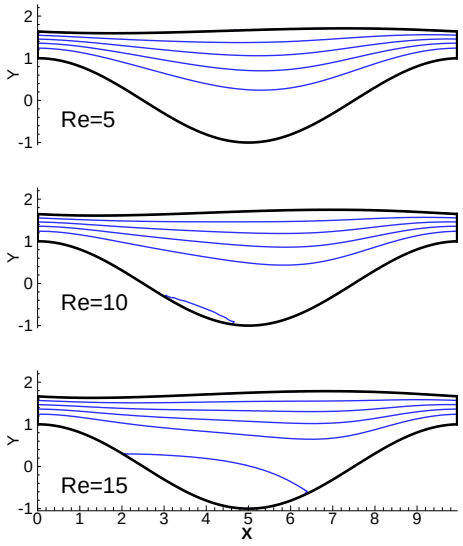

Figure 5.6: The contour plots of streamlines for ξ=1, δ=$2\pi/10$, α=45^o, Bo^{-1}=50 and increasing Re.

that, as the wall becomes steeper, the flow separates both in the subcritical and in the supercritical regime. If δ is not very large, the internal flow generated from the separation eddies interacts in a non-trivial way with the free surface, and variables δ, Re and Bo^{-1} combine to determine the intensity of free surface deformation. The above form a complex parametric matrix for the problem, whose effect will be attempted to be delineated by appropriate flow regime maps. For very steep wall corrugations, the steady computations will be shown to reach singular limits. The relation of these computational limitations to actual physical singularities, such as hydraulic jumps (shocks), and to the transition from steady to oscillatory behaviours will be questioned by comparisons with independent data.

5.3.2 Subcritical Flow Separation

Inertially-induced separation may take place at relatively small $Re \sim O(10^0 - 10^1)$ if the change in flow cross-section is steep enough to create a significant adverse pressure gradient. The most straight-forward case is when the free surface is practically flat, a condition that is satisfied when capillary forces are strong enough, and the deformation triggered by the wall-free surface resonance is postponed to much higher Re. Then, separation takes place at the inflow to the corrugation trough, as in the classical problem of a diverging channel. The situation is of course reversed at the outflow from the trough, and the flow re-attaches. Examples of this process are shown in the streamline plots of Fig. 5.6, which correspond

Institutional Repository - Library & Information Centre - University of Thessaly
09/06/2024 06:51:43 EEST - 18.219.33.223

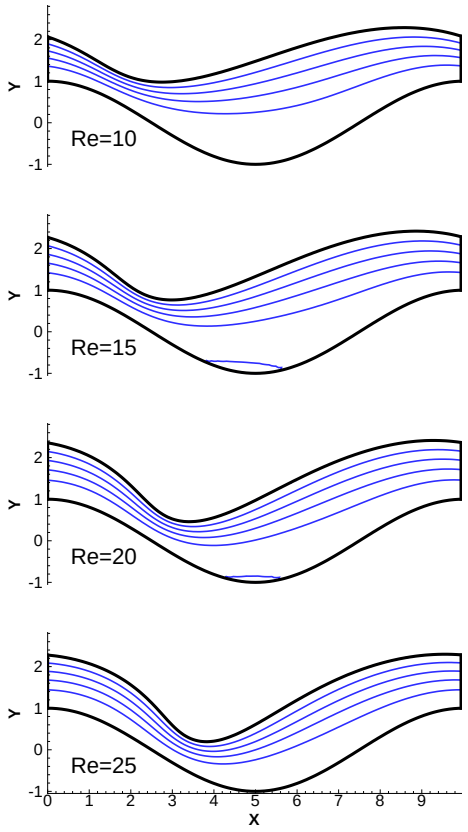

Figure 5.7: The contour plots of streamlines for ξ=1, δ=$2\pi/10$, α=45^o, Bo^{-1}=5 and increasing Re.

to $\xi = 1$, $\delta = 2\pi/10$, $\alpha = 45^o$, $Bo^{-1} = 50$ and increasing Re. The separatrix of the inertial eddy is at an angle to the mean wall inclination, as has been observed in experiments (*Wierschem et al.*, 2005). With increasing Re, the separation eddy grows in size and covers most of the corrugation trough.

It is important to note that the above parametric evolution with Re is totally insensitive to further increase in Bo^{-1}, i.e. separation occurs at the exact same value of Re. This observation confirms that under the present conditions capillary forces have no other dynamic role apart from keeping the interface flat. On the contrary, when moving to low Bo^{-1}, the resonant interaction occurs at low enough Re to have a dynamic effect. Though it is now very weak, it deforms the free surface so that the flow is assisted to remain attached. An example is provided in Fig. 5.7, which corresponds to the same conditions as in Fig. 5.6, except for $Bo^{-1} = 5$. It is observed that, not only the onset of separation is delayed, but its subsequent evolution is also suppressed.

The effect on flow separation of the wall steepness, ζ, is presented in Fig. 5.8,

Institutional Repository - Library & Information Centre - University of Thessaly
09/06/2024 06:51:43 EEST - 18.219.33.223

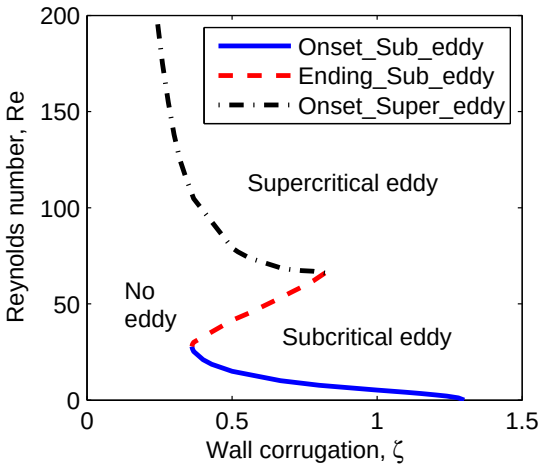

Figure 5.8: The parametric regime, in Reynolds number and wall steepness space, where eddies appear for δ=1, Bo^{-1}=15 and α=45^o.

which corresponds to $\delta = 1$ and $Bo^{-1} = 15$. Separation occurs on the right side of the curves, which represent events of onset and ending of steady eddies triggered by parametric variation of Re. The onset of a subcritical eddy is denoted by the continuous line and its disappearance by the dashed line. Finally, the dashed-dotted line indicates the onset of supercritical separation, to be discussed in the next section.

Concentrating on the subcritical curves, we note that, with increasing ζ the onset of separation moves to lower Re, and eventually occurs at $Re = 0$ for $\zeta \geq 1.3$. Separation in the limit $Re \to 0$ corresponds to a geometrically induced eddy, which has been systematically documented by *Wierschem et al.* (2003). Also, referring to a recent discussion by *Scholle et al.* (2008), it is observed that there exists a synergy between geometric and inertial effects. When the wall is too steep for the film of given thickness to be accommodated through its trough, separation occurs at $Re = 0$. When it is barely smooth enough, separation takes place at a small but finite Re. With decreasing steepness, subcritical separation occurs at progressively higher Re, and does not take place at all below a minimum value that in the example of Fig. 5.8 is $\zeta_{min} \approx 0.36$.

The effect of dimensionless film thickness, δ is presented in a series of streamline plots in Fig. 5.9, which corresponds to $\zeta = 2\pi/5$, $Bo^{-1} = 5$, $\alpha = 45$ and $Re = 10$. Strong inertial separation occurs at small film thickness, but diminishes and almost disappears as δ grows. However, as the mean film thickness exceeds the wall amplitude, a separated region re-establishes, and its size appears independent of further increase in δ. The eddies may be characterized quantitatively by their size,

Institutional Repository - Library & Information Centre - University of Thessaly
09/06/2024 06:51:43 EEST - 18.219.33.223

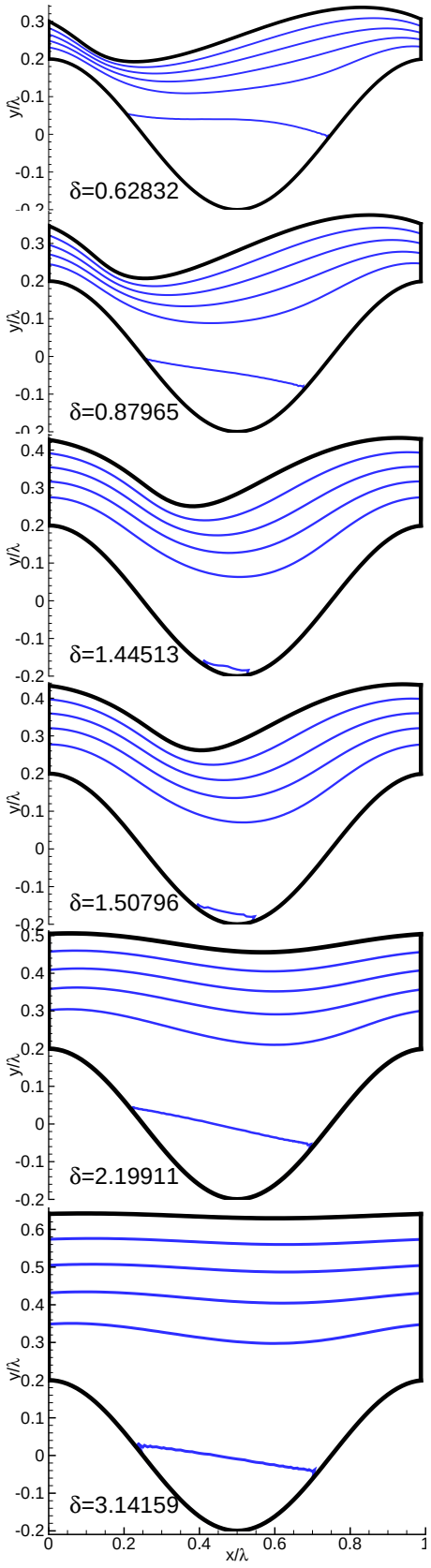

Figure 5.9: The flow structure in subcritical regime with increasing dimensionless film thickness for Re=10, ζ=$2\pi/5$, α=45^o, Bo^{-1}=5.

Institutional Repository - Library & Information Centre - University of Thessaly
09/06/2024 06:51:43 EEST - 18.219.33.223

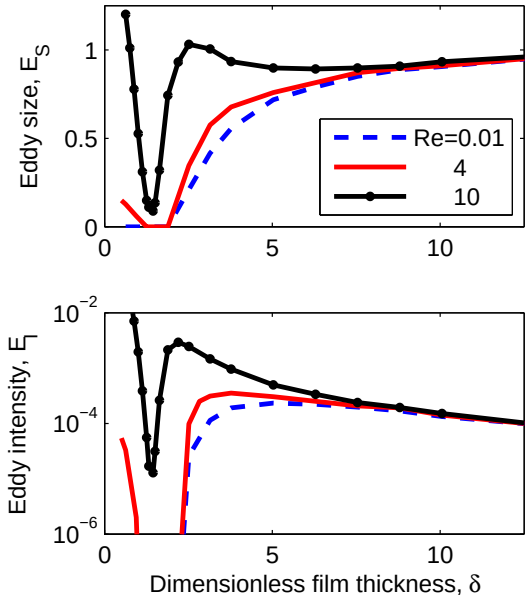

Figure 5.10: The effect of film thickness on the size and intensity of the subcritical eddy for ζ=$2\pi/5$, Bo^{-1}=5 and α=45^o.

E_S and intensity, E_I. Fig. 5.10 shows the relevant results for the previous conditions, but now for three values of Re. It is observed that, in the limit of very thick films, the characteristics of separation become independent of Re, and approach those of creeping flow. This behaviour was explained by *Scholle et al.* (2008), who showed that the flow close to the wall is governed by a local Re, based on the corrugation height, which may be much lower than the global Re calculated from the film thickness. On the contrary, for thin enough films a strong inertial separation takes place. It is interesting to observe that the extent of inertial separation varies inversely with the film thickness, whereas geometric separation is proportional to it. For example, at $Re = 4$ and with increasing film thickness from very small values, one observes from Fig. 5.10 a dominant inertial eddy gradually shrinking in size, then a film with no separation, then a film with geometrically induced separation.

According to the above, the value of the dimensionless film thickness (which may be envisioned to vary by changing the kinematic viscosity while retaining the same Re) results in a significant difference of the flow between the two extremes of very thin and very thick films. Insight implies that a thin, low viscosity film has a better ability to bridge the distance between successive corrugations, thus resulting in a large separation eddy. This is a typically subcritical characteristic. At the other end, very thick films are characterized by a local interaction between the wall and the

Institutional Repository - Library & Information Centre - University of Thessaly
09/06/2024 06:51:43 EEST - 18.219.33.223

flow, which results in a geometrically induced separation eddy, though the flow may be formally supercritical for high enough δ.

5.3.3 Supercritical Flow Separation

In the limit of supercritical Re, well beyond the resonance regime, the deformation of the free surface diminishes once again. However, this behaviour is not related to capillary forces, whose role is now insignificant, but to the inertia of the liquid, which is sufficient to bridge the gap between successive crests of the wall corrugation. Typical flow structures are provided by the streamline plots in Fig. 5.11, which correspond to $Re = 300,\ \zeta = 2\pi/10,\ Bo^{-1} = 5,\ \alpha = 45^o$ and increasing film thickness. It is observed that for $\delta \geq 1$ the open streamlines are practically straight, and thus the flow resembles an undisturbed film flowing above the crests and the separation eddy.

Returning to Fig. 5.8, we confirm the expected effect of wall steepness, i.e. for a constant film thickness, the steeper the wall the smaller the Re value at which supercritical separation occurs. However, the effect of film thickness, δ is not so trivial. This is manifested by Fig. 5.12, which shows the size of the eddy as a function of δ. For a constant Re, the eddy attains maximum size at $\delta \sim O(1)$, but decreases gradually for $\delta \gg 1$. Furthermore, the eddy shrinks fast and disappears altogether in the opposite limit $\delta \to 0$. This behaviour is contrasted to the subcritical separation (see Fig. 5.10), where $\delta \gg 1$ results in locally creeping flow and a geometrically separated eddy and $\delta \to 0$ results in a large, inertial separation.

The explanation for the above behaviour is as follows: For $\delta \gg 1$ the proportional change in flow cross-section becomes gradually smaller, and thus the separation is progressively less drastic and the eddy shrinks. At the other end, $\delta \to 0$ with $\zeta = constant$ results in $\xi \gg 1$, i.e. a film much thinner than the wall amplitude. This thin film readily deforms to follow the shape of the wall, because capillary forces are now insignificant. Therefore, the difference in the subcritical and supercritical separation (as shown respectively in Figs. 5.10 and 5.12) is mainly attributed to the variation in the significance of capillary forces.

For the parametric range where the eddy covers most of the corrugation trough, we define an effective film thickness, h_{eff} (measured from the top of the corrugation crests up to the nearly flat free surface), and compare the actual liquid flow rate on the corrugated wall to the flow rate of a Nusselt film of thickness h_{eff}. Accordingly,

Institutional Repository - Library & Information Centre - University of Thessaly
09/06/2024 06:51:43 EEST - 18.219.33.223

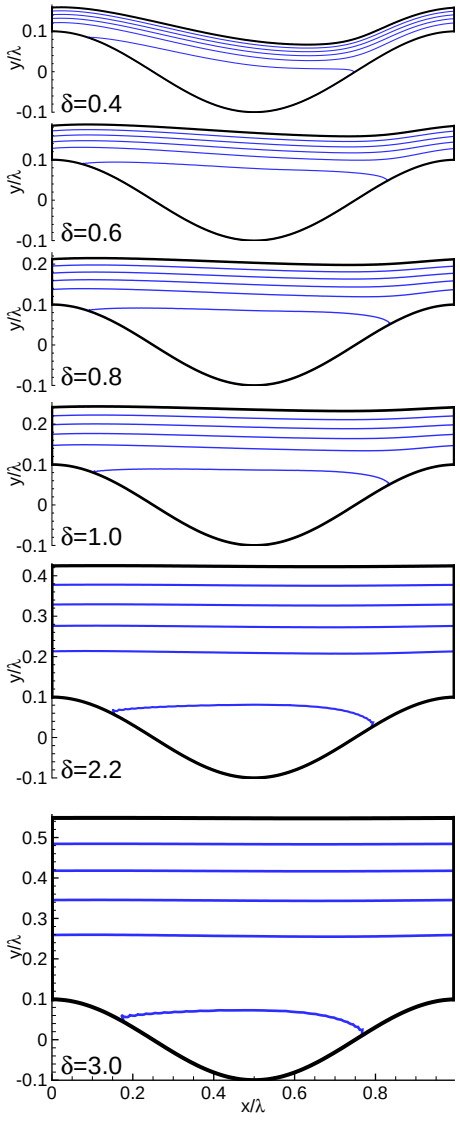

Figure 5.11: The flow structure in supercritical regime with increasing dimensionless film thickness for Re=300, ζ=$2\pi/10$, Bo^{-1}=5 and α=45^o.

Institutional Repository - Library & Information Centre - University of Thessaly
09/06/2024 06:51:43 EEST - 18.219.33.223

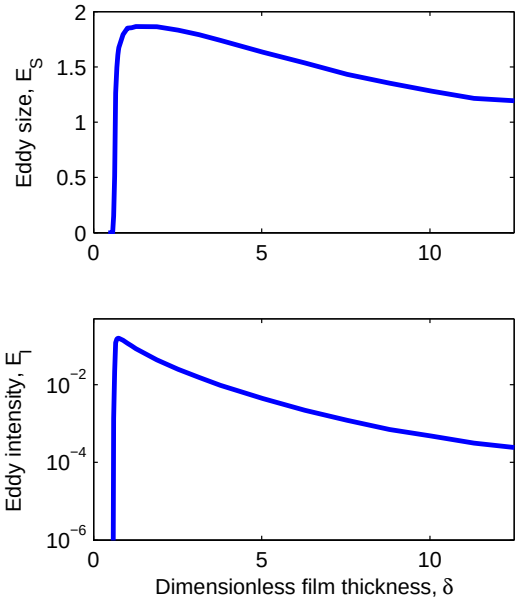

Figure 5.12: The effect of film thickness on the size and intensity of the supercritical eddy for ζ=$2\pi/5$, Bo^{-1}=5, Re=80 and α=45^o.

the flow rates along the actual, corrugated and the hypothetical flat wall are

$$q_{cor} = \frac{g \sin\alpha \, h_N^3}{3\nu} \quad \text{and} \quad q_{flat} = \frac{g \sin\alpha \, h_{eff}^3}{3\nu}$$

Their ratio, which is an implicit function of the dimensionless film thickness, is calculated as

$$r(\delta) = \frac{q_{cor}}{q_{flat}} = (\frac{h_N}{h_{eff}})^3 = (\frac{1}{H_{eff}})^3 \tag{5.14}$$

where H_{eff} is the effective film thickness scaled by h_N.

The flow rate ratio, r is computed in Fig. 5.13 as a function of δ for $\zeta = 2\pi/10$ and $\alpha = 45^o$. It is shown to attain values significantly higher than one when the eddies are large and cover most of the corrugation trough. Therefore, these eddies may be viewed as rollers that reduce viscous friction and allow higher flow rates at the same film thickness. An example of wall characteristics and fluid properties that would result in the dimensionless film thickness range depicted in Fig. 5.13, while remaining in the separated, supercritical regime, is provided by Table 5.1.

Based on the above, it is concluded that, under proper conditions, the liquid film flows faster on a sinusoidally corrugated than on a plane wall. This result provides motivation to study the related, but different, problem of an object sliding along a

Institutional Repository - Library & Information Centre - University of Thessaly
09/06/2024 06:51:43 EEST - 18.219.33.223

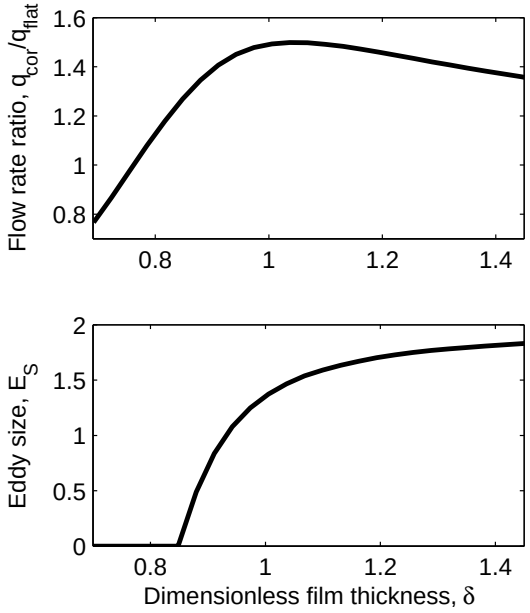

Figure 5.13: (a) The ratio of the actual flow rate along a corrugated wall to the hypothetical flow rate of a Nusselt film, with thickness equal to the distance from the crest to the flat free surface, for $\zeta=2\pi/10$, $Bo^{-1}=3.21$ and $\alpha=45^o$. (b) The respective eddy size.

liquid layer. More specifically, it would be of interest to question whether an object with undulated, rather than smooth, surface of contact with the liquid could possibly face less resistance to flow.

5.3.4 Flow Transition and Flow-Regime Maps

Approaching the condition of linear resonance is accompanied by an impressive modification in the structure of the flow. More specifically, the liquid film follows much more faithfully the shape of the wall and the separated regions shrink drastically and, if the wall is not very steep, disappear altogether. The suppression of the separation eddy in a window of Re has been conclusively demonstrated very recently (*Wierschem et al.*, 2010) by a combination of experiment and numerics. Therefore, we defer any further discussion of this phenomenon, and concentrate on the transition from the subcritical to the supercritical regime and on the parametric dependence of flow structure on the main dimensionless variables.

The typical variation in flow structure when moving from subcritical to supercritical conditions by increasing Re at constant δ is depicted in Fig. 5.14. This parametric evolution may be conceptually paralleled to a ballistics problem: Each corrugation

Institutional Repository - Library & Information Centre - University of Thessaly
09/06/2024 06:51:43 EEST - 18.219.33.223

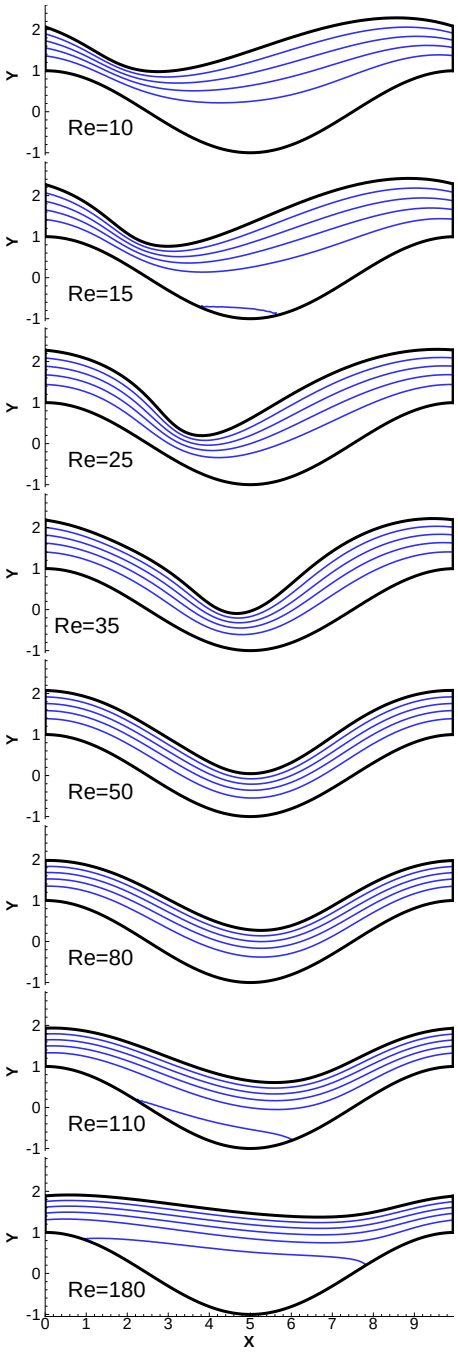

Figure 5.14: Parametric evolution of the flow structure as function of Re, for Bo^{-1}=5, δ=$2\pi/10$, ξ=1 and α=45^o. The subcritical regime at Re=10, 15 and 25, the resonance regime at Re=35 and 50 and the supercritical regime at Re=50, 80, 110 and 180.

Institutional Repository - Library & Information Centre - University of Thessaly
09/06/2024 06:51:43 EEST - 18.219.33.223

λ(m)	a(m)	$\nu(m^2/s)$	$\rho(g/mm^3)$	$\sigma(N/m)$
0.01	0.001	$1.08\times\ 10^{-5}$	1.1538	0.065
$h_N(m)$		δ		Re
0.0011		0.691150		26.3
0.0025		1.570796		309.3

Table 5.1: Characteristics of wall corrugation and of liquid properties, water-glycerol solution 60% at 20^oC, used in Fig. 5.13 as well as the range of values of δ and Re dependant on mean film thickness h_N.

cycle of the wall is viewed to consist of two sub-sections: one steeper, and one less steep than the mean inclination. The former may be perceived as an accelerator of the liquid and the latter as an ejection platform. If the liquid inertia is small, the jet will land in the upstream part of the next corrugation length, and will create there a local minimum in film thickness (Fig. 5.14, Re = 10, 15 and 25). Therefore, if a separation eddy forms, it will occur downstream of the film thickness minimum.

With increasing inertia, the landing point gradually reaches the trough of the next corrugation. Then, the liquid follows the shape of the wall, and separation diminishes or disappears altogether (Fig. 5.14, Re = 35 and 50). Further increase in inertia moves the landing point to the downstream side of the next corrugation, and as a result the separation eddy forms upstream of this point (Fig. 5.14, Re = 80, 110 and 180). When inertia is sufficient to cover the distance from one crest to the next, then flow separation extends over most of the trough and the streamlines above the separation eddy become practically straight.

The parametric dependence of the flow structure on the main system properties is summarized conveniently in the flow regime maps of Fig. 5.15a, b and 5.16a, b. Fig. 5.15a shows the values of Re and Bo^{-1} where the subcritical and supercritical eddies exist. Parameters ζ and δ are constant and are both equal to $2\pi/10$. These values result in a well-defined zone with no eddy around the resonance conditions. It is readily observed that, at the relatively small δ considered, subcritical separation dominates the capillary regime (high Bo^{-1}) and supercritical separation dominates the gravity regime (low Bo^{-1}).

By increasing the constant parameter values to $\zeta = \delta = 2\pi/5$, the corrugations become too steep and the resonance only shrinks (but does not totally eliminate) the separation eddy. The parametric region without eddies now reduces to the lower-left corner of the map, and a magnified view of this region is shown in Fig. 5.15b. As expected, with the increase in corrugation steepness, the onset of the supercritical eddy moves to much lower Re. It is also noted that, for $Bo^{-1} > 20$ the subcritical

Institutional Repository - Library & Information Centre - University of Thessaly
09/06/2024 06:51:43 EEST - 18.219.33.223

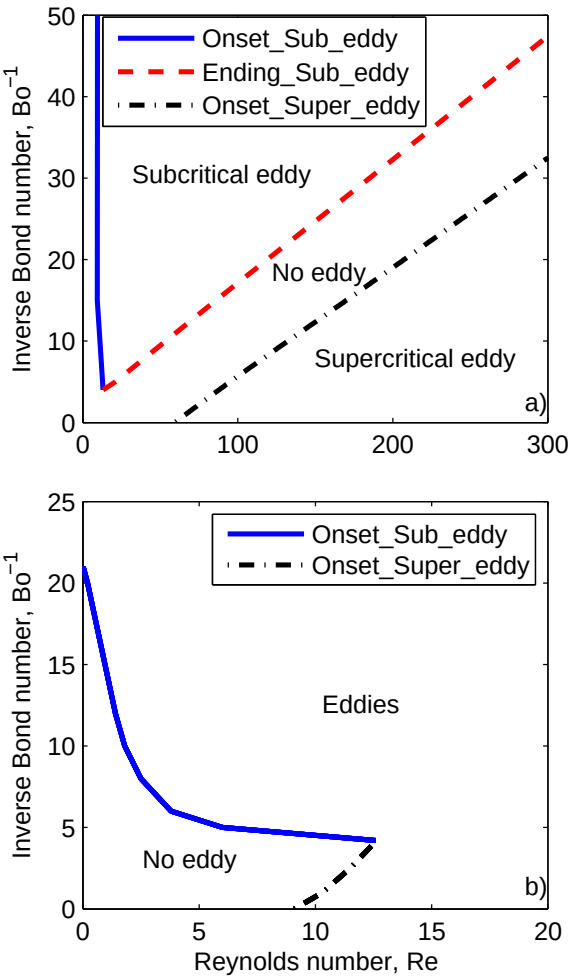

Figure 5.15: The maps of eddy separation in terms of Re and Bo^{-1} are made for two wall corrugations in a) ζ=δ=$2\pi/10$ and b) ζ=δ=$2\pi/5$ at other parameters ξ=1, α=45^o.

Institutional Repository - Library & Information Centre - University of Thessaly
09/06/2024 06:51:43 EEST - 18.219.33.223

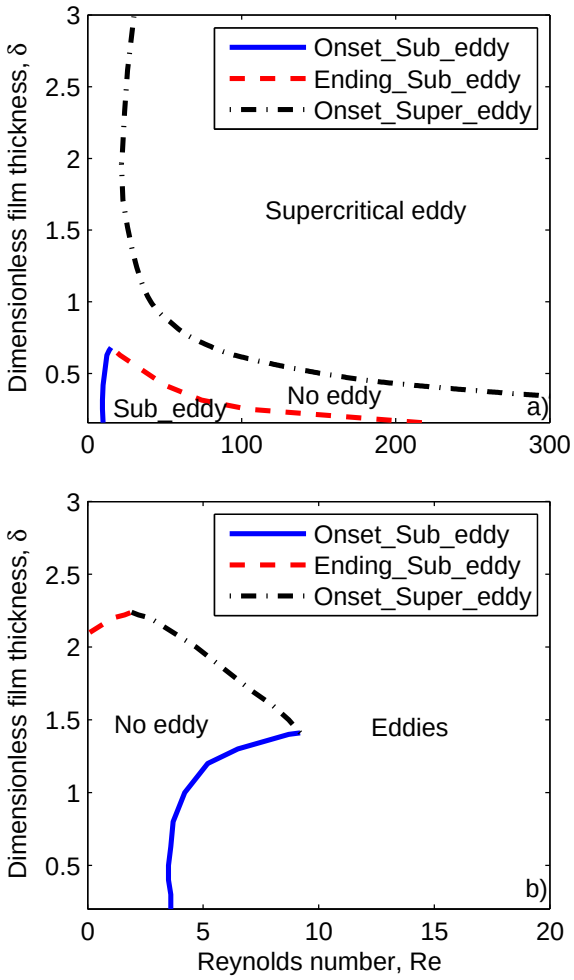

Figure 5.16: The maps of eddy separation in terms of Re and δ are made for two wall corrugations in a) ζ=$2\pi/10$ and b) ζ=$2\pi/5$ at other parameters Bo^{-1}=5, α=45^o.

Institutional Repository - Library & Information Centre - University of Thessaly
09/06/2024 06:51:43 EEST - 18.219.33.223

eddy exists even at $Re = 0$. Thus, geometric separation is facilitated at high Bo^{-1}, as is anticipated from the effect of capillary forces in the subcritical regime.

Fig. 5.16a shows the values of Re and δ where the subcritical and supercritical eddies exist. The parameters now held constant are $\zeta = 2\pi/10$ and $Bo^{-1} = 5$. It is readily observed that, at this relatively low Bo^{-1}, subcritical separation is dominant at low δ and supercritical at high δ. It is also noted that, above $\delta = 1.96$ the minimum Re for the onset of the supercritical eddy gradually increases once again. The latter observation is in line with the gradual shrinkage of the supercritical eddy as δ increases, noted in the previous section.

By increasing the dimensionless wall steepness to $\zeta = 2\pi/5$, the approach to resonance leads in shrinkage, but not total elimination, of the separation eddy. This behaviour is manifested in Fig. 5.16b, which shows that the parametric region without eddies is limited to small Re and small-to-intermediate δ.

5.3.5 Branch Disconnection at Very Steep Wall Corrugations

An effect of increasing wall steepness, which has already been discussed in the literature (*Heining et al.*, 2009), is the occurrence of bistability at high Bo^{-1}. Then, the relatively steep resonance curve of free surface amplification versus Re bends towards the supercritical regime. As a result, there is a range of Re, where multiple steady solutions co-exist.

Here, we report on another effect of steep corrugations, which occurs at low Bo^{-1}, i.e. when the linear resonance curve is blunt and exhibits a weak peak. Representative computational predictions with increasing wall steepness are shown in Fig. 5.17 for $Bo^{-1} = 5$ and $\delta = 2\pi/10$. They indicate that beyond $\xi = 1.6$ the resonance curve breaks into two disconnected branches, a subcritical and a supercritical one. The end of each branch marks a failure of the computer code to converge to a steady solution. It is interesting to note that the two branches cross, an indication that exchange of stability takes place.

Some characteristics of the two branches for $\xi = 2$, namely the relative amplitude and phase shift of the free surface, and the intensity of the wall eddy, are shown in Fig. 5.18. We note that there is a discontinuous jump in all characteristics, i.e. the two branches are genuinely different. In particular, the wall eddy disappears totally in the supercritical branch but persists in the subcritical one.

In Fig. 5.19 are shown the first three harmonics of the free surface deformation. It is evident that the subcritical solution is relatively more deformed at small length-scales. Fig. 5.20 shows the streamlines of the limiting solutions of the two branches.

Institutional Repository - Library & Information Centre - University of Thessaly
09/06/2024 06:51:43 EEST - 18.219.33.223

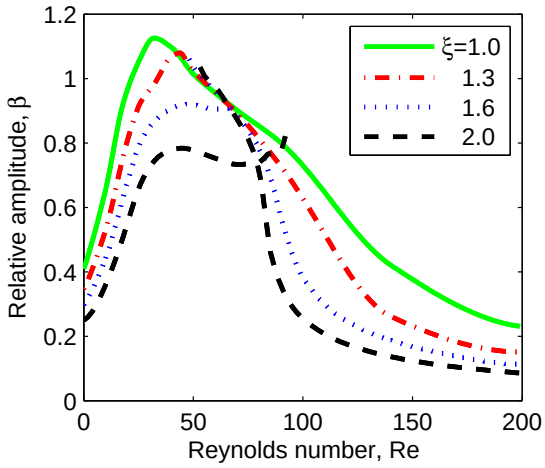

Figure 5.17: The disconnection of subcritical and supercritical branches with multiple solutions in the mid range of Re for increasing wall amplitude with δ=$2\pi/10$, Bo^{-1}=5, α=45^o.

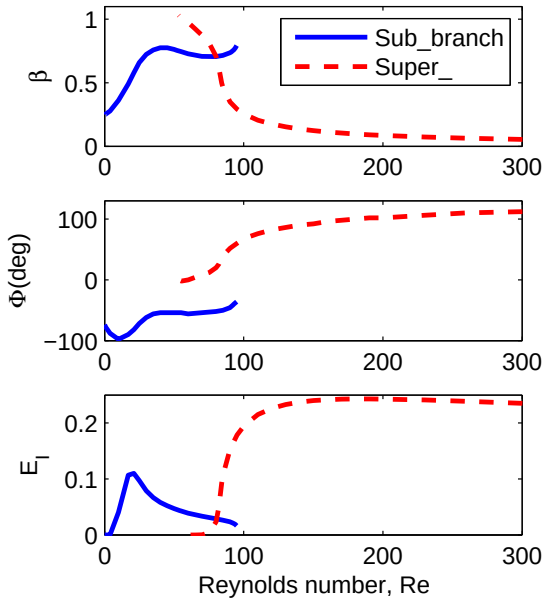

Figure 5.18: The plots depict the relative amplitude, the phase shift of free surface and the eddy intensity of the two disconnected subcritical and supercritical branches for film flow along a very steep corrugated wall with ξ=2, δ=$2\pi/10$, Bo^{-1}=5, α=45^o.

Institutional Repository - Library & Information Centre - University of Thessaly
09/06/2024 06:51:43 EEST - 18.219.33.223

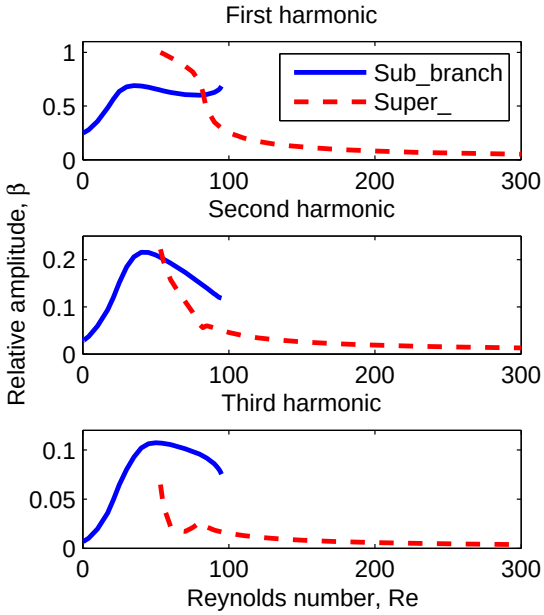

Figure 5.19: The plots show relative amplitude of three harmonics of the free surface with the same flow parameters as in Fig. 5.18.

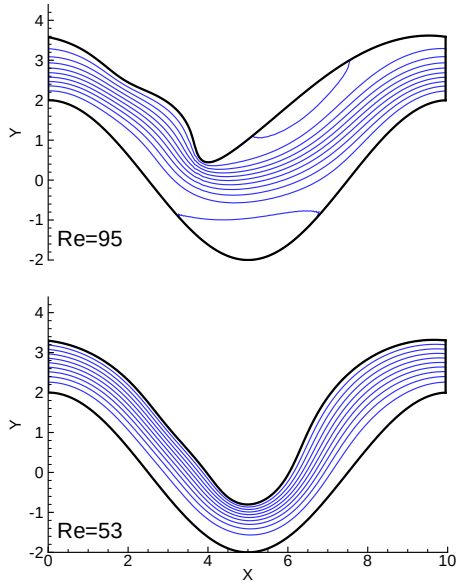

Figure 5.20: The limiting solutions of the two branches in Fig. 5.18 are obtained respectively at Re=95 (in subcritical branch) and Re=53 (in supercritical branch).

Institutional Repository - Library & Information Centre - University of Thessaly
09/06/2024 06:51:43 EEST - 18.219.33.223

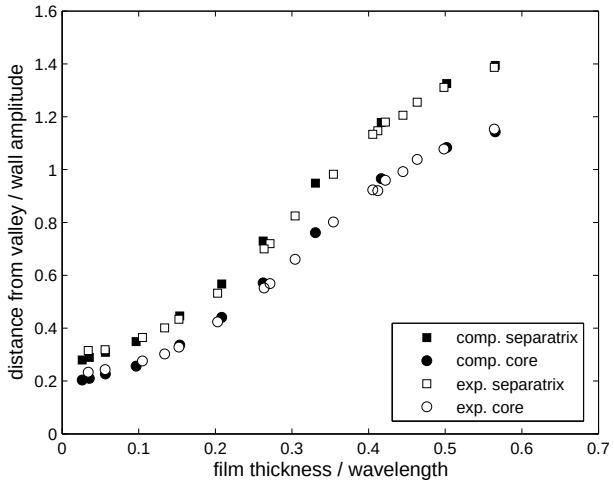

Figure 5.21: Comparison of data by *Wierschem et al.* (2003) (open symbols) to computational predictions (filled symbols) for the distance of the separatrix and the core of the eddy from the center of the trough. Creeping flow along a sinusoidal wall with wavelength 20 mm and amplitude 9 mm, at inclination 45^o.

It is interesting to observe that the subcritical solution features extensive capillary deformation on the upstream side of the free surface. It is also characterized by two separation eddies, one on the wall and another one on the downstream side of the free surface. On the contrary, the supercritical solution is almost in perfect phase with the wall and only exhibits a slight downstream bulge.

5.3.6 Comparison with Experiments

This concluding section serves to validate the accuracy of the computations by quantitative comparison with independent data taken at steady conditions. It also attempts to relate singular limits of the steady computations to experimentally observed hydraulic jumps (shocks) and recursive behaviours. To this end, we will exploit published data by the Aksel group (*Wierschem et al.*, 2003; *Wierschem and Aksel*, 2004a).

First, we consider the characteristics of the separation eddy under creeping flow conditions along a sinusoidal wall with wavelength 20 mm and amplitude 9 mm, inclined at 45^o. Fig. 5.21 compares data by *Wierschem et al.* (2003) (their Fig. 10) to our computations. The predicted vertical distance of the separatrix and the core of the eddy to the bottom of the trough is in very good agreement with the data over the entire range of measured film thickness.

Institutional Repository - Library & Information Centre - University of Thessaly
09/06/2024 06:51:43 EEST - 18.219.33.223

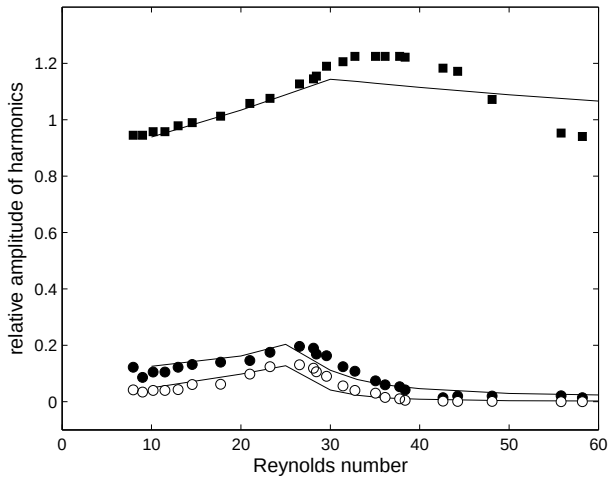

Figure 5.22: Comparison of data by *Wierschem and Aksel* (2004a) (symbols) to computational predictions (lines) of the first three harmonics of steady surface deformation over a range of Re. Flow along a wall with wavelength 300 mm and amplitude 15 mm, at inclination 15.1^o.

The effect of wall steepness on geometric separation under creeping flow is also very well predicted. More specifically, *Wierschem et al.* (2003) have shown (their Fig. 8) that at a waviness equal to 0.1 (equivalent to $\zeta = 2\pi/10$) there is no eddy as $Re \sim 0$, no matter how thick the film is. This is in line with our results depicted in Fig. 5.16a. On the contrary, a wall of waviness equal to 0.2 ($\zeta = 2\pi/5$), is observed to develop a separation eddy at a critical film thickness/wavelength equal to 0.34. This is again in quantitative agreement with our results, shown in Fig. 5.16b, which indicate that the critical dimensionless film thickness for the occurrence of separation at zero Re is $\delta = 2\pi \times 0.34$.

Next, we move to finite Re, and consider the characteristics of the free surface. *Wierschem and Aksel* (2004a) report the first three harmonics of the steady surface deformation over a wide range of Re, for flow along a wall with wavelength 300 mm and amplitude 15 mm. In Fig. 5.22 we reproduce their data together with our predictions. Rather satisfactory agreement is noted for the second and third harmonic, and also for the first harmonic up to $Re = 30$. Given the rather small ratio of channel width to wavelength (170/300), it is conjectured that the deviation at high Re is caused by finite-width effects. The observation that the disagreement appears in the first harmonic further supports this conjecture.

It is also confirmed that all the steady flow structures documented by *Wierschem and Aksel* (2004a) (their Fig. 11) appear as predictions of the present code. In

Institutional Repository - Library & Information Centre - University of Thessaly
09/06/2024 06:51:43 EEST - 18.219.33.223

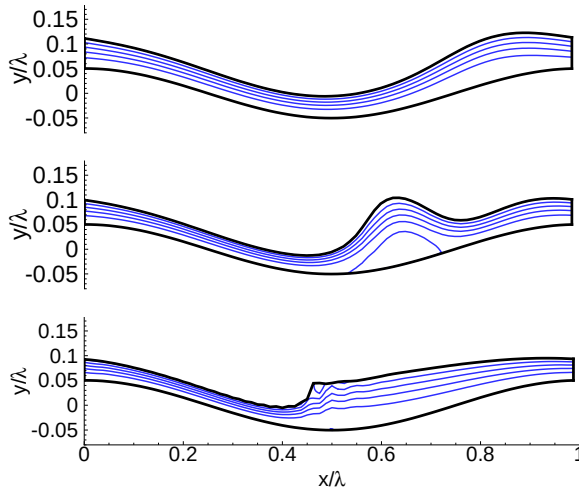

Figure 5.23: The flow structures at low inverse Bond number are shown as examples at fixed inclination angle α=9.9^o, fixed wall amplitude/wavelength = 0.015/0.298 and Bo^{-1}=0.005531. Different flow structures obtained by changing viscosity and mean film thickness are standing wave (upper plot) with Re = 41.28, δ=0.309548, ξ=1.020408; hump (middle plot) with Re=40.02, δ=0.246375, ξ=1.282051; and hydraulic jump (lower plot) with Re=17.5, δ=0.246375, ξ=1.282051.

particular, the first streamline plot in Fig. 5.23 shows a supercritical standing wave with a slight downstream bulge. With decreasing dimensionless film thickness, the bulge moves upstream and turns into a pronounced hump (second plot), which is accompanied by a recirculation region.

Finally, approaching the relevant experimental conditions, the computational steady solution steepens in the sense of a hydraulic jump, develops computational instabilities and eventually ceases to exist (third streamline plot in Fig. 5.23). It may reasonably be conjectured that the failure to converge to a steady solution is associated with the experimental observation of recursive build-up and degeneration of the hydraulic jump into three-dimensional structures (surface rollers, fingering).

5.4 Concluding Remarks

Steady flow of a liquid film along sinusoidal, steeply corrugated walls is investigated computationally by finite-element simulation of the 2D Navier-Stokes equations. The interaction of flow structures resulting from the shape of the wall and from the deformation of the free surface is parameterized by the Reynolds number, Re, the inverse Bond number, Bo^{-1}, the dimensionless wall steepness, ζ, and the dimensionless

Institutional Repository - Library & Information Centre - University of Thessaly
09/06/2024 06:51:43 EEST - 18.219.33.223

film thickness, δ, and is studied for a typical inclination angle $\alpha = 45^o$.

The overall behaviour is efficiently classified into a subcritical and a supercritical regime. The boundary is demarcated by the value, Re_{res}, where the wall corrugations are at resonance with capillary-gravity waves travelling against the flow and the free surface exhibits maximum deformation. The value of the inverse Bond number (mainly affected by the wall wavelength) defines the capillary and the gravity regimes. The capillary regime is characterized by a resistance to the deformation of the free surface at low Re, but also by strong wall-free surface resonance, and thus a significant deformation of the free surface at higher Re. On the contrary, the gravity regime is characterized by a relatively small deformation of the free surface and weak variation with Re.

As is intuitively expected, steeper walls trigger earlier flow separation at the trough, both in the subcritical and the supercritical regime. However, the separation characteristics in the two regimes vary significantly because capillary forces dominate over inertia forces in the former and vice-versa in the latter. More specifically, in the subcritical regime, the resistance to free surface deformation results in a pronounced separation eddy for very thin films and in the approach to a creeping flow eddy for very thick films. On the contrary, in the supercritical regime, separation disappears for very thin films (because the flow readily deforms to follow the wall) and gradually shrinks for very thick films (because the change in flow cross-section becomes less drastic).

At very high values of wall steepness, the solution breaks into two, intersecting branches. It is conjectured that this topological change of the solution is associated with recursive behaviours that have been documented from independent experiments. Also, computational predictions in the appropriate parametric range agree with observations of steady flow, and failure of the code to converge appears relevant to the experimentally recorded formation of shocks.

Institutional Repository - Library & Information Centre - University of Thessaly
09/06/2024 06:51:43 EEST - 18.219.33.223

CHAPTER VI

Unsteady Flow along Periodic Corrugations

6.1 Introduction

Liquid film flow along corrugated substrates can be encountered in nature and in several industrial applications. It occurs in a variety of scales ranging from environmental flows (*Balmforth and Liu*, 2004), mesoscale flows in two-phase heat exchangers (*Webb*, 1994), in mass transfer equipment (*deSantos et al.*, 1991; *Valluri et al.*, 2005; *Helbig et al.*, 2009), or in coating processes (*Quere*, 1999; *Weinstein and Ruschak*, 2004), to biomedical flows (*Bull and Grotberg*, 2003). More information can be extensively found in the reviews by *Oron et al.* (1997); *Chang et al.* (2002); *Craster and Matar* (2009). Wall corrugation induces a rich physical behaviour in liquid film flow and makes it particularly more interesting (*Wierschem and Aksel*, 2004a). First studies on the problem dated back since late 70s early 80s (*Tougou*, 1978; *Wang*, 1981).

Different research approaches with relevant assumptions have been carried out. Initial theoretical works simplified the problem to a special case of creeping flow for asymptotic analysis (*Wang*, 1981) and numerics on Stokes-flow (*Pozrikidis*, 1988; *Shetty and Cerro*, 1993). They studied a steady deformation of free surface of liquid film flow along sinusoidal wall. On the other hand, the assumption of infinitesimal amplitude of wall corrugation makes the problem analytically more tractable at finite inertia. However, the imposition of even small wall amplitude on the deformation of free surface flow is non-trivial. It is observed that there is a linear resonance of a flow in finite range of Reynolds number (*Bontozoglou and Papapolymerou*, 1997; *Trifonov*, 1999; *Luo and Pozrikidis*, 2006; *Wierschem et al.*, 2008). Another assumption is of very small film thickness, so the effect of finite-steepness corrugation can be questioned. Again, it corroborates the nonlinear resonance between free surface

Institutional Repository - Library & Information Centre - University of Thessaly
09/06/2024 06:51:43 EEST - 18.219.33.223

deformation and wall corrugation in an appropriate range of parameters (*Heining et al.*, 2009).

Other topographical walls were also questioned. Periodic orthogonal wall was studied to depict its effect on free surface morphology and vortical structure of steady flow (*Argyriadi et al.*, 2006; *Pak and Hu*, 2011). Another aspect of substrate with topographical feature, such as single step-in or step-out, was studied to provide more specific physical understanding relevant to defect or intentional design of industrial equipments (*Kalliadasis and Homsy*, 2001; *Gaskell et al.*, 2004; *Bontozoglou and Serifi*, 2008).

In order to work on flow instability, most studies approached to film flow along wall corrugation traditionally with low-dimensional models by assuming very small amplitude of corrugation or very thin mean film thickness. These publications followed the classical long-wave expansion originated from the one for planar wall (*Benjamin*, 1957; *Yih*, 1963) and implicitly excluded the possible effect of short wave. However, they could provide specific pieces of information on corrugated-wall film flow. *Davalos-Orozco* (2007) employed the long-wave equation of Benney type and introduced a local perturbation of air pressure on free surface. He found that perturbation can be dampened and disappears with a proper wavelength of corrugation. Dynamics of flow on periodic wall by *Oron and Heining* (2008) based on the first-order WRIBL-type (Weighted Residual Integral Boundary Layer) set of equations presented periodic flow beyond a critical threshold, then travelling wave, and ending up in unstationary state. He predicted that the effect of corrugation on flow extends the critical Reynolds number to higher value than on planar wall. *D'Alessio et al.* (2009) derived a second-order model and stated that corrugation reduces stability of flow at large Weber number and with thick film flow. This instability is monotonic and increases with corrugation amplitude. The onset of instability is of short wavelength which approaches to the one of high-amplitude corrugation. *Heining and Aksel* (2009) predicted that corrugation can cause either instability or stability depending on surface tension or corrugation wavelength.

Another effective approach to instability is to use a curvilinear coordinate system following wall corrugation. It satisfactorily captures recirculation eddies around bottom trough. *Wierschem and Aksel* (2003) studied corrugation of very large wavelength and showed that the delay of critical threshold to higher value than in that of flat wall occurs at low inclination angle. On the contrary, larger inclination resulted in lower critical one. *Hacker and Uecker* (2009) derived a WRIBL type model. It interestingly predicted that corrugation does not have monotonic effect but can cause

Institutional Repository - Library & Information Centre - University of Thessaly
09/06/2024 06:51:43 EEST - 18.219.33.223

opposite ones either stability or instability. By the same method, *Nguyen and Plourde* (2011) studied the behaviour of free surface in terms of inclination angle, quantified by the area ratio of free surface to the corrugation bottom. The instability of corrugated-wall film flow was additionally questioned by considering the addition of surfactant (*Pozrikidis*, 2003) or the application of electric field (*Tseluiko et al.*, 2008, 2009). By using different low-dimension models bound with constraint assumptions, conclusions on flow instability are quantitatively incomparable and often contradictory to each other, not to mention due to different range of geometric and physical parameters. It is also emphasized that these models by their nature encounter difficulties in reflecting rigorously the physics of flow structure due to the fact that their ad-hoc assumption of velocity profile always misses the information on recirculation eddies around the trough (*Wierschem et al.*, 2003; *Wierschem and Aksel*, 2004a,b; *Scholle et al.*, 2004; *Wierschem et al.*, 2010; *Nguyen and Bontozoglou*, 2011). Typically, *Trifonov* (1999) carried out the first theoretical study on instability of corrugated-wall film-flow, using the long-wave IBL (Integral Boundary Layer) equations derived from the ad-hoc parabolic profile of crosswise velocity and apparently missed the short-wave mode.

Also for the first time, a paper by *Trifonov* (2007) on corrugated-wall film-flow was unique by using the full Navier-Stokes equations. He rigorously employed the Floquet theory for the instability analysis of steady flow. He stated that a vertical flow can be stabilized by corrugation wall at a large Reynolds under any disturbance wavelength. His data showed that using wall corrugation appropriately matching with liquid properties, flow can be stable under conditions that make it unstable along flat wall. Therefore, a well tailored wall can delay significantly the critical threshold. On the other hand, corrugation can cause instability and reduce the critical threshold of even short-wave disturbance. Despite of his robust data by the full governing equations and systematically parametric study, the physical mechanism enhancing the stabilization of flow by corrugation wall was not yet explained as well as the dynamic evolution of long or short wave disturbance not yet understood.

On the experimental side, there are few data on film flow along corrugation. *Vlachogiannis and Bontozoglou* (2002) observed inertia flow along periodic orthogonal wall (with rectangular step-in and step-out). Flow stabilization is showed to be significantly enhanced by a corrugation wavelength $12mm$, being in the effective acting of surface tension. It increases with inclination angle from $1 - 8°$. Making a similar conclusion but with a periodic sinusoidal wall of large wavelength ($300mm$), *Wierschem et al.* (2005) dictated that the flow is merely stabilized by the corrugation.

Earlier theoretical studies mostly either neglected short-wave periodic forcing of

Institutional Repository - Library & Information Centre - University of Thessaly
09/06/2024 06:51:43 EEST - 18.219.33.223

the wall in their long-wave expansion or did not discuss the modulation of free surface wave by the corrugation. This work is developed both for time-dependent problem and for stability analysis to solve the remaining unanswered questions. I will carry out study on the evolution of free surface and flow structure by DNS. It aims at providing a physical understanding of stabilization effect by corrugation on film flow. Preliminary results are necessarily shown to describe dynamical evolution of free surface wave disturbance. The latter manifests interesting behaviour due to additional interaction of wall corrugation to flow, which activates energy transfer from long-wave to short-wave mode. The chapter outline is as follows: Sect. 6.2 describes the computational methodology for the time dependent nonlinear problem, Sect. 6.3 develops the computational methodology for the linearized problem, Set. 6.4 present DNS results and discussion about the stabilizing effect by corrugation and the short-wave mode primary instability; and finally some concluding remarks are drawn in Sec. 6.5.

6.2 Formulation of the Problem and Computational Methodology

6.2.1 Time Dependent Formulation

The gravity-driven liquid film flows are considered along a periodic substrate which comprises of a number k_c of bottom corrugations of wavelength λ and amplitude a, inclined at an angle α with the horizontal plane (Fig. 6.1). The problem is modelled

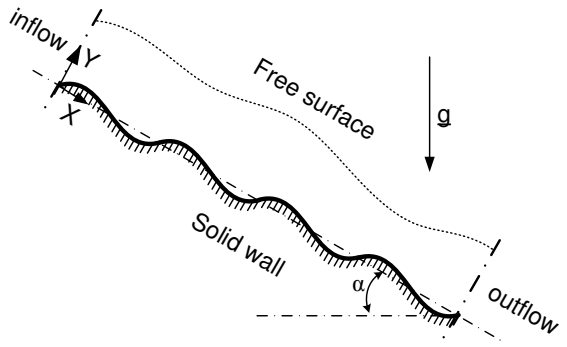

Figure 6.1: The configuration of film flow along sinusoidal corrugated wall.

as two-dimensional in a Cartesian coordinate system, with the x-axis pointing in the mean flow direction and the y-axis across the film. The respective dimensional velocity components are u and v. The liquid is incompressible and Newtonian, with

Institutional Repository - Library & Information Centre - University of Thessaly
09/06/2024 06:51:43 EEST - 18.219.33.223

density ρ, dynamic viscosity μ or kinematic viscosity $\nu = \mu/\rho$, and surface tension σ. The evolution of the free surface in time t is described as $y = h(x,t)$.

The full Navier-Stokes equations governing the two-dimensional flow are non-dimensionalized using as characteristic scales the mean film thickness and the mean velocity,

$$h_N = \left(\frac{3\,\nu\,q}{g\sin\alpha}\right)^{1/3}, \tag{6.1}$$

$$u_N = \frac{h_N^2\,g\sin\alpha}{3\,\nu}, \tag{6.2}$$

of the uniform Nusselt solution transporting the same mean flow rate q, where g is the gravity. Specifically, the dimensional variables are scaled as follows:

$$X = x/h_N;\; Y = y/h_N;\; H = h/h_N;$$
$$U = u/u_N;\; V = v/u_N;\; P = p/(\rho\,u_N^2);\; T = t/(h_N/u_N).$$

The resulting continuity and momentum equations are formulated as follows, with capital letters indicating the respective dimensionless variables:

$$\mathbb{C} := \nabla\cdot\underline{U} = 0, \tag{6.3}$$

$$\mathbb{M} := \frac{\partial\underline{U}}{\partial T} + \underline{U}\cdot\nabla\underline{U} + \nabla P - \frac{1}{Re}\nabla^2\underline{U} - \frac{3}{Re\sin\alpha}\underline{g} = \underline{0}. \tag{6.4}$$

Beside the unknowns to be solved in a confined problem which are the two velocity components, $\underline{U}(\underline{X},T) = [U,V]^T$, and the pressure $P(\underline{X},T)$, this free surface problem requires to determine the free surface height $H(X,T)$ by imposing the kinematic equation, describing its evolution,

$$H_T + UH_X - V = 0.$$

By the parametric mapping in Eq. (2.11), the derivative term H_X can be rewritten as $\dfrac{\partial H}{\partial X} = \dfrac{H_{\boldsymbol{\xi}}}{X_{\boldsymbol{\xi}}}$, where $\boldsymbol{\xi}$ is the coordinate along the free surface described by $\boldsymbol{\eta} = 1$. Noting that the bold font of ξ and η denote the global coordinates of computational domain. So the kinematic equation can be rewritten as,

$$\mathbb{K} := H_T\,X_{\boldsymbol{\xi}} + UH_{\boldsymbol{\xi}} - V\,X_{\boldsymbol{\xi}} = 0, \tag{6.5}$$

The boundary condition prescribing the flow along the wall is the no-slip and

Institutional Repository - Library & Information Centre - University of Thessaly
09/06/2024 06:51:43 EEST - 18.219.33.223

no-penetration boundary conditions,

$$U = V = 0. \tag{6.6}$$

The computational domain is studied for a liquid film flowing along multiple periodic corrugations. The bottom wall has a length, l, consisting of k_c periodic corrugations of wavelength, λ, so $l = k_c\,\lambda$. Each periodic corrugation of amplitude a has a sinusoidal profile,

$$y = w(x) = a\cos(2\pi\frac{x}{\lambda}). \tag{6.7}$$

At this point, a good characteristic length, which is the capillary length $l_c = \sqrt{\sigma/(\rho g \sin\alpha)}$, is proposed for scaling the wavelength of the periodic corrugation, $\lambda_c = \lambda/l_c$ as it can distinguish three different regimes, i.e. strong capillary, capillary-gravity, and gravity regime. Then, the equation (6.7) can be rewritten as

$$\frac{y}{h_N} = \frac{a}{\lambda}\frac{\lambda}{l_c}\frac{l_c}{l_\nu}\frac{l_\nu}{h_N}\cos\left[2\pi\frac{x}{h_N}\frac{h_N}{l_\nu}\frac{l_\nu}{l_c}\frac{l_c}{\lambda}\right],$$

or,

$$Y = W(X) = A\,\lambda_c\,(Ka)^{1/2}\,(3Re)^{-1/3}\cos\left[2\pi X\,(3Re)^{1/3}(Ka)^{-1/2}\frac{1}{\lambda_c}\right]. \tag{6.8}$$

With this scaling, the dimensionless profile of the bottom periodic corrugation exposes an explicit connection with both the liquid properties and the flow rate by including dimensionless variables (Ka) and (Re) respectively. Finally, the dynamical balance of the shear stress with the capillary force along the free surface is expressed as,

$$\underline{\underline{T}}\cdot\underline{n} = \Delta\,P\,\underline{n} + 3^{1/3}\,Ka\,Re^{-5/3}\,K\underline{n}. \tag{6.9}$$

In equation (6.9), $\underline{\underline{\mathrm{T}}}$ is the stress tensor,

$$\underline{\underline{T}} = -P\underline{\underline{I}} + \frac{1}{Re}\begin{bmatrix} 2\,U_X & U_Y + V_X \\ U_Y + V_X & 2\,V_Y \end{bmatrix}, \tag{6.10}$$

and $\underline{\mathrm{n}}$ is the outward unit normal vector on the free surface,

$$\underline{n} = \frac{(-H_X,\,1)^*}{\sqrt{1+H_X^2}},$$

Institutional Repository - Library & Information Centre - University of Thessaly
09/06/2024 06:51:43 EEST - 18.219.33.223

K is the surface curvature

$$K = \frac{H_{XX}}{\left(1 + H_X^2\right)^{3/2}}.$$

Beside that, there is a pressure jump term $\Delta P = P_{ref} - P_{gas}$ on the right hand side of the equation (6.9) due to the computed relative pressure based on a reference pressure, P_{ref} set at some point in the flow domain, e.g. at the top of its inlet. This pressure term arises as an additional variable which requires one more equation to avoid a degeneracy of the problem by imposing the mass of liquid being equal to the mass of the Nusselt mean flow on the domain length, $l = L\,h_N$ and $L = k_c\,\lambda_c\,\dfrac{l_c}{h_N}$,

$$m = \int_0^l \left[h(x,t) - w(x)\right]\,dx = h_N\,l.$$

or in the dimensionless form,

$$\frac{1}{L}\int_0^L \left[H(X,T) - W(X)\right]\,dX = 1. \tag{6.11}$$

6.2.2 Dimensionless Parameters

The dimensionless parameters arisen in the problem are the Reynolds number (in Eqs. (6.4)),

$$Re = \frac{q}{\nu} = \frac{1}{3}\left(\frac{h_N}{l_\nu}\right)^3, \tag{6.12}$$

with the viscous length, $l_\nu = \left[\nu^2/(g\sin\alpha)\right]^{1/3}$, and the mean inclination angle, α. In Eqs. (6.4), the unit normal vector $\underline{g}$ pointing in the gravity direction $\underline{g} = \left[\sin\alpha \quad -\cos\alpha\right]^T$, indicates the importance of each gravity component. Three other dimensionless parameters, appear in equations (6.8) and (6.9), namely the corrugation steepness,

$$A = \frac{a}{\lambda}, \tag{6.13}$$

the ratio of the corrugation wavelength with respect to the capillary length,

$$\lambda_c = \frac{\lambda}{l_c}, \tag{6.14}$$

Institutional Repository - Library & Information Centre - University of Thessaly
09/06/2024 06:51:43 EEST - 18.219.33.223

and the Kapitsa number which only depends on the liquid properties,

$$Ka = \left(\frac{l_c}{l_\nu}\right)^2. \tag{6.15}$$

6.2.3 Computational Method for Time Dependent Formulation

Applying the Galerkin-Finite Element Method, the governing equations (6.3), (6.4) and (6.5) are integrally weighted to produce the continuity, momentum and kinematic residuals respectively,

$$R_C^i := \iint_V \nabla \cdot \underline{U} \Psi^i \, dV = 0, \tag{6.16}$$

$$\underline{R}_M^i := \iint_V \left(\underline{U}_T + \underline{U} \cdot \nabla \underline{U} - \nabla \cdot \underline{\underline{T}} - \frac{3}{Re \sin\alpha} \underline{g} \right) \Phi^i \, dV = 0, \tag{6.17}$$

$$R_K^i := \int_S \left(H_T \, X_\xi + U \, H_\xi - V \, X_\xi \right) \Phi^i d\xi = 0, \tag{6.18}$$

where,

- In Eq. (6.16), Ψ^i is the bilinear basis function assigned at i^{th} node (where $\Psi^i = 0$). In Eqs. (6.17) Φ^i is the biquadratic basis function at i^{th} node, and in Eq. (6.18) $\Phi^i(\xi, \eta = 1)$ is set for nodes on the free surface ($\eta = 1$) and becomes actually the quadratic basis function.

- The velocity, the pressure, the free surface height elsewhere in the flow are interpolated elementwise from the pertinent nodal unknowns in the same element,

$$\underline{U} = \sum_{j=1}^{9} \underline{U}_j \Phi^j; \quad P = \sum_{j=1}^{4} P_j \Psi^j; \quad H = \sum_{j=1}^{3} H_j \Phi^j(\xi, \eta = 1), \tag{6.19}$$

  where the tessellation of each element consists of nine nodal velocities $\underline{U}_j$, four nodal pressures P_j and three nodal heights H_j.

- V and S are the whole flow domain and the free surface of the flow. The continuity, momentum, and kinematic residuals in Eqs. (6.16), (6.17), and (6.18) at each i^{th} node are respectively evaluated elementwise by the four-point, nine-point, and three-point Gauss quadratures. The number of equations R_C^i, $\underline{R}_M^i$, and R_K^i are equal to the number of the nodal unknown variables P_i, $\underline{U}_i$, and H_i respectively.

Institutional Repository - Library & Information Centre - University of Thessaly
09/06/2024 06:51:43 EEST - 18.219.33.223

In order to avoid the second derivative of the velocity in Eqs. (6.17), the integration can be rewritten as follows by mean of the divergence theorem,

$$\nabla \cdot (\Phi^i \underline{\underline{T}}) = \Phi^i (\nabla \cdot \underline{\underline{T}}) + \underline{\underline{T}} \cdot \nabla \Phi^i,$$
$$\iiint_V (\nabla \cdot \underline{\underline{T}}) \Phi^i \, dV = \int_\Omega \Phi^i \underline{\underline{T}} \cdot \underline{n} \, d\Omega - \iiint_V \underline{\underline{T}} \cdot \nabla \Phi^i \, dV,$$

then,

$$\underline{R}^i_M := \iiint_V \left[\left(\frac{\partial \underline{U}}{\partial T} + \underline{U} \cdot \nabla \underline{U} - \frac{3}{Re \sin \alpha} \underline{g} \right) \Phi^i + \underline{\underline{T}} \cdot \nabla \Phi^i \right] dV - \int_\Omega \Phi^i \underline{\underline{T}} \cdot \underline{n} \, d\Omega = 0. \tag{6.20}$$

In the Eqs. (6.20), the surface integration is done around the boundary Ω of the flow domain, which can be divided into the inflow (Ω_1), outflow (Ω_2), free surface ($S = \Omega_3$) and solid wall(Ω_4) boundaries. Here,

- For any i^{th} node at inlet, outlet and inside flow domain, the surface integration of the residual (in Eqs. (6.20)) is cancelled out from both sides of surface ($\underline{n}$ takes opposite sign),
$$\underline{R}^i_{MS} := \int_\Omega \Phi^i \underline{\underline{T}} \cdot \underline{n} \, d\Omega = 0.$$

- If the i^{th} node is on the solid wall ($U_i = V_i = 0$), the relating residual and its derivatives are simply given as,
$$\underline{R}^i_M = 0; \quad \frac{\partial \underline{R}^i_M}{\partial U_i} = 1; \quad \frac{\partial \underline{R}^i_M}{\partial V_i} = 1.$$

- Finally, the surface integration requires the evaluation only at any i^{th} node along the free surface, $\int_\Omega \rightarrow \int_S$.

Due to the stress balance along the free surface given in Eq. (6.9), the surface integration term can be rewritten as follows,

$$\underline{R}^i_{MS} := -\int_S \Phi^i \underline{\underline{T}} \cdot \underline{n} \, dS = -\int_S (\nabla P + We \, K) \, \underline{n} \, \Phi^i \, dS = \underline{R}^i_{MS1} + \underline{R}^i_{MS2} \tag{6.21}$$

where $We = 3^{1/3} Ka \, Re^{-5/3} = \dfrac{\sigma}{\rho U^2 H}$ is the Weber number. The outward normal unit

Institutional Repository - Library & Information Centre - University of Thessaly
09/06/2024 06:51:43 EEST - 18.219.33.223

is explicitly expressed by $\underline{n} = \dfrac{(-Y_\xi, X_\xi)^*}{\sqrt{X_\xi^2 + Y_\xi^2}}$ where ξ, η are two coordinates of the computational domain related to the X, Y of the physical domain by the isoparametric transformation,

$$X = L\xi; \quad Y = (H(X,T) - W(X))\eta + W(X), \tag{6.22}$$

with ξ and η vary in the range $[0,1]$. For the free surface, it is known $\eta = 1$ hence the arclength, dS, is a parametric curve in terms of ξ, $dS = \sqrt{dX^2 + dY^2} = \sqrt{X_\xi^2 + Y_\xi^2}\, d\xi$. Now, the first term of the surface integration in Eq. (6.21) are treated separately as follows,

$$\underline{R}^i_{MS1} := -\int_S \nabla P \underline{n} \Phi^i \, dS, \tag{6.23}$$

$$R^i_{MS1X} := -\int_S \nabla P \frac{Y_\xi}{\sqrt{X_\xi^2 + Y_\xi^2}} \Phi^i \, dS = -\int_S \nabla P Y_\xi \Phi^i d\xi, \tag{6.24}$$

$$R^i_{MS1Y} := -\int_S \nabla P \frac{X_\xi}{\sqrt{X_\xi^2 + Y_\xi^2}} \Phi^i \, dS = -\int_S \nabla P X_\xi \Phi^i d\xi, \tag{6.25}$$

The second term is rewritten by using the curvature definition, $K\underline{n} = \dfrac{d\underline{t}}{dS}$ where $\underline{t}$ is the unit tangential vector, $\underline{t} = \dfrac{(X_\xi, Y_\xi)^*}{\sqrt{X_\xi^2 + Y_\xi^2}}$,

$$\underline{R}^i_{MS2} := -\int_S We \frac{d\underline{t}}{dS} \Phi^i \, dS = -We \int_S \Phi^i d\underline{t} = -We \left[\left\{ \Phi^i \underline{t} \right\}_{First\,node}^{Last\,node} - \int_S \underline{t} \frac{\partial \Phi^i}{\partial \xi} d\xi \right], \tag{6.26}$$

$$R^i_{MS2X} := -We \left[\left\{ \Phi^i \frac{X_\xi}{\sqrt{X_\xi^2 + Y_\xi^2}} \right\}_{First\,node}^{Last\,node} - \int_S \frac{X_\xi \Phi^i_\xi}{\sqrt{X_\xi^2 + Y_\xi^2}} d\xi \right], \tag{6.27}$$

$$R^i_{MS2Y} := -We \left[\left\{ \Phi^i \frac{Y_\xi}{\sqrt{X_\xi^2 + Y_\xi^2}} \right\}_{First\,node}^{Last\,node} - \int_S \frac{Y_\xi \Phi^i_\xi}{\sqrt{X_\xi^2 + Y_\xi^2}} d\xi \right], \tag{6.28}$$

The periodic boundary condition is applied for the inlet and outlet of the flow domain, so the first node and the last node on the free surface take the same value of the

Institutional Repository - Library & Information Centre - University of Thessaly
09/06/2024 06:51:43 EEST - 18.219.33.223

unknown variables and the terms in the curly bracket become zero,

$$\left\{ \Phi^i \frac{X_\xi}{\sqrt{X_\xi^2 + Y_\xi^2}} \right\}_{First\,node}^{Last\,node} = 0, \quad \left\{ \Phi^i \frac{Y_\xi}{\sqrt{X_\xi^2 + Y_\xi^2}} \right\}_{First\,node}^{Last\,node} = 0.$$

Finally, the two X and Y components of the momentum residual are expressed as follows ready for numerical implementation,

$$\begin{aligned} R^i_{MX} := \iint_V \Bigg[\left(U_T + U\,U_X + V\,U_Y - \frac{3}{Re \sin\alpha} \sin\alpha \right) \Phi^i + \left(-P + \frac{2}{Re} U_X \right) \Phi^i_X \\ + \frac{1}{Re} \left(U_Y + V_X \right) \Phi^i_Y \Bigg]\, dV + \int_S \Delta P Y_\xi \Phi^i \, d\xi + We \int_S \frac{X_\xi \Phi^i_\xi}{\sqrt{X_\xi^2 + Y_\xi^2}} \, d\xi, \end{aligned} \tag{6.29}$$

$$\begin{aligned} R^i_{MY} := \iint_V \Bigg[\left(V_T + U\,V_X + V\,V_Y + \frac{3}{Re \sin\alpha} \cos\alpha \right) \Phi^i + \frac{1}{Re} \left(U_Y + V_X \right) \Phi^i_X \\ + \left(-P + \frac{2}{Re} U_Y \right) \Phi^i_Y \Bigg]\, dV - \int_S \Delta P X_\xi \Phi^i \, d\xi + We \int_S \frac{Y_\xi \Phi^i_\xi}{\sqrt{X_\xi^2 + Y_\xi^2}} \, d\xi, \end{aligned} \tag{6.30}$$

To this point, the number of nodal residuals of the governing equations in Eqs. (6.16), (6.18) and (6.20) corresponds to the number of the nodal unknown variables. However, due to setting a pressure datum at a reference grid node in the flow, the residual of the continuity at that node is set a priori. This setting results in a pressure difference between the pressure datum and the uniform gas pressure in the dynamical balance at the gas-liquid interface, as shown in Eq. (6.9). The unknown variables of pressure difference, ΔP, requires an additional equation of liquid mass in the flow domain in order that the problem is well defined, as follows

$$M := \int_0^L (H - W)\, dX = L, \tag{6.31}$$

$$R_{MASS} := \int_0^L (H - W)\, dX - L = 0. \tag{6.32}$$

Until now, the vector of the nodal unknown variables,

$$\underline{Q} = [U^1, V^1, \cdots, U^N, V^N, P^1, \cdots, P^{NP}, H^1, \cdots, H^{NH}, \Delta P],$$

Institutional Repository - Library & Information Centre - University of Thessaly
09/06/2024 06:51:43 EEST - 18.219.33.223

corresponds fully to the vector of the residuals,

$$\underline{R} = [R^1_{MX}, R^1_{MY}, \cdots, R^N_{MX}, R^N_{MY}, R^1_C, \cdots, R^{NP}_C, R^1_K, \cdots, R^{NH}_K, R_{MASS}].$$

The indices N, NP, and NH denote respectively the number of unknown nodal velocities, unknown nodal pressures, and unknown nodal free surface height in the flow domain, where one unknown nodal pressure is set as a datum value which results in an additional variable of pressure difference to count for the dynamical balance at the gas-liquid interface. The nodal residuals of the governing equations, Eqs. (6.16), (6.18) and (6.20) and the additional mass equation (6.31) are discretised in time, if it is time-dependent, using the Crank-Nicolson (C.N.) scheme, and are integrally weighted by the Gaussian quadratures: the nine-point Gaussian quadrature for the domain integration and the three-point for the surface one. The basic C.N. scheme is as follows,

$$\frac{\partial \underline{Q}}{\partial T} + \underline{L}(\underline{Q}) = 0, \qquad \frac{\partial \underline{Q}}{\partial T} + \frac{1}{2}\left[\underline{L}(\underline{Q}^{n+1}) + \underline{L}(\underline{Q}^n)\right] = \underline{0}. \tag{6.33}$$

For the integrated residuals of the governing equations, the extended Crank-Nicolson scheme gives:

$$R^i := \int_V \left[\frac{\partial \underline{Q}}{\partial T} + L(\underline{Q})\right] \Phi^i \, dV = 0,$$
$$R^i := \int_V \left[\frac{\partial \underline{Q}}{\partial T} + \frac{1}{2}\underline{L}(\underline{Q}^{n+1}) + \frac{1}{2}\underline{L}(\underline{Q}^n)\right] \Phi^i \, dV = \underline{0}. \tag{6.34}$$

Here, the time derivatives of unknown variables are discretised using the backward difference with a special attention to the vertically moving grid, as follows:

$$\frac{\partial U}{\partial T} = \frac{U^{n+1} - U^n}{\Delta T} - \frac{Y^{n+1} - Y^n}{\Delta T}\left(\frac{\partial U}{\partial Y}\right)^n,$$
$$\frac{\partial V}{\partial T} = \frac{V^{n+1} - V^n}{\Delta T} - \frac{Y^{n+1} - Y^n}{\Delta T}\left(\frac{\partial V}{\partial Y}\right)^n,$$
$$\frac{\partial H}{\partial T} = \frac{H^{n+1} - H^n}{\Delta T},$$

where the flow field variables at the $(n+1)^{th}$ time step is unknown and to be solved based on the known ones at the previous n^{th} time step. The system of the algebraic equations obtained are solved for the unknown variables vector $\underline{Q}$ using the Newton-

Institutional Repository - Library & Information Centre - University of Thessaly
09/06/2024 06:51:43 EEST - 18.219.33.223

Raphson method,

$$Q^{n+1} = Q^n - \underline{\underline{J}}^{-1}\underline{R}(\underline{Q}^n),$$

where $\underline{\underline{J}}$ is the Jacobian of the vector of residuals, $\underline{R}$, with respect to the vector of unknown variables, $\underline{Q}$.

6.3 Computational Method for the Linearised Governing Equations

6.3.1 Linearising the Unknown Variables

In order to investigate the linear stability of the flow, the perturbation to the known base flow is assumed to be infinitesimal. Hence all nonlinear (high order) terms of perturbation are neglected in comparison to the first order terms. This results in a linearised form of the governing equations for the time evolution of the unknown perturbation. Denoting the overhead bar for the steady value of the base flow and the tilde for the perturbed value, the linearisation of the nodal coordinates and free surface height are expressed as follows,

$$X = \bar{X}, \text{ (grid node is not perturbed in the streamwise direction)} \tag{6.35}$$

$$Y = \bar{Y} + \tilde{Y}, \tag{6.36}$$

$$H = \bar{H} + \tilde{H}. \tag{6.37}$$

Any other unknown variable of the flow field is necessarily linearized as a sum of the known steady value and an unknown perturbed value. If considered in the physical domain, the perturbed term should include both local perturbation $\tilde{U})|_{Y=\bar{Y}}$ and the one due to perturbed grid $U_Y|_{Y=\bar{Y}}\,\tilde{Y}$, and results in complication with higher-order Y derivative. In order to avoid this Y-derivative, it is practical to determine the linearization of the flow unknown variables at frozen coordinates (ξ, η) of the

Institutional Repository - Library & Information Centre - University of Thessaly
09/06/2024 06:51:43 EEST - 18.219.33.223

computational domain, as follows,

$$U = \bar{U} + \tilde{U}, \tag{6.38}$$

$$V = \bar{V} + \tilde{V}, \tag{6.39}$$

$$P = \bar{P} + \tilde{P}. \tag{6.40}$$

The pressure jump, which is set at a fixed node, is linearised as $\nabla P = \nabla\bar{P} + \nabla\tilde{P}$. The unit tangential vector, $\underline{t} = \dfrac{(X_\xi, Y_\xi)^*}{\sqrt{X_\xi^2 + Y_\xi^2}} = (t_1, t_2)^*$ of the free surface is linearised by first considering the denominator,

$$\begin{aligned}(X_\xi^2 + Y_\xi^2)^{-1/2} =& \left(\bar{X}_\xi^2 + (\bar{Y}_\xi + \tilde{Y}_\xi)^2\right)^{-1/2} \\ =&(\bar{X}_\xi^2 + \bar{Y}_\xi^2 + 2\bar{Y}_\xi\tilde{Y}_\xi + \mathcal{O}(\tilde{Y}_\xi^2))^{-1/2} \\ =&(\bar{X}_\xi^2 + \bar{Y}_\xi^2)^{-1/2} + (-1/2)(\bar{X}_\xi^2 + \bar{Y}_\xi^2)^{-3/2}\, 2\,\bar{Y}_\xi\,\tilde{Y}_\xi.\end{aligned}$$

Plugging it back into the two components of the tangential vector, it yields,

$$\begin{aligned}t_1 =&\frac{X_\xi}{\sqrt{X_\xi^2 + Y_\xi^2}} = \frac{\bar{X}_\xi}{\left(\bar{X}_\xi^2 + (\bar{Y}_\xi + \tilde{Y}_\xi)^2\right)^{1/2}} \\ =&\bar{X}_\xi\left[(\bar{X}_\xi^2 + \bar{Y}_\xi^2)^{-1/2} - (\bar{X}_\xi^2 + \bar{Y}_\xi^2)^{-3/2}\bar{Y}_\xi\tilde{Y}_\xi\right] \\ =&\bar{t}_1 - \frac{\bar{X}_\xi\bar{Y}_\xi}{(\bar{X}_\xi^2 + \bar{Y}_\xi^2)^{3/2}}\tilde{Y}_\xi,\end{aligned} \tag{6.41}$$

$$\begin{aligned}t_2 =&\frac{Y_\xi}{\sqrt{X_\xi^2 + Y_\xi^2}} = \frac{\bar{Y}_\xi + \tilde{Y}_\xi}{\left(\bar{X}_\xi^2 + (\bar{Y}_\xi + \tilde{Y}_\xi)^2\right)^{1/2}} \\ =&(\bar{Y}_\xi + \tilde{Y}_\xi)\left[(\bar{X}_\xi^2 + \bar{Y}_\xi^2)^{-1/2} - (\bar{X}_\xi^2 + \bar{Y}_\xi^2)^{-3/2}\bar{Y}_\xi\tilde{Y}_\xi\right] \\ =&\bar{Y}_\xi(\bar{X}_\xi^2 + \bar{Y}_\xi^2)^{-1/2} + \left[(\bar{X}_\xi^2 + \bar{Y}_\xi^2)^{-1/2} - (\bar{X}_\xi^2 + \bar{Y}_\xi^2)^{-3/2}\bar{Y}_\xi^2\right]\tilde{Y}_\xi \\ =&\bar{t}_2 + \frac{\bar{X}_\xi^2}{(\bar{X}_\xi^2 + \bar{(Y)}_\xi^2)^{3/2}}\tilde{Y}_\xi.\end{aligned} \tag{6.42}$$

For the linear stability analysis, the unknown variables are the perturbed ones to be computed from the given base flow. A computational approach is going to be developed in the following to solve the linearised governing equations for these unknown variables. The linearised governing equations are obtained by replacing all the lin-

Institutional Repository - Library & Information Centre - University of Thessaly
09/06/2024 06:51:43 EEST - 18.219.33.223

earised variables to the governing equations and their residuals and by eliminating the nonlinear terms of the perturbation in these formulations.

Computationally, the linearised governing equations are then solved for the unknown perturbation in a straightforward way by the same technique as for the nonlinear problem. By the Galerkin Finite Element Method, the weak formulation of the governing equations is established by integrating the weighted residual of the governing equations. Therefore instead of linearising the governing equations first, then taking their integrations of weighted residuals, the formulation will be the same as the direct linearisation of the weighted residual of the governing equations.

6.3.2 Linearising the Continuity Equation

First, the continuity equation is considered for linearisation by replacing the linearised expressions of U and V from Eq. (6.38), (6.39) into the nonlinear residual of the continuity equation, Eq. (6.16),

$$R_C^i := \iint\limits_V \left(\frac{\partial U}{\partial X} + \frac{\partial V}{\partial Y} \right) \Psi^i \, dV = \int\limits_V \left[\frac{\partial}{\partial X}(\bar{U} + \tilde{U}) + \frac{\partial}{\partial Y}(\bar{V} + \tilde{V}) \right] \Psi^i \, dV. \quad (6.43)$$

By eliminating the zero-sum base flow terms, the nonlinear residual becomes the linear one in terms of perturbed unknown variables,

$$\tilde{R}_C^i := \iint\limits_V \left[\frac{\partial \tilde{U}}{\partial X} + \frac{\partial \tilde{V}}{\partial Y} \right] \Psi^i \, dV. \quad (6.44)$$

6.3.3 Linearising the Momentum Conservation Equations

Now the two X and Y components of the nonlinear momentum residuals in Eqs. (6.29) and (6.30) are going to be linearised. Replacing the linearised expressions of the variables and tangential vector in Eqs. (6.38), (6.39), (6.40), (6.41), and

Institutional Repository - Library & Information Centre - University of Thessaly
09/06/2024 06:51:43 EEST - 18.219.33.223

(6.42) into the equation (6.29) gives the nonlinear residual of the X momentum,

$$\begin{aligned} R^i_{MX} := \iint_V \Bigg[\Bigg(& \frac{\partial}{\partial T}\{\bar{U}+\tilde{U}\} + (\bar{U}+\tilde{U})\frac{\partial}{\partial X}\{\bar{U}+\tilde{U}\} \\ & +(\bar{V}+\tilde{V})\frac{\partial}{\partial Y}\{\bar{U}+\tilde{U}\} - \frac{3}{Re\sin\alpha}\sin\alpha \Bigg) \Phi^i \\ & +(-\{\bar{P}+\tilde{P}\} + \frac{2}{Re}\{\bar{U}_X+\tilde{U}_X\})\,\Phi^i_X \\ & +\frac{1}{Re}(\bar{U}_Y+\tilde{U}_Y+\bar{V}_X+\tilde{V}_X)\,\Phi^i_Y \Bigg]\, dV \\ & + \int_S (\Delta\bar{P}+\Delta\tilde{P})(\bar{Y}_\xi+\tilde{Y}_\xi)\Phi^i\, d\xi \\ & - We \int_S (\bar{t}_1 - \frac{\bar{X}_\xi\bar{Y}_\xi}{(\bar{X}^2_\xi+\bar{Y}^2_\xi)^{3/2}}\tilde{Y}_\xi)\Phi^i_\xi\, d\xi. \end{aligned} \tag{6.45}$$

By eliminating the zero-sum terms of the steady base flow and the nonlinear terms of perturbation, the nonlinear residual, R^i_{MX}, in Eq. (6.45) reduces to a linear one, $\tilde{R}^i_{MX}$, as follows,

$$\begin{aligned} \tilde{R}^i_{MX} := \iint_V \Bigg[& \left(\frac{\partial\tilde{U}}{\partial T} + \tilde{U}\bar{U}_X + \bar{U}\tilde{U}_X + \tilde{V}\bar{U}_Y + \bar{V}\tilde{U}_Y \right) \Phi^i \\ & + \left(-\tilde{P} + \frac{2}{Re}\tilde{U}_X \right) \Phi^i_X + \frac{1}{Re}\left(\tilde{U}_Y + \tilde{V}_X \right) \Phi^i_Y \Bigg]\, dV \\ & + \int_S (\Delta\tilde{P}\bar{Y}_\xi + \Delta\bar{P}\tilde{Y}_\xi)\Phi^i\, d\xi + We \int_S \frac{\bar{X}_\xi\bar{Y}_\xi}{(\bar{X}^2_\xi+\bar{Y}^2_\xi)^{3/2}}\tilde{Y}_\xi\Phi^i_\xi\, d\xi. \end{aligned} \tag{6.46}$$

Institutional Repository - Library & Information Centre - University of Thessaly
09/06/2024 06:51:43 EEST - 18.219.33.223

Similarly the nonlinear and linear Y components, R^i_{MY} and $\tilde{R}^i_{MY}$, of the momentum residual are obtained,

$$\begin{aligned} R^i_{MY} := \iint_V \Bigg[\Bigg(& \frac{\partial}{\partial T}\{\bar{V}+\tilde{V}\} + (\bar{U}+\tilde{U})\frac{\partial}{\partial X}\{\bar{V}+\tilde{V}\} \\ & + (\bar{V}+\tilde{V})\frac{\partial}{\partial Y}\{\bar{V}+\tilde{V}\} + \frac{3}{Re\sin\alpha}\cos\alpha \Bigg) \Phi^i \\ & + \frac{1}{Re}(\bar{U}_Y + \tilde{U}_Y + \bar{V}_X + \tilde{V}_X)\,\Phi^i_X \\ & + (-\{\bar{P}+\tilde{P}\} + \frac{2}{Re}\{\bar{V}_Y + \tilde{V}_Y\})\,\Phi^i_Y \Bigg]\, dV \\ & - \int_S (\Delta\bar{P} + \Delta\tilde{P})(\bar{Y}_\xi + \tilde{Y}_\xi)\Phi^i\, d\xi \\ & - We \int_S (\bar{t_2} + \frac{\bar{X}^2_\xi}{(\bar{X}^2_\xi + \bar{Y}^2_\xi)^{3/2}}\tilde{Y}_\xi)\Phi^i_\xi\, d\xi. \end{aligned} \tag{6.47}$$

and

$$\begin{aligned} \tilde{R}^i_{MY} := \iint_V \Bigg[& \left(\frac{\partial\tilde{V}}{\partial T} + \bar{U}\tilde{V}_X + \tilde{U}\tilde{V}_X + \bar{V}\tilde{V}_Y + \tilde{V}\bar{V}_Y \right) \Phi^i \\ & + \frac{1}{Re}\left(\tilde{U}_Y + \tilde{V}_X\right)\,\Phi^i_X + \left(-\tilde{P} + \frac{2}{Re}\tilde{V}_Y\right)\,\Phi^i_Y \Bigg]\, dV \\ & - \int_S \Delta\tilde{P}\bar{X}_\xi\,\Phi^i\, d\xi - We \int_S \frac{\bar{X}^2_\xi}{(\bar{X}^2_\xi + \bar{Y}^2_\xi)^{3/2}}\tilde{Y}_\xi\Phi^i_\xi\, d\xi. \end{aligned} \tag{6.48}$$

6.3.4 Linearising the Kinematic Equation

Replacing the linearised expression of H, as well as U and V in Eq. (6.37), (6.38), (6.39) into the equation (6.18) gives:

$$R^i_K := \int_0^1 \left[(\bar{H}_T + \tilde{H}_T)\bar{X}_\xi + (\bar{U}+\tilde{U})(\bar{Y}_\xi + \tilde{Y}_\xi) - (\bar{V}+\tilde{V})\bar{X}_\xi \right] \Phi^i\, d\xi. \tag{6.49}$$

Institutional Repository - Library & Information Centre - University of Thessaly
09/06/2024 06:51:43 EEST - 18.219.33.223

By eliminating the terms of the steady base flow and the nonlinear terms of perturbation, the linearised residual of the kinematic equation is given as follows,

$$\tilde{R}_K^i := \int_0^1 \left[\tilde{H}_T \bar{X}_\xi + \bar{U}\tilde{Y}_\xi + \tilde{U}\bar{Y}_\xi - \tilde{V}\bar{X}_\xi \right] \Phi^i \, d\xi. \tag{6.50}$$

6.3.5 Linearising the Mass Equation

For a no-mass exchange flow, the mass conservation dictates that the mass perturbation during the flow evolution on the computational domain is equal to zero. It is described as follows,

$$M := \int_0^L (H - W) \, dX = L, \quad \text{or}$$

$$M := \int_0^L (\bar{H} + \tilde{H} - W) \, dX = L. \tag{6.51}$$

When scaling with the mean film thickness, the mass of the steady base flow equals to L

$$\bar{M} := \int_0^L (\bar{H} - W) \, dX = L. \tag{6.52}$$

Therefore, the condition of no mass perturbation is expressed as follows,

$$\tilde{M} := \int_0^L \tilde{H} \, dX = 0, \quad \text{or} \tag{6.53}$$

$$\tilde{R}_{Mass} := \int_0^L \tilde{H} \, dX = 0. \tag{6.54}$$

Given the steady base flow, the vector of unknown variables of the perturbation,

$$\underline{\tilde{Q}} = [\tilde{U}^1, \tilde{V}^1, \cdots, \tilde{U}^N, \tilde{V}^N, \tilde{P}^1, \cdots, \tilde{P}^{NP}, \tilde{H}^1, \cdots, \tilde{H}^{NH}, \Delta\tilde{P}],$$

are correspondingly solved from the vector of the perturbed residuals,

$$\underline{\tilde{R}} = [\tilde{R}^1_{MX}, \tilde{R}^1_{MY}, \cdots, \tilde{R}^N_{MX}, \tilde{R}^N_{MY}, \tilde{R}^1_C, \cdots, \tilde{R}^{NP}_C, \tilde{R}^1_K, \cdots, \tilde{R}^{NH}_K, \tilde{R}_{MASS}],$$

Institutional Repository - Library & Information Centre - University of Thessaly
09/06/2024 06:51:43 EEST - 18.219.33.223

established in the set of Eqs. (6.44), (6.46), (6.48), (6.50), and (6.54), using the the same technique as described in Sec. 6.2.3.

6.4 Numerical results and discussion

The time-dependent computational study based on the full Navier-Stokes equations present preliminary results about the evolution of perturbation on free surface. We do the numerical experiment, using a periodic sinusoidal wall with amplitude $a = 1mm$ and wavelength $\lambda = 12mm$. Computational domain is periodic and consists of eight corrugations, $k_c = 8$. The liquid used is the aqueous glycerol solution in percentage weight 68% with physical properties: kinematic viscosity $\nu = 8.4x10^{-6}m^2/s$, surface tension $\sigma = 0.068N/m$, and density $\rho = 1185.6kg/m^3$.

Noting that those dimensional parameters are given for a more realistic reference, in fact computation by the non-dimensionalized governing equations is applied for a set of dimensionless controlling parameters as follows. The Kapitsa number is $Ka = 188.85$ which only depends on the liquid properties and is for a wall inclination fixed at a mean angle $\alpha = 35°$. Other normalized lengths are the ratio of wavelength of wall over capillary length, $\lambda_c = 3.76$ (Scaled corrugation wavelength), and the ratio of amplitude over wavelength of wall, $A = 1/12$ (Corrugation steepness). We have a good reason to use the normalized λ_c in order to express physically the effect of capillary force on free surface, which is in this case in the acting range in comparison with forcing corrugation of the high steepness.

From the above information, three different critical Reynolds numbers, corresponding to disturbances of infinitely long wavelength, wavelength of eight corrugations (equal to computational domain length), and one-corrugation wavelength are respectively given by Eq. (1.17) as $Re_{crl} = 1.19$; $Re_{cr8} = 1.23$; and $Re_{cr1} = 3.52$. Based on these different theoretical values of Re_{cr}, we may want to question the flow stability under corrugation forcing. This suggests us to carry out numerical experiments by varying only flow rate for two study cases. In the first case, $Re = 3.0$, Reynolds number is larger than both Re_{crl} and Re_{cr8}, but smaller than Re_{cr1}. The second is with Reynolds number, $Re = 5.0$, higher than all three critical values.

The time-dependent problem of liquid film flow along a specified corrugation wall now are defined with six dimensionless parameters (Re, Ka, λ_c, A, α, k_c), with appropriate boundary conditions. To start the simulation, initial condition is needed to feed into the numerical code, which is in the study a relevant steady flow solution. However, in order to observe the instability of flow, the introduction of perturba-

Institutional Repository - Library & Information Centre - University of Thessaly
09/06/2024 06:51:43 EEST - 18.219.33.223

tion compounded with different wavelengths is necessary to facilitate the growth or to recognize the decay of disturbance. Therefore, we need to get first the steady solution, called the base flow. Then, it is perturbed with very small amplitude of periodic disturbance on free surface height, so the mass conservation is ensured on the domain. The time-dependent computation provides full evolution of flow field, which is subtracted from the base flow to obtain merely evolution of perturbation. The time step should be small enough to follow flow evolution, in particular it can be $\Delta T = 0.2$ in both cases. The decay or growth of perturbation in time respectively indicate the stable or unstable state of the base flow. Moreover, perturbation evolution is rigorously quantified by its kinetic energy, E, which is obtained by integrating on the whole domain the sum of two square velocity components of perturbation part of flow.

$$E = \iint_V (\tilde{U}^2 + \tilde{V}^2) dV. \tag{6.55}$$

The decrease or increase of this energy is plotted in time to provide accurate information on the nonlinear stability of flow.

First, we want to examine the flow structure of the steady solutions for two study cases, $Re = 3$, and 5, shown in Fig. 6.2. Both are in the *subcritical* regime (in the context of steady flow specifically defined in Chapter V) where both inertia and surface tension equivalently act on free surface. Higher inertia results in larger deformation of free surface. In particular, the relative amplification (Amplitude ratio of free surface deformation to corrugation, see Ref. Chapter V) of these flows are $\beta = 0.73$ for $Re = 3$, and $\beta = 0.82$ for $Re = 5$. Moreover, these flows are close to the resonance region (Ref. Chapter V) as these large deformations of free surface couple with suppression of recirculation eddy that is found at lower Re around the bottom trough.

Next moving on the instability of the first case at $Re = 3$, due to strong forcing of capillarity combined with corrugation, free surface of the base flow significantly deforms with the same corrugation wavelength. Inertia is described as an acting cause of flow instability so a flow at $Re = 3$ on planar wall is unstable to disturbance of wavelengths equal to or shorter than the domain length. However, in this capillary-inertial regime, flow rate at $Re = 3$ is not sufficiently strong to win over the combined capillarity and corrugation force for feeding momentum to long wave instability. Any travelling disturbance on free surface is readily forced to deform periodically with a similar morphology and wavelength of the free surface of base flow. Whatever

Institutional Repository - Library & Information Centre - University of Thessaly
09/06/2024 06:51:43 EEST - 18.219.33.223

wavelength of disturbance is, the combined forces of surface tension, flow inertia and wall corrugation will gradually modulate any long wavelength into the one-corrugation wavelength. The resulting one-corrugation wavelength disturbance is not unstable under this small flow rate. As a result, all disturbances with all scales of wavelengths on the computational domain, after passing through of the modulation, declines and disappears altogether, see Fig. 6.3.

Moreover, Figure 6.4 shows meaningful information on kinetic energy (E) evolution of the above flow. At the beginning, $T = 0 \rightarrow 50$, travelling waves are modulated by wall corrugation action. They can locally be unstable but globally stable as the curve trend of kinetic energy goes down. The mechanism of raising little-up and sinking much-down of E in time depicts how is long travelling wave evolved into short wave along corrugation wall. The modulation of travelling disturbances into short-wave mode of one corrugation can clearly be reflected on this staircase-down curve at early stage $T = 0 \rightarrow 100$. After that, there is no more long wavelength so we do not see any localized increase of E but only a linear decrease. It means that there is now only short waves which are gradually being stabilized with declining amplitude. The flow in this case is stable, but interestingly at a higher Reynolds number (more than 2.4 times of Re_{cr8}) in comparison to the planar wall case. So we can conclude that this particular wall corrugation imposes a stabilizing effect on flow.

On the other hand, a small perturbation consisting of different wavelengths up to the domain length can grow from a base flow at $Re = 5$, see Fig. 6.5. This Reynolds number is larger than the critical threshold corresponding to a one-corrugation wavelength disturbance on planar wall. As the evolution of perturbation can show, long travelling wave can not completely be modulated by the wall forcing to one-corrugation short wave. Analysis by Fast Fourier Transform in Figure 6.6 reveals that disturbance of larger than one-corrugation wavelength still exists and grows with increasing amplitude, see the curve $\tilde{H}$ ordered from 10 upward or from time $T = 200$ afterward. Despite of the wall forcing, flow inertia is sufficiently strong to allow disturbance stretching out wavelength larger than the corrugation to survive and grow. There are two reasons. i) The capillary and wall forcing are unable to arrest these disturbances to synchronize with the corrugation. ii) Even so, they are unable to stabilize this one-corrugation disturbance because inertia is larger than the critical threshold for that wavelength disturbance. This is indeed a result of the interplay of both supercritical inertia and wall modulation on flow perturbation. Disturbance of intrinsically defined wavelength erupts and grows from the base flow because the two stabilizing forces of surface tension and wall corrugation are no more effective to

Institutional Repository - Library & Information Centre - University of Thessaly
09/06/2024 06:51:43 EEST - 18.219.33.223

sustain the primary stability of flow.

More information can be revealed from Figure 6.7, depicting the kinetic energy evolution of unstable flow. At the beginning ($T = 0 \to 50$), it is dominated with the long-wave modulation process. Long wave components in the perturbation strongly decay and break into shorter waves, and on the other hand the growth rate of short-wave mode is still very weak. As a whole, perturbation decays when passing through this transitional process of long-to-short mode-transfer. So we can not see the perturbation growing right away, kinetic energy even declines there. After that transition, very long or very short travelling waves continue to decay. However, short wave components which can survive with wavelength in the range $\tilde{\lambda} = (1 \to 1.14)\,\lambda$, being larger than corrugation wavelength λ, become dominant in perturbation. Inertia finds its own effect on these short waves and facilitates them to grow. As a result, there is a train of travelling waves dominant with wavelength in the range $(1 \to 1.14)\,\lambda$ or $(1.07 \pm 0.07)\lambda$ along the free surface, see the curve of $\tilde{H}$ ordered from 15 upward or from time $T = 300$ afterward in Fig.6.5. Normalized with the mean film thickness, the wavelength of perturbation is calculated as follows,

$$\tilde{\Lambda} = \frac{\tilde{\lambda}}{h_N} = \frac{\tilde{\lambda}}{\lambda}\,\lambda_c\,Ka^{1/2}(3\,Re)^{-1/3}. \tag{6.56}$$

So the normalized dominant wavelength of perturbation is given by Eq. (6.56) as $\tilde{\Lambda} = 22.4 \pm 1.5$. From the enlarged inset of Fig. 6.7 which depicts around seven periodicities on a time range from $350 \to 400$, the period of the travelling perturbation is estimated about $\tilde{T} = 7.14$. These results provide an estimate of the phase speed $\tilde{C} = \tilde{\Lambda}/\tilde{T} = 3.13 \pm 0.21$. Noting that this phase speed is of a flow beyond the critical threshold. So it is predicted that the perturbation travels as fast as three times the mean velocity near the criticality, and may increase its phase speed with higher inertia. For now, we numerically observe that the primary instability occurring on corrugation wall is of short wave mode, contradicting with long-wave instability which was extensively discussed in the classical literature for planar wall, see e.g. works by *Benjamin* (1957); *Yih* (1963). As the wall corrugation does establish a short-wave mode of primary instability on film flow, it suggests a rethinking about theoretical analysis to address properly this kind of instability.

Institutional Repository - Library & Information Centre - University of Thessaly
09/06/2024 06:51:43 EEST - 18.219.33.223

6.5 Concluding Remarks and Perspective

Numerical tools have been developed in Sec. 6.2 for the full time-dependent simulation and in 6.3 for the linear stability analysis. DNS result presents a flow stabilization by wall corrugation. The evolution of the disturbance which results from the subtraction of time-dependent flow to the steady flow is focused. We observe that long wave perturbation evolves into short wave mode due to the interaction with the corrugated wall. As short wave destabilizes flow as higher Reynolds number, this satisfactorily provides the physical mechanism of stabilization by corrugation on flow. It corroborates the stabilizing effect of wall corrugation on the film flow, as documented in some experimental studies (*Vlachogiannis and Bontozoglou*, 2002; *Wierschem et al.*, 2005) as well as numeric (*Trifonov*, 2007). Moreover beyond the critical threshold, there is a transfer of perturbation energy from long-wave to short-wave mode. The short travelling perturbation is dominant, which reveals a primary short-wave instability of film flows along corrugated wall.

Institutional Repository - Library & Information Centre - University of Thessaly
09/06/2024 06:51:43 EEST - 18.219.33.223

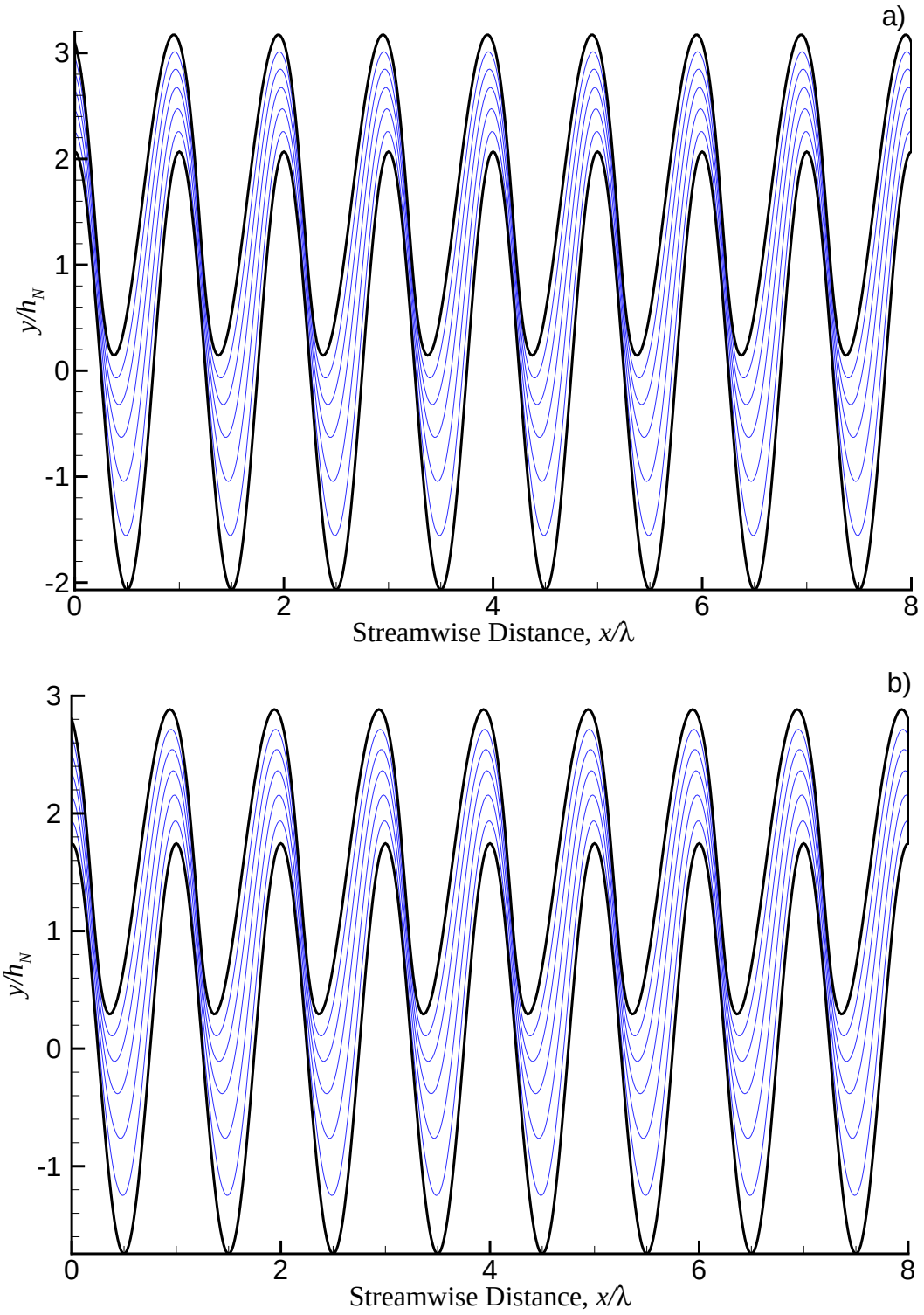

Figure 6.2: Steady solutions of a) the stable flow at $Re = 3$, and b) the unstable flow at $Re = 5$.

Institutional Repository - Library & Information Centre - University of Thessaly
09/06/2024 06:51:43 EEST - 18.219.33.223

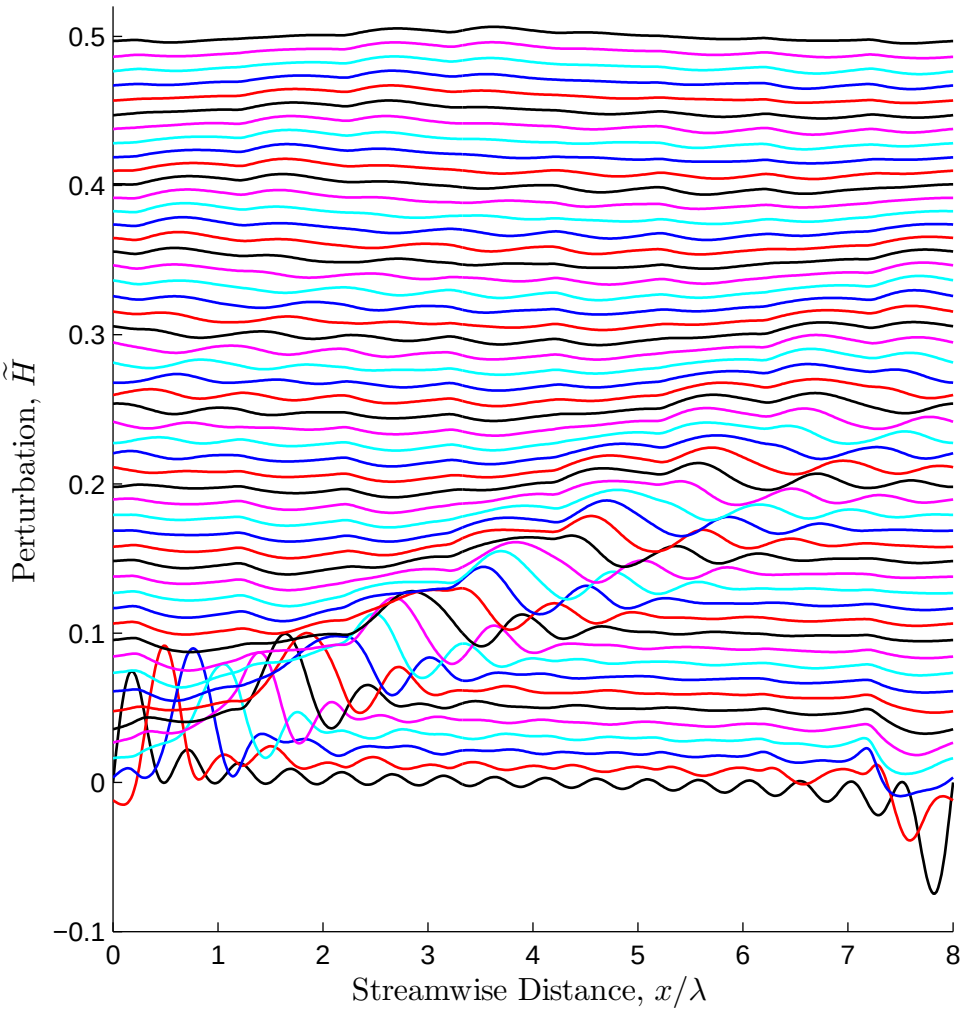

Figure 6.3: Evolution of perturbation in the stable flow at $Re = 3$. Perturbed height, $\tilde{H}$, of the free surface is depicted every time interval of 2. It is shifted upward a distance of 0.01 consecutively for the sake of clarity.

Institutional Repository - Library & Information Centre - University of Thessaly
09/06/2024 06:51:43 EEST - 18.219.33.223

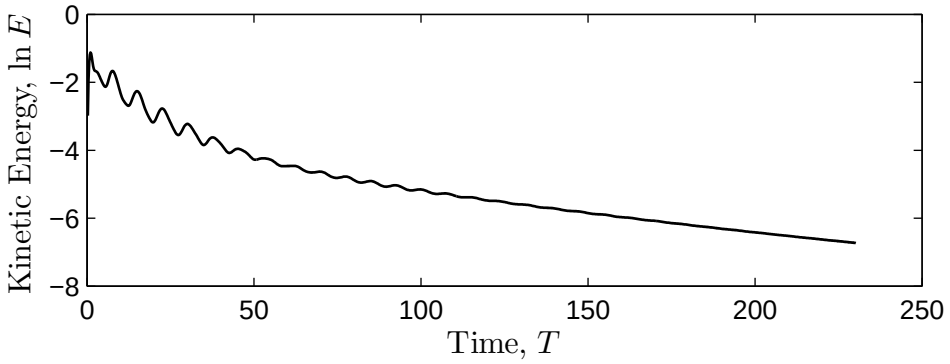

Figure 6.4: Kinetic energy of perturbation in the stable flow at $Re = 3$.

Institutional Repository - Library & Information Centre - University of Thessaly
09/06/2024 06:51:43 EEST - 18.219.33.223

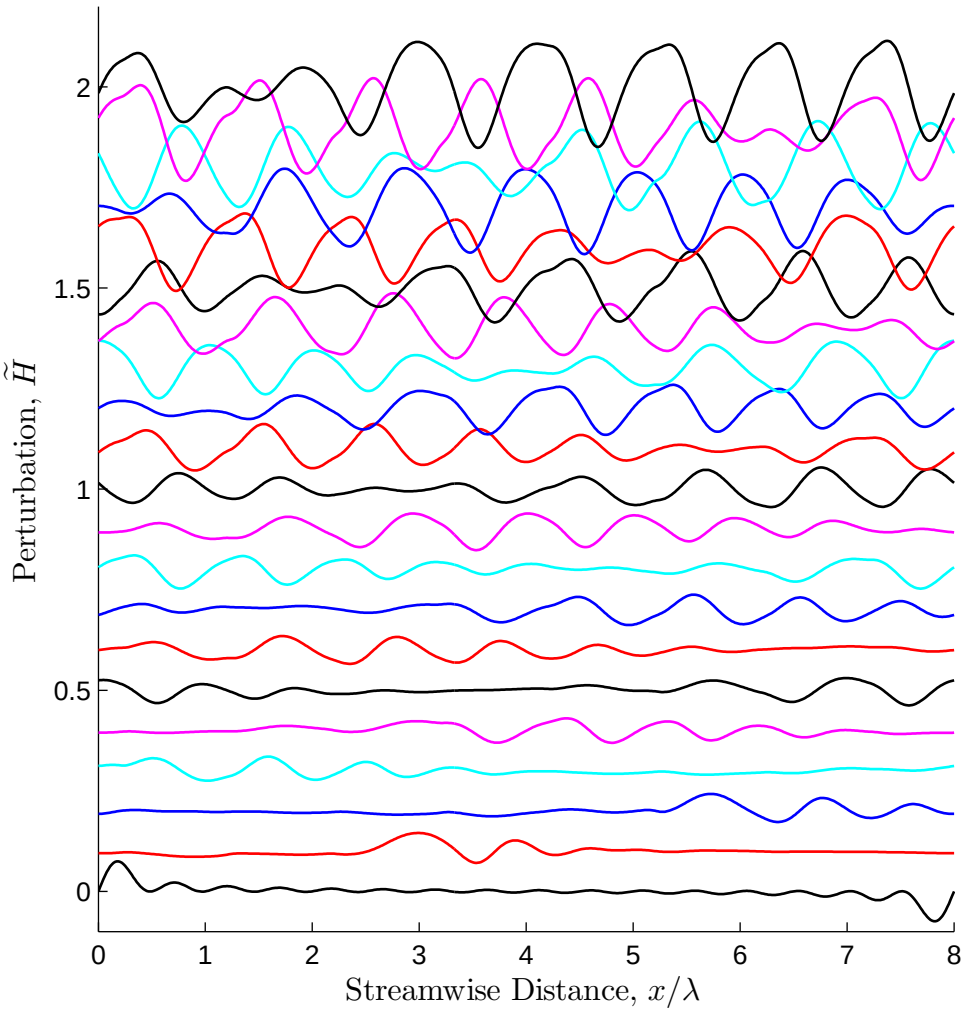

Figure 6.5: Evolution of perturbation in the unstable flow at $Re = 5$. Perturbed height, $\tilde{H}$, of the free surface is depicted every time interval of 20. It is shifted upward a distance of 0.1 consecutively for the sake of clarity.

Institutional Repository - Library & Information Centre - University of Thessaly
09/06/2024 06:51:43 EEST - 18.219.33.223

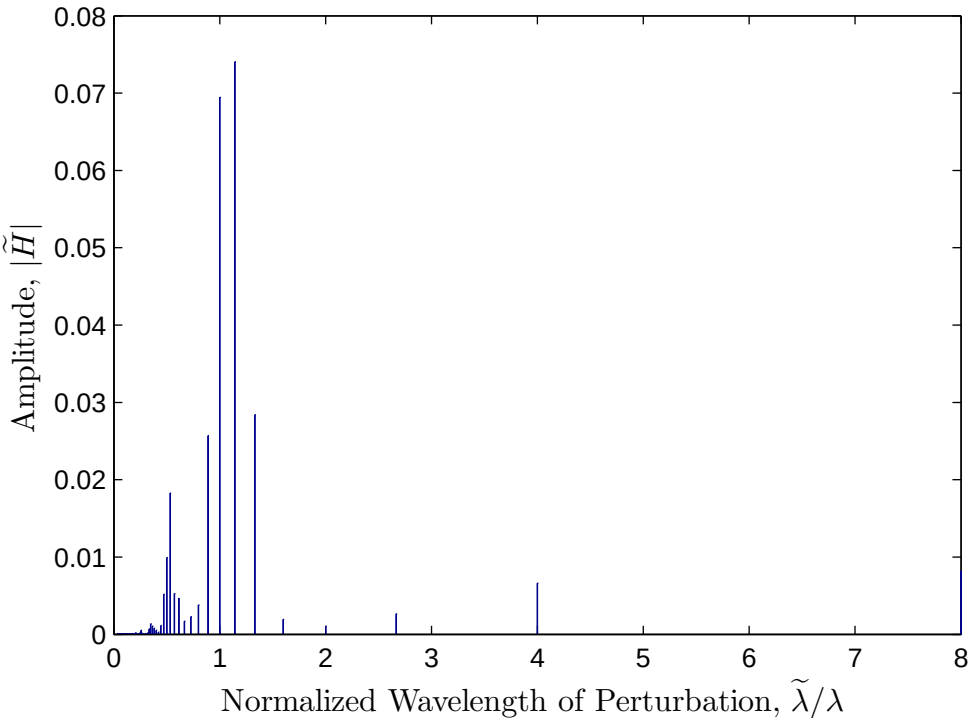

Figure 6.6: Fast Fourier Transform of perturbation profile at time $T = 400$ of the unstable flow at $Re = 5$.

Institutional Repository - Library & Information Centre - University of Thessaly
09/06/2024 06:51:43 EEST - 18.219.33.223

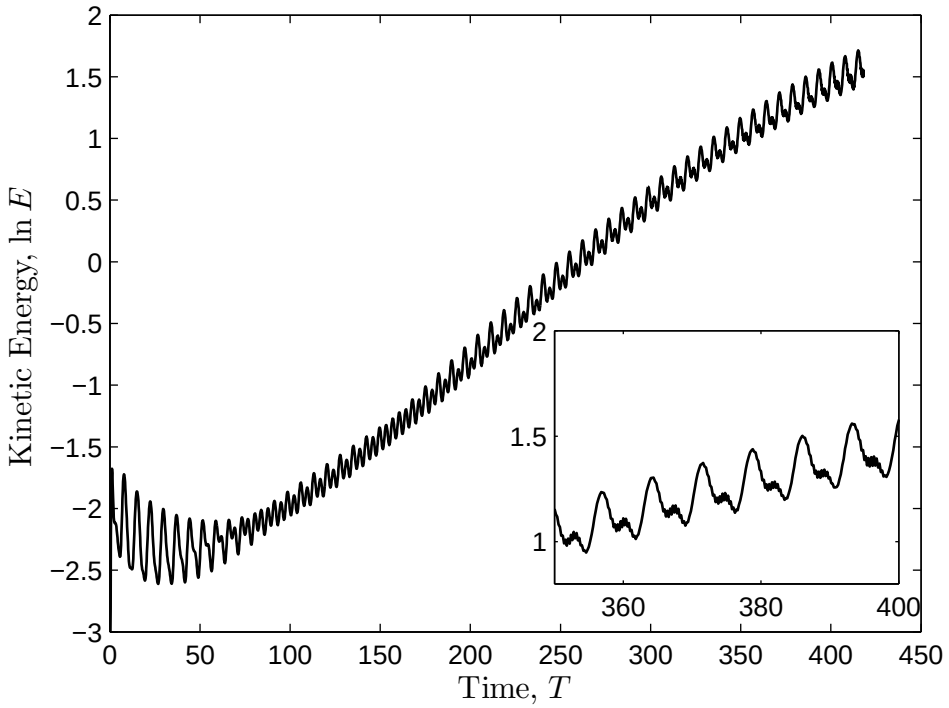

Figure 6.7: Kinetic energy of perturbation in the unstable flow at $Re = 5$.

Institutional Repository - Library & Information Centre - University of Thessaly
09/06/2024 06:51:43 EEST - 18.219.33.223

CHAPTER VII

Summary and Outlook

So far, this thesis presents the computational work to investigate the gravity-driven thin film flow along either the flat wall or periodic corrugations, using the Galerkin Finite Element Method to solve the two dimensional Navier-Stokes equations. In particular, four topical issues of the physical problem have been tackled.

For the film flow down a flat wall, the fully developed solitary waves on the free surface of film flow are characterised on a sufficiently large domain with periodic boundary condition. True solitary wave has a distinct profile consisting of main hump and capillary ripples. The wave grows monotonically exponentially at the tail of main hump and decays oscillatorily exponentially in the front of main hump, in a form of capillary ripples. Numerical prediction of the properties of the extreme solitary wave has shown their non-monotonic dependence in the transition and high inertia regime. In particular, whereas both phase speed and wave height exhibit the same behaviour for all liquids in the drag-gravity regime (low inertia), there is a fast increase of their amplitude during the transition regime and reach a maximum in the drag-inertia regime (high inertia). Computational evidence for this drastically different behaviour of regimes is marked by the gradual appearance of the reverse flow in the transition regime. Deep into the high inertia regime, the reverse flow increasingly grows and scatters in other surface dimples. After the reversal is well established, the characteristic of phase speed and heigh amplitude drops to plateau and approaching an asymptotic limit. These characteristics can only be predicted in the full second order low-dimension model of *Ruyer-Quil and Manneville* (2002). Furthermore, the viscous diffusion is found to cause opposite effects in both regimes. High viscosity liquid tends to destabilize the flow in the low inertia regime and stabilize it in higher inertia. The DNS study also confirms that below the critical threshold given by theory, there is no more wave on free surface. Parametric variation of inclination

Institutional Repository - Library & Information Centre - University of Thessaly
09/06/2024 06:51:43 EEST - 18.219.33.223

angle shows that the phase speed and wave height of extreme solitary waves increase with inclination and reach the maximum in a vertical falling film.

As it is observed that solitary waves are moving consecutively as a train of waves, the question naturally arises as to what is the interaction pattern between successive solitary waves, and in particular whether bound-states are formed. The question is first addressed for the two solitary pulse system, when it is fully developed. The computational code is successful with the novel technique of joining two individual true solitary waves to form an appropriate initial combination, rather than the naive superposition. The numerical prediction of the intrinsic separation distances, both stable and unstable, in the stationary-in-a-comoving-frame doublet has been documented and has led to the following two physical conclusions: (a) Higher inertia causes a closer increment of separation distances. (b) The separation distance is regular and in agreement with theoretical predictions (weak interaction theory) for pulses separated by intermediate to large distances, but becomes gradually irregular and deviates from theory as pulses approach each other. Moving on to the time-dependent simulation of these stationary doublets, it reveals intriguing interaction dynamics of solitary pulses. Initially large separation doublet shows a monotonic attraction or repulsion in time evolution to its stable bound-state, whereas at closest distances, the doublet system is potentially unstable and explodes, passing over several intermediate separations, to much larger separation distance. In a narrow range covering several medium separation distance, the doublet exhibits an intriguing permanent oscillation of separation distance between the two pulses, with a pronounced and non-decaying amplitude and a defined frequency. It is a kind of metastable state which indicates a narrow strange attractor of flow dynamics. Beyond this range of permanent oscillation, the separation distance in doublet evolves in a combined fashion of the behaviour. In particular, pulses will attract or repel to the nearby stable bound-state separation, not monotonically but in a form of a damping oscillation. In order to interpret the wide distribution of separation distances in a multi-pulse system *Pradas et al.* (2011a), the bound-state formation of a triplet has been studied by adding a third solitary pulse to a doublet system. If the triplet system is symmetric, the two bound-state separations are similar to the ones found in the two-pulse system. However, the separation distances significantly deviate from the doublet's one if the triplet is asymmetric, and the third pulse can affect the doublet's separation differently depending on whether it is located in front or behind. Triplet's information has given a good understanding on a statistically broad band of separations in a train of numerous solitary waves.

Institutional Repository - Library & Information Centre - University of Thessaly
09/06/2024 06:51:43 EEST - 18.219.33.223

Moving on the effect of the periodic corrugation on the free surface flow, the steady solutions of inertial film flows under gravitation has been studied. Several physical factors, such as inertia of flow, wall geometry, and liquid properties, all combine to make a complex matrix of parameters in the problem. It is observed that there is free surface resonance where the amplitude of free surface deformation attains maximum value. This physical phenomenon can be used as a demarcation to characterise uniformly the flow behaviour into subcritical or supercritical regimes. In subcritical regime, at low inertia flow or small mean film thickness, the capillary force plays the dominant role and tends to reduce the free surface deformation. This essentially creates an eddy separation in the trough of corrugation, apparently coupled with free surface deformation. Increasing inertia enhances the surface deformation up to the limit where resonance with the wall creates the largest deformation. Here, there is an interplay between inertial and capillary forces, which affect equally the flow, while the separation eddy disappears. With increasing inertia, and resembling a ballistic projection, the landing point (the lowest point on the free surface) gradually moves from upstream of the wall trough, to the bottom, and then to downstream.

In the supercritical regime, the capillary force becomes now unimportant, strong inertia helps the flow to bridge the gap between two consecutive crests and the free surface may flatten again. In this regime, the separation eddy in the trough plays as roller to support the upper-layer liquid moving faster across the corrugated substrate. It is quantitatively indicated that the flow rate on a corrugated wall with recirculation eddy is higher than the one on a flat wall. More insight can suggest, even it is another problem, that whether an object with a rather undulated surface could possibly face less resistance than with a smooth one. In the above physical studies, the flow is in the capillary-gravity regime where the ratio of the capillary length of liquid to the wavelength of corrugation wall is equally relevant to order one. Deep into the gravity regime, where the capillary length is insignificant to the wall wavelength, the flow exhibits new fascinating phenomena. The free surface can follow closely the inclined corrugated substrate, even with phase difference, to form a standing wave. However, a little higher flow rate can drastically change to form a bump or hump on the stationary free surface at its low-sloped part downstream. Finally it can evolve into a hydraulic shock where a steep and abrupt change on the free surface profile renders the computation impossible to give any more solution.

Now, several questions can be raised concerning the effect of wall corrugation on the flow instability. To this end, I wish to address this issue computationally, and to contribute some hypotheses on the prevailing physical mechanisms. Even though

Institutional Repository - Library & Information Centre - University of Thessaly
09/06/2024 06:51:43 EEST - 18.219.33.223

there have been a few theoretical and numerical results that predicted a delay of instability by the corrugation, the mechanism by which the wall corrugation imposes on the flow to modify the primary instability was not well explained and constitutes an interesting open question. My DNS results present essential information that the flow can be stable at much larger Reynolds number than in planar case. Discussion on the physical mechanism of this stabilization is sensibly addressed by focusing on the evolution of free surface disturbance obtained by subtracting full flow from the relevant steady flow. Dynamical simulation has revealed that there is a transfer of energy from long waves to short waves due to the interaction with the periodic corrugation. In order word, the additional forcing by wall corrugation modulates long waves and facilitates shorter wave formation. As shorter waves destabilize at higher Reynolds number than the long-wave threshold, this energy transfer process provides the mechanism that expands the stable regime and leads to a new, short-wave mode.

That may motivate a proper stability theory to seek for both intrinsic unstable wavelength and critical Reynolds number, in complement to the long wave one extensively established in classical literature. If intrinsic wavelength could be assumed the same as the corrugation wavelength, the critical threshold would be given by the growth rate condition, similarly to the long wave theory. However, it disregards of the corrugation amplitude whose infinitesimal limit makes the assumption inappropriate. Thus, intrinsic short wavelength is unknown a priori and must be sought together with critical Reynolds. Finally, what else will be in prospective work? i) Apart from the well-documented convective instability, there is always the possibility of a globally absolute instability at very low Reynolds number. Of particular interest is the flow over corrugations with geometric singularity such as the orthogonal wall. The latter contains multiple recirculation eddies whose instability and flexibility can modify flow, coupling with global oscillation of free surface. ii) Strongly undulated substrates can result in multiple steady flow solutions with possible bistable states and/or absolute instability. iii) The propagation of wave package on free surface flow along corrugation may deserve more investigation to understand absolute instability not in a laboratory frame but in a co-moving frame.

Institutional Repository - Library & Information Centre - University of Thessaly
09/06/2024 06:51:43 EEST - 18.219.33.223

BIBLIOGRAPHY

Institutional Repository - Library & Information Centre - University of Thessaly
09/06/2024 06:51:43 EEST - 18.219.33.223

BIBLIOGRAPHY

Alekseenko, S. V., V. Y. Nakoryakov, and B. G. Pokusaev (1985), Wave formation on a vertical falling liquid film, *AIChE J.*, *31*, 1446.

Argyriadi, K., K. Serifi, and V. Bontozoglou (2004), Nonlinear dynamics of inclined films under low-frequency forcing, *Phys. Fluids*, *16*, 2457.

Argyriadi, K., M. Vlachogiannis, and V. Bontozoglou (2006), Experimental study of inclined film flow along periodic corrugations: the effect of wall steepness, *Phys. Fluids*, *18*, 012,102.

Bach, P., and J. Villadsen (1984), Simulation of the vertical flow of a thin wavy film using a finite element method, *Int. J. Heat Mass Transf.*, *27*, 815.

Balmforth, N. J., and J. J. Liu (2004), Roll waves in mud, *J. Fluid Mech.*, *519*, 33.

Benjamin, T. B. (1957), Wave formation in laminar flow down an inclined plane, *Rev. Mod. Phys.*, *2*, 554.

Benney, D. J. (1966), Long waves on liquid films, *J. Math. Phys.*, *45*, 150.

Bontozoglou, V. (2000), Laminar film flow along a periodic wall, *Comp. Model. Eng. Sci.*, *1*, 133.

Bontozoglou, V., and G. Papapolymerou (1997), Laminar film flow down a wavy incline, *Int. J. Multiphas. Flow*, *23*, 69.

Bontozoglou, V., and K. Serifi (2008), Falling film flow along steep two-dimensional topography: The effect of inertia, *Intl. J. Multiphase Flow*, *34*, 734.

Brauner, N., and D. M. Maron (1982), Characteristics of inclined thin films, waviness and the associated mass transfer, *Int. J. Heat Mass Transf*, *25*, 99.

Bull, J. L., and J. B. Grotberg (2003), Surfactant spreading on thin viscous films: Film thickness evolution and periodic wall stretch, *Exp. Fluids*, *34*, 1.

Chang, H.-C. (1994), Wave evolution on a falling film, *Annu. Rev. Fluid Mech.*, *26*, 103.

Chang, H. C., and E. Demekhin (2002), *Complex Wave Dynamics on Thin Films*, Springer, Amsterdam.

Institutional Repository - Library & Information Centre - University of Thessaly
09/06/2024 06:51:43 EEST - 18.219.33.223

Chang, H. C., E. A. Demekhin, and D. I. Kopelevich (1993), Nonlinear evolution of waves on a falling film, *J. Fluid Mech.*, *250*, 433.

Chang, H. C., E. A. Demekhin, and E. N. Kalaidin (1995), Interaction dynamics of solitary waves on a falling film, *J. Fluid Mech.*, *294*, 123.

Chang, H. C., E. A. Demekhin, and Kalaidin (1998), Generation and suppression of radiation by solitary pulses, *SIAM (Soc. Ind. Appl. Math.) J. Appl. Math.*, *58*, 1246.

Chang, H. C., E. A. Demekhin, and S. S. Saprikin (2002), Noise-driven wave transitions on a vertically falling film, *J. Fluid Mech.*, *462*, 255.

Chen, L. H., and H. C. Chang (1986), Nonlinear waves on liquid film surfaces-ii. bifurcation analysis of the long wave equation, *Chem. Eng. Sci.*, *41*, 2477.

Craster, R. V., and O. K. Matar (2009), Dynamics and stability of thin liquid films, *Rev. Mod. Phys.*, *81*, 1131.

D'Alessio, A. J. D., J. P. Pascal, and H. A. Jasmine (2009), Instability in gravity-driven flow over uneven surfaces, *Phys. Fluids*, *21*, 062,105.

Davalos-Orozco, L. A. (2007), Nonlinear instability of a thin film flowing down a smoothly deformed surface, *Phys. Fluids*, *19*, 074,103.

Demekhin, E. A., G. Y. Tokarev, and V. Y. Shkadov (1991), Hierarchy of bifurcations of space-periodic structures in a nonlinear model of active dissipative media, *Physica D*, *52*, 338.

Demekhin, E. A., E. N. Kalaidin, S. Kalliadasis, and S. Y. Vlaskin (2007), Three-dimensional localized coherent structures of surface turbulence. i. scenarios of two-dimensional three-dimensional transition, *Phys. Fluids*, *19*, 114,103.

Demekhin, E. A., E. M. Shapar, and A. Selin (2008), Resonance effect of the bottom topography on the surface of an inclined layer of a viscous liquid, *Thermophys. Aeromech.*, *15*, 243.

deSantos, J. M., T. R. Melli, and L. E. Scriven (1991), Mechanics of gas-liquid flow in packed-bed contactors, *Ann. Rev. Fluid Mech.*, *23*, 233.

Duprat, C., F. Giorgiutti-Dauphin, D. Tseluiko, S. Saprykin, and S. Kalliadasis (2009), Liquid film coating a fiber as a model system for the formation of bound states in active dispersive dissipative nonlinear media, *Phys. Rev. Lett.*, *103*, 234,501.

Frenkel, A. L. (1992), Nonlinear theory of strongly undulating thin films flowing down vertical cylinders, *Europhys. Lett.*, *18*, 583.

Frenkel, A. L. (1993), On evolution equations for thin films flowing down solid surfaces, *Phys. Fluids A*, *5*, 2342.

Institutional Repository - Library & Information Centre - University of Thessaly
09/06/2024 06:51:43 EEST - 18.219.33.223

Gaskell, P. H., P. K. Jimack, M. Sellier, H. M. Thompson, and M. C. T. Wilson (2004), Gravity-driven flow of continuous thin liquid films on non-porous substrates with topography, *J. Fluid Mech.*, *509*, 253.

Gjevik, B. (1970), Occurance of finite-amplitude surface waves on falling liquid films, *Phys. Fluids*, *13*, 1918.

Gottlieb, O., and A. Oron (2004), Stability and bifurcations of parametrically excited thin liquid films, *Int. J. Bifurcation Chaos Appl. Sci. Eng.*, *14*, 4117.

Hacker, T., and H. Uecker (2009), An integral boundary layer equation for film flow over inclined wavy bottoms, *Phys. Fluids*, *21*, 092,105.

Heining, C., and N. Aksel (2009), Bottom reconstruction in thin-film flow over topography: Steady solution and linear stability, *Phys. Fluids*, *21*, 083,605.

Heining, C., V. Bontozoglou, N. Aksel, and A. Wierschem (2009), Nonlinear resonance in viscous films on inclined wavy planes, *Intl. J. Multiphase Flow*, *35*, 78.

Helbig, K., R. Nasarek, T. Gambaryan-Roisman, and P. Stephan (2009), Effect of longitudinal minigrooves on flow stability and wave characteristics of falling liquid films, *J. Heat Transfer*, *131*, 011,601.

Ho, L. W., and A. T. Patera (1990), A legendre spectral element method for simulation of unsteady incompressible viscous free-surface flows, *Comput. Methods Appl. Mech. Eng.*, *80*, 355.

Hoffman, K. A., and S. T. Chiang (2000), *Computational Fluid Dynamics, Volume 1, fourth edition*, Engineering Education System, Kansas.

Hood, P. (1976), Frontal solution program for unsymmetric matrices, *International Journal for Numerical Methods in Engieering*, *10*, 379–399.

Jones, L. O., and S. Whitaker (1966), An experimental study of falling liquid films, *AIChE J.*, *12*, 525.

Joo, S. W., S. H. David, and S. G. Bankoff (1991), Long-wave instabilities of heated falling films: two-dimensional theory of uniform layers, *J. Fluid Mech.*, *230*, 117.

Kalliadasis, S., and G. M. Homsy (2001), Stability of free-surface thin-film flows over topography, *J. Fluid Mech.*, *448*, 387.

Kalliadasis, S., and U. Thiele (2007), *Thin Films of Soft Matter*, Springer-Wien, New York.

Kalliadasis, S., C. Bielarz, and G. M. Homsy (2000), Steady free-surface thin film flows over topography, *Phys. Fluids*, *12*, 1889.

Kalliadasis, S., C. Ruyer-Quil, B. Scheid, and M. G. Velarde (2012), *Falling Liquid Films*, Springer Series on Applied Mathematical Sciences, Vol. 176.

Institutional Repository - Library & Information Centre - University of Thessaly
09/06/2024 06:51:43 EEST - 18.219.33.223

Kapitza, P. L., and S. P. Kapitza (1965), Wave flow of thin fluid layers of liquid, *in Collected Works of LP Kapitza*.

Kheshgi, H. S., and L. E. Scriven (1987), Disturbed film flow on a vertical plate, *Phys. Fluids*, *30*, 990.

Kliakhandler, I. L., S. H. David, and S. G. Bankoff (2001), Viscous beads on vertical fiber, *J. Fluid Mech.*, *429*, 381.

Lee, J. J., and C. C. Mei (1996), Solitary waves on an inclined sheet of viscous fluid at high reynolds and moderate weber numbers, *J. Fluid Mech.*, *307*, 191.

Leontidis, V., J. Vatteville, M. Vlachogiannis, N. Andritsos, and V. Bontozoglou (2010), Nominally two-dimensional waves in inclined film flow in channels of finite width, *Phys. Fluids*, *22*, 112,106.

Liu, J., and J. P. Gollub (1993), Onset of spatially chaotic waves on flowing films, *Phys. Rev. Lett.*, *70*, 2289.

Liu, J., and J. P. Gollub (1994), Solitary wave dynamics of film flows, *Phys. Fluids*, *6*, 1702.

Liu, J., J. D. Paul, and J. P. Gollub (1993), Measurements of the primary instabilities of film flows, *J. Fluid Mech.*, *250*, 69.

Luo, H., M. G. Blyth, and C. Pozrikidis (2008), Two-layer flow in a corrugated channel, *J. Eng. Math.*, *60*, 127.

Luo, H. X., and C. Pozrikidis (2006), Effect of inertia on film flow over oblique and three-dimensional corrugations, *Phys. Fluids*, *18*, 078,107.

Malamataris, N., M. Vlachogiannis, and V. Bontozoglou (2002a), Solitary waves on inclined films: Flow structure and binary interactions, *Phys. Fluids*, *14*, 1082.

Malamataris, N. A. (1991), *Computer added analysis of flows on moving and unbounded domains: Phase change fronts and liquid leveling*, Ph.D. thesis, University of Michigan, Ann Arbor, MI.

Malamataris, N. A., and V. Bontozoglou (1999), Computer aided analysis of viscous film flow along an inclined wavy wall, *J. Comp. Phys.*, *154*, 372.

Malamataris, N. A., and T. C. Papanastasiou (1991), Unsteady free surface flows on truncated domains, *Ind. Eng. Chem. Res.*, *30*, 2210.

Malamataris, N. A., M. Vlachogiannis, and V. Bontozoglou (2002b), Solitary waves on inclined films: Flow structure and binary interactions, *Phys. Fluids*, *14*, 1082.

Mei, C. C. (1966), Nonlinear gravity waves in a thin sheet of viscous fluid, *J. Math. Phys.*, *45*, 266.

Institutional Repository - Library & Information Centre - University of Thessaly
09/06/2024 06:51:43 EEST - 18.219.33.223

Meza, C. E., and V. Balakotaiah (2008), Modeling and experimental studies of large amplitude waves on vertically falling films, *Chem. Eng. Sci.*, *63*, 4704.

Nakaya, C. (1989), Waves on a viscous fluid film down a vertical wall, *Phys. Fluids A*, *1*, 1143.

Negny, S., M. Meyer, and M. Prevost (2001a), Study of laminar falling film flowing over a wavy column: Part I. Numerical investigation of the flow pattern and the coupled heat and mass transfer, *Int. J. Heat Mass Transf.*, *44*, 2137.

Negny, S., M. Meyer, and M. Prevost (2001b), Study of laminar falling film flowing over a wavy column: Part II. Experimental validation of hydrodynamic model, *Int. J. Heat Mass Transf.*, *44*, 2147.

Nguyen, C. C., and F. Plourde (2011), Wavy wall influence on the hydrodynamic instability of a liquid film flowing along an inclined plane, *Intl. J. Heat and Fluid Flow*, *32*, 698.

Nguyen, L. T., and V. Balakotaiah (2000), Modeling and experimental studies of wave evolution on free falling viscous films, *Phys. Fluids*, *12*, 2236.

Nguyen, P.-K., and V. Bontozoglou (2011), Steady solutions of inertial film flow along strongly undulated substrates, *Phys. Fluids*, *23*, 052,103.

Nguyen, P.-K., M. Pradas, S. Kalliadasis, and V. Bontozoglou (2012), Bound-state formation on falling liquid film, in *The 15th International Conference on Fluid Flow Technologies, Proceedings, Budapest, Hungary.*

Northey, P. J., R. C. Armstrong, and R. A. Brown (1990), Finite element calculation of time-dependent two-dimensional viscoelastic flow with explicitly elliptic momentum equation formulation, *J. Non-Newtonian Fluid Mech.*, *36*, 109.

Nosoko, T., and A. Miyara (2004), The evolution and subsequent dynamics of waves on a vertically falling liquid film, *Phys. Fluids*, *16*, 1118.

Olson, M. D. (1977), *Comparison of various finite element solution methods for Navier-Stokes equations*, Finite elements in water resources, Pentech Press London.

Oron, A., and P. Gottlieb (2002), Nonlinear dynamics of temporally excited falling liquid films, *Phys. Fluids*, *14*, 2622.

Oron, A., and C. Heining (2008), Weighted-residual integral boundary-layer model for the nonlinear dynamics of thin liquid films falling on an undulating vertical wall, *Phys. Fluids*, *20*, 082,102.

Oron, A., S. H. Davis, and S. G. Bankoff (1997), Long-scale evolution of thin liquid films, *Rev. Mod. Phys.*, *69*, 931.

Institutional Repository - Library & Information Centre - University of Thessaly
09/06/2024 06:51:43 EEST - 18.219.33.223

Pak, M., and G. Hu (2011), Numerical investigations on vortical structures of viscous film flows along periodic rectangular corrugations, *International Journal of Multiphase Flow*, *27*, 369.

Pozrikidis, C. (1988), The flow of a liquid film along a periodic wall, *J. Fluid Mech.*, *188*, 275.

Pozrikidis, C. (2003), Effect of surfactants on film flow down a periodic wall, *J. Fluid Mech.*, *496*, 105.

Pradas, M., D. Tseluiko, and S. Kalliadasis (2011a), Rigorous coherent-structure theory for falling liquid films: Viscous dispersion effects on bound-state formation and self-organization, *Phys. Fluids*, *23(1)*, 1070.

Pradas, M., D. Tseluiko, and S. Kalliadasis (2011b), Binary interactions in falling liquid films (submitted), in *Proc. IMA Conference on Nonlinearity and Coherent Structures, Reading, UK*.

Prokopiou, T., M. Cheng, and H. C. Chang (1991), Long waves on inclined films at high reynolds number, *J. Fluid Mech.*, *222*, 665.

Pumir, A., P. Manneville, and Y. Pomeau (1983), On solitary waves running down an inclined plane, *Journal of Fluid Mech*, *135*, 27.

Quere, D. (1999), Fluid coating on a fiber, *Annu. Rev. Fluid Mech.*, *31*, 347.

Ramaswamy, B., S. Chippada, and S. W. Joo (1996), A full-scale numerical study of interfacial instabilities in thin-film flows, *J. Fluid Mech.*, *325*, 163.

Rosenau, P., A. Oron, and J. Hyman (1992), Bounded and unbounded patterns of the benney equation, *Phys. Fluids A*, *4*, 1102.

Ruyer-Quil, C., and P. Manneville (1998), Modeling film flows down inclined planes, *Eur. Phys. J. B*, *6*, 277.

Ruyer-Quil, C., and P. Manneville (2000), Improved modeling of flows down inclined planes, *Eur. Phys. J. B*, *15*, 357–359.

Ruyer-Quil, C., and P. Manneville (2002), Further accuracy and convergence results on the modelling of flows down inclined planes by weighted-residual approximations, *Phys. Fluids*, *14*, 170.

Ruyer-Quil, C., and P. Manneville (2005), On the speed of solitary waves running down a vertical wall, *J. Fluid. Mech*, *531*, 181–190.

Salamon, T. R., R. C. Armstrong, and R. A. Brown (1994), Traveling waves on inclined films: Numerical analysis by the finite-element method, *Phys. Fluids*, *6*, 2202.

Institutional Repository - Library & Information Centre - University of Thessaly
09/06/2024 06:51:43 EEST - 18.219.33.223

Sani, R., P. Gresho, and R. Lee (1980), On the spurious pressures generated by certain gfem solutions of the incompressible navier-stokes equations, in *Third Int. Conf. on Finite Elements in Flow Problems, Proceedings, Banff, Alberta, Canada*.

Scheid, B., C. Ruyer-Quil, U. Thiele, O. Kabov, J. Legros, and P. Colinet (2005), Validity domain of the benney equation including marangoni effect for closed and open flows, *Journal of Fluid Mechanics.*, *527*, 303.

Scheid, B., C. Ruyer-Quil, and P. Manneville (2006), Wave patterns in film flows: modeling and three-dimensional waves, *J. Fluid Mech.*, *562*, 183.

Scholle, M., A. Wierschem, and N. Aksel (2004), Creeping films with vortices over strongly undulated bottoms, *Acta Mech.*, *168*, 167.

Scholle, M., A. Haas, N. Aksel, M. C. T. Wilson, and P. H. Thompson, H. M. Gaskell (2008), Competing geometric and inertial effects on local flow structure in thick gravity-driven fluid films, *Phys. Fluids*, *20*, 123,101.

Shetty, L., and R. L. Cerro (1993), Flow of a thin film over a periodic surface, *Int. J. Multiphas. Flow*, *18*, 495.

Shkadov, V. Y. (1967), Wave modes in the flow of thin layer of a viscous liquid under the action of gravity, *Izv. Akad. Nauk SSSR, Mekh. Zhidk. Gaza*, *1*, 43.

Shkadov, V. Y. (1968), Theory of wave flows of a thin layer of a viscous liquid, *Izv. Akad. Nauk SSSR, Mekh Zhidk. Gaza*, *2*, 20.

Sivashinsky, G. I., and D. M. Michelson (1980), On the irregular wavy ?ow of a liquid film down a vertical plane, *Prog. Theor. Phys.*, *63*, 2112.

Strang, G., and G. Fix (1973), *An analysis of the Finite Element Method, 2nd Ed.*, Prentice Hall Inc.

Tailby, S. R., and S. Portalski (1962), The determination of the wavelength on a vertical film of liquid flowing down a hydrodynamically smooth plate, *Trans. Inst. Chem. Eng.*, *40*, 114.

Takahama, H., and S. Kato (1980), Longitudinal flow characteristics of vertically falling liquid films without concurrent gas flow, *Int. J. Multiphase Flow*, *6*, 203.

Tihon, J., K. Serifi, K. Argyriadi, and V. Bontozoglou (2006), Solitary waves on inclined films: their characteristics and the effects on wall shear stress, *Exp. Fluids*, *41*, 79.

Tougou, H. (1978), Long waves on a film flow of a viscous fluid down an inclined uneven wall, *J. Phys. Soc. Jpn.*, *44*, 1014.

Trifonov, Y. Y. (1998), Viscous liquid film flow over a vertical corrugated surface and waves formation on the film free surface, in *In Third Intl Conf. on Multiphase Flow. Lyon, France*.

Institutional Repository - Library & Information Centre - University of Thessaly
09/06/2024 06:51:43 EEST - 18.219.33.223

Trifonov, Y.-Y. (1999), Viscous liquid film flows over a periodic surface, *Intl. J. Multiphase Flow*, *24*, 1139.

Trifonov, Y.-Y. (2007), Stability of a viscous liquid film flowing down a periodic surface, *International Journal of Multiphase Flow*, *33*, 1186.

Trifonov, Y. Y., and O. Y. Tsvelodub (1991), Nonlinear waves on the surface of a falling liquid film. part 1. waves of the first family and their stability, *J. Fluid Mech.*, *229*, 531.

Tseluiko, D., M. G. Blyth, D. T. Papageorgiou, and J.-M. Vanden-Broeck (2008), Electrified viscous thin film flow over topography, *J. Fluid Mech.*, *597*, 449.

Tseluiko, D., M. G. Blyth, D. T. Papageorgiou, and J. M. Vanden-Broeck (2009), Viscous electrified film flow over step topography, *SIAM J. Appl. Math.*, *70*, 845.

Tseluiko, D., S. Saprykin, C. Duprat, F. Giorgiutti-Dauphin, and S. Kalliadasis (2010a), Pulse dynamics in low-reynolds-number interfacial hydrodynamics: Experiments and theory, *Physica D*, *239*, 2000.

Tseluiko, D., S. Saprykin, and S. Kalliadasis (2010b), Interaction of solitary pulses in active dispersive-dissipative media, in *Proc. Est. Acad. Sci., 59*, p. 139.

Tsvelodub, O. Y., and Y. Y. Trifonov (1989), On steady-state travelling solutions of an evolution describing the behaviour of disturbances in an active dissipative media, *Physica D*, *39*, 336.

Tsvelodub, O. Y., and Y. Y. Trifonov (1992), Nonlinear waves on the surface of a falling liquid film. part 2. bifurcations of the first-family waves and other types of nonlinear waves, *J. Fluid Mech.*, *244*, 149.

Valluri, P., O. K. Matar, G. F. Hewitt, and M. A. Mendes (2005), Thin film flow over structured packings at moderate Reynolds numbers, *Chem. Eng. Sci.*, *60*, 1965.

Veremieiev, S., H. M. Thompson, Y. C. Lee, and P. H. Gaskell (2010), Inertial thin film flow on planar surfaces featuring topography, *Comp. and Fluids*, *39*, 431.

Vlachogiannis, M., and V. Bontozoglou (2001), Observations of solitary wave dynamics of film flows, *J. Fluid Mech.*, *435*, 191.

Vlachogiannis, M., and V. Bontozoglou (2002), Experiments on laminar film flow along a periodic wall, *J. Fluid Mech.*, *457*, 133.

Vlachogiannis, M., A. Samandas, V. Leontidis, and V. Bontozoglou (2010), Effect of channel width on the primary instability of inclined film flow, *Phys. Fluids*, *22*, 12,106.

Wang, C. Y. (1981), Liquid film flowing slowly down a wavy incline, *AIChE J.*, *27*, 207.

Institutional Repository - Library & Information Centre - University of Thessaly
09/06/2024 06:51:43 EEST - 18.219.33.223

Webb, R. L. (1994), *Principles of Enhanced Heat Transfer*, Wiley, New York.

Weinstein, S. J., and K. J. Ruschak (2004), Coating flows, *Annu. Rev. Fluid Mech.*, *36*, 29.

Wierschem, A., and N. Aksel (2003), Instability of a liquid film flowing down an inclined wavy plane, *Physica D*, *186*, 221.

Wierschem, A., and N. Aksel (2004a), Hydraulic jumps and standing waves in gravity-driven flows of viscous liquids in wavy open channels, *Phys. Fluids*, *16*, 3868.

Wierschem, A., and N. Aksel (2004b), Influence of inertia on vortices created in films creeping over strongly undulated substrates, *Phys. Fluids*, *16*, 4566.

Wierschem, A., M. Scholle, and N. Aksel (2003), Vortices in film flow over strongly undulated bottom profiles at low Reynolds numbers, *Phys. Fluids*, *15*, 426.

Wierschem, A., C. Lepski, and N. Aksel (2005), Effect of long undulated bottoms on thin gravity-driven films, *Acta Mech.*, *179*, 41.

Wierschem, A., V. Bontozoglou, C. Heining, H. Uecker, and N. Aksel (2008), Linear resonance in viscous films on inclined wavy planes, *Intl. J. Multiphase Flow*, *34*, 580.

Wierschem, A., T. Pollak, C. Heining, and N. Aksel (2010), Suppression of eddies in films over topography, *Phys. Fluids*, *22*, 113,603.

Yih, C. S. (1963), Stability of liquid flow down an inclined plane, *Phys. Fluids*, *6*, 321–33.

Yu, L. Q., F. K. Wasden, A. E. Dukler, and V. Balakotaiah (1991), Nonlinear waves on the surface of a falling liquid film. part 1. waves of the first family and their stability, *J. Fluid Mech.*, *229*, 531.

Zhao, L., and R. L. Cerro (1992), Experimental characterization of viscous film flows over complex surfaces, *Intl. J. Multiphase Flow*, *18*, 495.

Institutional Repository - Library & Information Centre - University of Thessaly
09/06/2024 06:51:43 EEST - 18.219.33.223